Electronic Transport in Interacting Nanostructures:

Time-dependent Density-Matrix-Renormalisation-Group Approach

Zur Erlangung des akademischen Grades eines
DOKTORS DER NATURWISSENSCHAFTEN
von der Fakultät für Physik
des Karlsruher Instituts für Technologie

genehmigte

DISSERTATION

von

Alexander Branschädel

aus Bad Friedrichshall

Referent:	Prof. Dr. Peter Wölfle
Korreferent:	Prof. Dr. Ferdinand Evers
Tag der Prüfung:	15. April 2011

Diese Arbeit ist

meinen Eltern

gewidmet.

Contents

Contents

Chapter 1

Introduction

For sure, Joseph Nicéphore Niépce did not think about nano-scale physics when he made the first permanent photograph of nature with a camera obscura in 1826. A layer of bitumen on a metal plate was exposed to light for several hours, hardening in the illuminated regions. When the plate was washed with lavender oil, only the hardened image area remained. Nevertheless, this technique resembles – at least in its basic ideas – modern litographic methods that are very important for today's mass production of microchips. In 1971 the Intel Corporation released the first commercially available microprocessor,

Joseph N. Niépce, Point de vue du Gras (1826)

the Intel 4004, which integrates about 2300 transistors on a die with structures of a size of $\sim 10\mu$m. Forty years later, it is roughly 10^6 times more transistors, while the width of structures is reduced to ~ 40nm. The lower limit to this present evolution is on the atomic scale. Recently, in scientific setups, experiments with single molecules coupled to electrodes have been carried out where the reversible rearrangement of the molecular configuration has been demonstrated as a future possibility to store information [1–3].

Besides the commercial motivation of further miniaturisation there also exists a vital interest in the investigation of nanostructures in basic research. On the scale of only a few atoms, quantum mechanical effects strongly dominate the behaviour of a physical system. Furthermore, screening effects that allow for an effective single particle description in bulk materials are suppressed, which may lead to strong correlation effects. If the system additionally is driven out of equilibrium, as for example by adding gradients of temperature or of the electro-chemical potential, the theoretical description and the prediction of physically relevant quantities is a demanding task.

In this work we treat electronic properties of nanostructures coupled to electrodes. The list of realisations of this kind of physical system includes, for example, quantum dots in a two-dimensional electron gas [4–9], carbon nanotubes [10, 11], and the example given above, where the structure consists of a single molecule [1, 2, 12–15].

The experimentalist has access to various controllable parameters, like the electronic potential in a gate electrode [11, 16, 17] or the minimal distance in a mechanically controllable break junction [15, 18].

The quantity of central interest in the present work is the response of the system to a bias voltage which manifests in a current of charge carriers. Landauer [19, 20] and Büttiker [21] developed a formalism that allows the computation of the current through a finite region connected to reservoirs, based on transmission coefficients, as well as the distribution functions of the reservoirs. However, this approach does not include interaction which limits its applicability in the given context – in small or low-dimensional structures, screening-effects are suppressed, therefore electron-electron interactions can no longer be neglected. For strongly interacting nanostructures, several methods to calculate the linear response conductance at vanishing bias voltage have been developed recently. One class of approaches consists in extracting the conductance from an equilibrium quantity that is easier to calculate, as for example from a persistent current calculation [22–26], from phase shifts in NRG calculations [27], or from approximations based on the tunneling density of states [28]. Alternatively one can evaluate the Kubo formula within Monte-Carlo simulations [29], or from density matrix renormalisation group (DMRG) calculations [30–32]. Linear conductance has also been investigated using Functional Renormalization Group studies [33], or by diagonalizing small clusters and attaching them to leads via a Dyson equation [34].

For the computation of *finite bias* conductance, Meir and Wingreen found a formal solution using Keldysh Green's functions [35]. However, the evaluation of these formulas for interacting systems is generally based on approximations such as real time Keldysh RG [36]. Within the framework of time-dependent density functional theory (td-DFT) and Keldysh Green's functions Stefanucci and Almbladh [37, 38] discuss the extraction of conduction from real time simulations. The restriction to finite sized systems for calculating transport within td-DFT was also discussed by Di Ventra and Todorov [39]. In Ref. [40], Bushong, Sai, and Di Ventra discuss the extraction of a finite bias current in the framework of td-DFT. Weiss, Eckel, Thorwart and Egger [41] discuss an iterative method based on the summation of real-time path integrals (ISPI) in order to address quantum transport problems out of equilibrium. Han and Heary [42] discuss strongly correlated transport in the Kondo regime using imaginary time Quantum Monte Carlo techniques.

The extraction of finite bias conductance of nanostructures based on real-time simulations has also been discussed for various situations [43–60] in the framework of DMRG [61–66]. This concept provides a unified description of strong and weak interactions and works in the linear and finite bias regime, as long as finite size effects are treated properly. In this approach, the many-particle wave function is directly computed, which allows the incorporation of even exotic excitations. The method was successfully applied to obtain results for the finite bias conductance in the interacting resonant level model (IRLM), showing perfect agreement with analytical methods based on the Bethe ansatz [56]. I–V-characteristics have been obtained for the single-impurity Anderson model using the adaptive td-DMRG-method [57].

Finite size effects and especially the impact of the possible combinations of tight binding leads with an even or odd number of sites coupled to the structure have been studied in detail in [58] for a single impurity and for three quantum dots. Recently [67] we showed that finite size effects can be directly related to the distribution of the single-particle energy-levels in non-interacting systems.

The great success in obtaining finite bias conductance of interacting nanostructures that has been achieved based on time-evolution simulations gave reason to raise the bar. The study of current *fluctuations* in nanodevices is connected with important physical questions, including the nature of fundamental excitations in strongly interacting electronic systems [68–71], the possibility of fluctuation theorems out of equilibrium [72], and the time evolution of many-body entanglement [73, 74]. Experimental progress in this area has been swift – second and third cumulants have been measured in several systems [75, 76], shot noise of single hydrogen molecules has been measured [14], and even the full counting statistics has been obtained in semi-conductor quantum dots [8, 9]. On the theory side, the free case has given rise to a lot of analytical studies [73, 74, 77, 78], but progress on the most interesting situations – far from equilibrium and with strong interactions – has been difficult (see [79] for a review). Over the years, extensions of the Bethe ansatz to study transport properties have been proposed [80–83], which might open the road to important progress.

One of the major goals of this work is to investigate a numerical method to compute zero temperature noise (shot noise) of the current through a strongly interacting region. In order to obtain the time-dependent current correlations we therefore extend the time evolution scheme based on the DMRG that was successfully used to obtain the I-V-characteristics for the IRLM before [56]. The main problem turns out to be the finite size effects of the results of the non-equilibrium correlation functions for finite systems, which in part can be controlled by analytical reasoning, and in part can be removed by linear extrapolation to the thermodynamic limit [84]. We provide numerical results for the shot noise in the self-dual IRLM, where we find excellent agreement with analytical results based on the Bethe ansatz [85].

1.1 Structure of this work

This work is organized as follows: The first three chapters are intended to give an introduction to the field of research, while the main results are presented in chapters 4 and 5. Additional information, as for example analytic results provided by collaborators, is given in the appendix.

In chapter 2, the introductory part of this work is complemented quantitatively by discussing simple models that are appropriate to describe the physics of the aforementioned systems. The focus of chapter 3 is to give an overview of the numerical methods that build the foundation for the computation of the main results, where we also hint at possible applications that have not been carried out for this work.

We then investigate spectral properties of an interacting nanostructure in chapter 4 before discussing conductance and shot noise – the latter being the central result of this work – for a non-equilibrium transport setup in chapter 5. A special emphasis throughout chapters 4 and 5 is set on removing effects from the finite size of the simulated systems, yielding results for the thermodynamic limit. Please note, that the results on the spectral properties are still work in progress. The main focus here is to demonstrate an approach based on the expansion of the impurity Green's function in orthogonal polynomials.

1.2 List of publications

The content of chapter 5 has been published in

A. Branschädel, T. Ulbricht, and P. Schmitteckert, Conductance of Correlated Nanostructures, in: High Performance Computing in Science and Engineering '09, edited by W.E. Nagel, D. Kröner, and M.M. Resch, (Springer, Berlin, 2009), pp. 123-135 [53]

A. Branschädel and P. Schmitteckert, Conductance and Noise Correlations of Correlated Nanostructures, in: High Performance Computing in Science and Engineering '10, edited by W.E. Nagel, D. Kröner, and M.M. Resch, (Springer, Berlin, 2010), pp. 169-179 [54]

A. Branschädel, E. Boulat, H. Saleur, and P. Schmitteckert, Numerical evaluation of shot noise using real-time simulations, Phys. Rev. B **82**, 205414 (2010) [84]

A. Branschädel, E. Boulat, H. Saleur, and P. Schmitteckert, Shot Noise in the Self-Dual Interacting Resonant Level Model, Phys. Rev. Lett. **105**, 146805 (2010) [85]

A. Branschädel, G. Schneider, and P. Schmitteckert, Conductance of inhomogenous systems: Real-time dynamics, Ann. Phys. (Berlin) **522**, 657 (2010) [67]

There is a publication in preparation for the content of chapter 4.

Unrelated work:

A. Branschädel and T. Gasenzer, 2PI nonequilibrium versus transport equations for an ultracold Bose gas, J. Phys. B: At. Mol. Opt. Phys. **41**, 135302 (2008)

Chapter 2

Physical Models

The system we want to describe consists of a nanostructure that is attached to leads, Fig. 2.1. The leads may consist of a two-dimensional electron gas, or of metallic wires, for example. The assumption of the leads being sufficiently big allows the representation of the electrons as free particles, since the electron-electron interaction can be assumed to be screened. On the other hand, due to the small size of the nanostructure, one there can not benefit from screening effects that occur in the leads. Instead, electron-electron interaction has to be taken into account.

For the numerical treatment of the physical questions we are interested in, the huge number of degrees of freedom this composite system of structure and leads consists of enforces us to choose the model for describing the system carefully. For a sufficiently small structure only a single transport channel may couple to the leads, which renders the description effectively one-dimensional. Also, the numerical method we use for the computations, based on the density matrix renormalisation group (DMRG) as discussed in chapter 3, works best for one-dimensional models. We therefore represent the leads as 1D tight-binding chains. The main results of this work, and especially the results for the shot noise, will be derived for a very simple model, the interacting resonant level model (IRLM) as defined below. There are essentially two reasons for investigating quantum fluctuations in this model: first, for the current-voltage characteristics, there is a negative differential conductance (NDC) with a power-law decay of the current in the high-voltage limit, as soon as electron-electron interaction is taken into account. The presence of this unexpected behaviour motivates us to take a closer look at this system. Second, for the IRLM, there are exact analytical solutions to the problem, if the parameters are chosen appropriately [56,85]. This allows us to check the reliability of the numerical method we apply here.

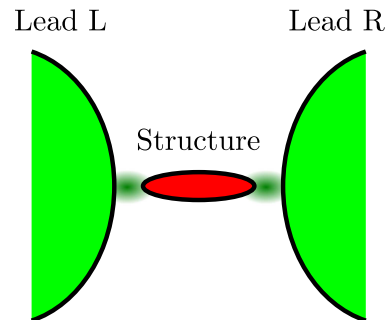Throughout the text we represent an electronic many-particle system in second quantisation language. For $\mathbf{x}$ denoting a set of degrees of freedom (as, for exam-

Figure 2.1 Sketch of the system we want to consider. An interacting nanostructure is coupled to two leads.

ple, band index, spin, momentum, etc.), we represent creation- and annihilation-operators as

$$\hat{c}_{\mathbf{x}}^{\dagger}, \quad \hat{c}_{\mathbf{x}}, \tag{2.1}$$

which obey the usual fermionic anti-commutator relations

$$\{\hat{c}_{\mathbf{x}}, \hat{c}_{\mathbf{y}}^{\dagger}\} = \delta_{\mathbf{x},\mathbf{y}}, \quad \{\hat{c}_{\mathbf{x}}, \hat{c}_{\mathbf{y}}\} = \{\hat{c}_{\mathbf{x}}^{\dagger}, \hat{c}_{\mathbf{y}}^{\dagger}\} = 0. \tag{2.2}$$

2.1 Description of the system

Interacting Nanostructure   As pointed out in the introductory chapter, a nanostructure can be many different things, as for example a single molecule of varying complexity, or an array of quantum dots, defined by gate electrodes on top of a heterostructure. The most general Hamiltonian that includes tunneling of electrons between different orbitals (labelled by ν, μ, κ and ρ), as well as electron-electron interaction, reads

$$\hat{H}_{\mathrm{S}} = \sum_{\nu\mu,\sigma} H_{\nu\mu} \hat{c}_{\nu\sigma}^{\dagger} \hat{c}_{\mu\sigma} + \sum_{\nu\mu\kappa\rho,\sigma\sigma'} V_{\nu\mu\kappa\rho} \hat{c}_{\nu\sigma}^{\dagger} \hat{c}_{\mu\sigma'}^{\dagger} \hat{c}_{\kappa\sigma'} \hat{c}_{\rho\sigma}, \tag{2.3}$$

$$H_{\nu\mu}^{*} = H_{\mu\nu}, \quad V_{\nu\mu\kappa\rho}^{*} = V_{\rho\kappa\mu\nu}. \tag{2.4}$$

For the numerical studies presented in the following chapters we make some simplifying assumptions. In fact, we aim at reducing the complexity of the model in order to make a treatment based on the available methods possible. On the other hand, we keep a certain level of complexity in order to preserve interesting effects, as for example, a negative differential conductance. The basic idea behind this approach is to find a minimalistic model that still includes the relevant physical properties, and then to treat this model rigorously.

The system we want to consider is a linear chain of single orbitals, labelled $x = 1 \ldots M_{\mathrm{S}}$, each connected to its next neighbour via a tunneling matrix element J_{S}. The energy of an electron occupying a certain orbital is given by V_{g}, which we call a local gate potential, since in the case of a quantum dot, the energy levels can be shifted by means of gate electrodes. Furthermore, we only consider local density-density interaction U_{S}, including interaction of electrons occupying neighbouring orbitals. The Hamiltonian then can be rewritten as

$$\hat{H}_{\mathrm{S}}^{\mathrm{t.b.}} = -\sum_{\sigma,x=1}^{M_{\mathrm{S}}-1} J_{\mathrm{S},x} (\hat{c}_{x,\sigma}^{\dagger} \hat{c}_{x+1,\sigma} + \hat{c}_{x+1,\sigma}^{\dagger} \hat{c}_{x,\sigma}) + \sum_{\sigma,x=1}^{M_{\mathrm{S}}} V_{\mathrm{g},x} \hat{n}_{x\sigma}$$

$$+ \sum_{x=1}^{M_{\mathrm{S}}} U_{\mathrm{S},x}^{0} \hat{n}_{x\uparrow} \hat{n}_{x\downarrow} + \sum_{\sigma\sigma',x=1}^{M_{\mathrm{S}}-1} U_{\mathrm{S},x}^{1} \hat{n}_{x,\sigma} \hat{n}_{x+1,\sigma'}. \tag{2.5}$$

This model is a tight-binding chain of finite length, with M_{S} lattice sites, where the operators

$$\hat{n}_{x\sigma} = \hat{c}_{x\sigma}^{\dagger} \hat{c}_{x\sigma} \tag{2.6}$$

count the number of electrons with spin σ occupying a lattice site x. If we consider a situation with x-independent parameters J_{S}, V_{g} and U_{S}, and additionally neglect the next-neighbour interaction $U^1 \equiv 0$, we arrive at the Hubbard model for a finite chain.

Further simplification can be achieved by assuming polarisation of the system. If we set the number of, say, spin $\downarrow$ particles to zero, we arrive at the tight binding chain of *spinless fermions*

$$\hat{H}_{\mathrm{S},\uparrow}^{\mathrm{t.b.}} = -\sum_{x=1}^{M_{\mathrm{S}}-1} J_{\mathrm{S},x}(\hat{c}_x^\dagger \hat{c}_{x+1} + \hat{c}_{x+1}^\dagger \hat{c}_x) + \sum_{x=1}^{M_{\mathrm{S}}} V_{\mathrm{g},x}\hat{n}_x + \sum_{x=1}^{M_{\mathrm{S}}-1} U_{\mathrm{S},x}\hat{n}_x\hat{n}_{x+1}. \qquad (2.7)$$

Here, the spin index σ has been omitted, together with the local interaction contribution $U_{\mathrm{S}}^0 \hat{n}_\uparrow \hat{n}_\downarrow$, while we replace $U_{\mathrm{S}}^1 \to U_{\mathrm{S}}$ for the next-neighbour interaction.

Leads   For the description of the leads we assume that the electron-electron interaction is completely screened. If the electronic dispersion relation of the bulk material is known, the Hamiltonian for the electron dynamics in an isolated lead with label α then reads

$$\hat{H}_\alpha = \sum_{n\mathbf{k},\sigma} \varepsilon_{\alpha n\mathbf{k}} \hat{c}_{\alpha n\mathbf{k}\sigma}^\dagger \hat{c}_{\alpha n\mathbf{k}\sigma}. \qquad (2.8)$$

Here, the band index is labelled n and the electron spin is labelled $\sigma \equiv \uparrow, \downarrow$. Since for transport calculations at low temperature only the partially filled bands contribute to the electron current, we omit the band index based on the assumption that there is only a single band with partial filling,

$$\hat{H}_\alpha = \sum_{\mathbf{k},\sigma} \varepsilon_{\alpha\mathbf{k}} \hat{c}_{\alpha\mathbf{k}\sigma}^\dagger \hat{c}_{\alpha\mathbf{k}\sigma}. \qquad (2.9)$$

Coupling of nanostructure to leads   The setup we consider here involves a structure which is connected to two leads, labelled $\alpha = \mathrm{L}, \mathrm{R}$, for the "left" and the "right" lead. This structure–lead coupling is assumed to be local in space, which renders the availability of a real-space representation of the lead Hamiltonian desirable. A very simple model of a lead is a one-dimensional semi-infinite tight-binding chain, defined by the Hamiltonian

$$\hat{H}_\alpha^{\mathrm{t.b.}} = -J \sum_{\sigma,x=1}^{\infty} (\hat{c}_{x,\alpha\sigma}^\dagger \hat{c}_{x+1,\alpha\sigma} + \hat{c}_{x+1,\alpha\sigma}^\dagger \hat{c}_{x,\alpha\sigma}). \qquad (2.10)$$

If we bring this Hamiltonian to diagonal form (2.9), we obtain a cosine dispersion relation

$$\varepsilon_k = -2J\cos k, \qquad (2.11)$$

with the band width $4J$. Assuming that the 1D nanostructure, modeled by a Hamiltonian of the form (2.5), is coupled to the *end* of the semi-infinite chains L and R,
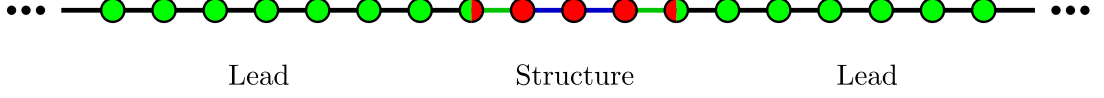
Figure 2.2 Interacting nanostructure ● coupled to two non-interacting semi-infinite leads ● (finite interaction U_C with the first lead site ◑ allowed). The system is represented as a linear tight-binding chain.

we introduce a coupling Hamiltonian

$$\hat{H}_{C,L} = - J_{C,L} \sum_\sigma (\hat{c}^\dagger_{1,\sigma} \hat{c}_{1,L\sigma} + \hat{c}^\dagger_{1,L\sigma} \hat{c}_{1,\sigma}) + \sum_{\sigma\sigma'} U_{C,L} \hat{n}_{1,\sigma} \hat{n}_{1,L\sigma'}, \qquad (2.12)$$

$$\hat{H}_{C,R} = - J_{C,R} \sum_\sigma (\hat{c}^\dagger_{M_S,\sigma} \hat{c}_{1,R\sigma} + \hat{c}^\dagger_{1,R\sigma} \hat{c}_{M_S,\sigma}) + \sum_{\sigma\sigma'} U_{C,R} \hat{n}_{M_S,\sigma} \hat{n}_{1,R\sigma'}, \qquad (2.13)$$

including an electron-electron interaction of the electrons on the "tip" of the leads and on the "tip" of the structure. Together with Eqns. (2.5,2.10), the overall setup now can be described by the Hamiltonian

$$\hat{H}^{t.b.} = \hat{H}^{t.b.}_L + \hat{H}_{C,L} + \hat{H}^{t.b.}_S + \hat{H}_{C,R} + \hat{H}^{t.b.}_R, \qquad (2.14)$$

sketched in Fig. 2.2.

2.2 Interacting Resonant Level Model

A very minimalistic transport setup with a nanostructure coupled to two leads is a structure which can be modelled by only one orbital (the *dot*). We arrive there by assuming $M_S = 1$ in Eq. (2.5). Neglecting the interaction on the contact link $U_C = 0$ results in a tight-binding version of the single impurity Anderson model [86].

An even more innocent looking model can be obtained by again assuming the strong polarisation limit where only one spin orientation persists. The local electron-electron interaction on the dot then is suppressed, the only remaining interaction effect is the interation on the contact link U_C. The result is called the *interacting resonant level model* (IRLM). The term *resonant* refers to the fact that for a very specific energy range, electrons tunnel through the dot from one lead to the other with probability 1 (*resonant tunneling*), even for very weak coupling of the dot to the leads, $J_C/J \ll 1$. Since in this work we concentrate on the investigation of the

properties of the IRLM, we once more write down the Hamiltonian for this system

$$\hat{H}_{\mathrm{IRLM}} = -J\sum_{x=1}^{\infty}(\hat{c}_x^\dagger\hat{c}_{x+1} + \hat{c}_{x+1}^\dagger\hat{c}_x + \hat{c}_{-x}^\dagger\hat{c}_{-x-1} + \hat{c}_{-x-1}^\dagger\hat{c}_{-x}) + V_{\mathrm{g}}\hat{n}_0$$

$$- J_{\mathrm{C}}(\hat{c}_0^\dagger\hat{c}_1 + \hat{c}_1^\dagger\hat{c}_0 + \hat{c}_0^\dagger\hat{c}_{-1} + \hat{c}_{-1}^\dagger\hat{c}_0) + U_{\mathrm{C}}\left[(\hat{n}_{-1} - \frac{1}{2})(\hat{n}_0 - \frac{1}{2}) + (\hat{n}_0 - \frac{1}{2})(\hat{n}_1 - \frac{1}{2})\right].$$

$$(2.15)$$

Note, that we slightly change the notation in order to simplify the expression; the *dot* level is now labelled 0, while we refer to the left (right) lead using negative (positive) indices. Furthermore, for the considerations in the following chapters, we choose the dot–lead coupling as well as the dot–lead interaction symmetric. Shifting the density operator in the interaction contribution by $-1/2$ corresponds to adding a local potential $-U_{\mathrm{C}}(\hat{n}_{-1} + \hat{n}_0 + \hat{n}_1)/2$. In doing so we guarantee, that for vanishing gate voltage $V_{\mathrm{g}} \equiv 0$, the probability for an incoming particle from one lead (L), to get scattered at the dot to the other lead (R), is maximal, if the energy of the particle is equivalent to the center of the cosine band. If we assume a "metallic" situation with a half filled band, this corresponds to resonant tunneling at the Fermi level.

2.3 Representation on a computer

In the next chapter we will discuss methods to numerically compute various properties of the models introduced above, including the impurity Green's function for the ground state of the system, and the time evolution of a non-equilibrium initial state. The methods in question altogether rely on the representation of the system's Hamiltonian on a *finite computer*, posing a very strong limitation on the models that can be considered: the Hamiltonian of the system needs to be *finite*. This means in practice that the real-space representation of the semi-infinite leads as described by Eq. (2.10) has to be cut to finite length, resulting in finite leads with M_α lattice sites. The most obvious effect of the finite size of the system is the discretisation of the energy spectrum, limiting the energy resolution of the numerical computations (cf. also Fig. A.1 in the appendix). Furthermore, the time evolution of a non-equilibrium state shows effects from reflections at the boundaries. An excitation that travels along the leads starting from the nanostructure will finally be reflected at its boundaries, which will eventually disturb the simulation of the quantities of interest, such as for example, the current through the structure.

The discussion of finite size effects and their impact on numerical results will be deferred to chapters 4 and 5 where we also present our main results. The purpose of the present section is to rewrite the infinite-lattice models, truncating the leads to finite length M_{L} and M_{R}, thus providing a unified representation for the discussion of the numerical results.

According to the sketch in Fig. 2.3 we change the labelling of the individual lattice

sites again. Rewriting the Hamiltonian (2.5,2.10,2.12-2.14) then leads to

$$\hat{H}_{\mathrm{S}}^{\mathrm{finite}} = -\sum_{\sigma, x=M_{\mathrm{L}}}^{M_{\mathrm{L}}+M_{\mathrm{S}}-2} J_{\mathrm{S},x}(\hat{c}_{x,\sigma}^{\dagger}\hat{c}_{x+1,\sigma} + \hat{c}_{x+1,\sigma}^{\dagger}\hat{c}_{x,\sigma}) + \sum_{\sigma, x=M_{\mathrm{L}}}^{M_{\mathrm{L}}+M_{\mathrm{S}}-1} V_{\mathrm{g},x}\hat{n}_{x\sigma}$$

$$+ \sum_{x=M_{\mathrm{L}}}^{M_{\mathrm{L}}+M_{\mathrm{S}}-1} U_{\mathrm{S},x}^{0}\hat{n}_{x\uparrow}\hat{n}_{x\downarrow} + \sum_{\sigma\sigma', x=M_{\mathrm{L}}}^{M_{\mathrm{L}}+M_{\mathrm{S}}-2} U_{\mathrm{S},x}^{1}\hat{n}_{x,\sigma}\hat{n}_{x+1,\sigma'}, \qquad (2.16)$$

$$\hat{H}_{\mathrm{C,L}}^{\mathrm{finite}} = -J_{\mathrm{C,L}}\sum_{\sigma}(\hat{c}_{\sigma,M_{\mathrm{L}}-1}^{\dagger}\hat{c}_{\sigma,M_{\mathrm{L}}} + \hat{c}_{\sigma,M_{\mathrm{L}}}^{\dagger}\hat{c}_{\sigma,M_{\mathrm{L}}-1}) + \sum_{\sigma\sigma'}U_{\mathrm{C,L}}\hat{n}_{\sigma,M_{\mathrm{L}}-1}\hat{n}_{\sigma',M_{\mathrm{L}}}, \qquad (2.17)$$

$$\hat{H}_{\mathrm{C,R}}^{\mathrm{finite}} = -J_{\mathrm{C,R}}\sum_{\sigma}(\hat{c}_{\sigma,M_{\mathrm{L}}+M_{\mathrm{S}}-1}^{\dagger}\hat{c}_{\sigma,M_{\mathrm{L}}+M_{\mathrm{S}}} + \mathrm{H.c.}) + \sum_{\sigma\sigma'}U_{\mathrm{C,R}}\hat{n}_{\sigma,M_{\mathrm{L}}+M_{\mathrm{S}}-1}\hat{n}_{\sigma',M_{\mathrm{L}}+M_{\mathrm{S}}},$$

$$(2.18)$$

$$\hat{H}_{\mathrm{L}}^{\mathrm{finite}} = -J\sum_{\sigma, x=0}^{M_{\mathrm{L}}-2}(\hat{c}_{\sigma x}^{\dagger}\hat{c}_{\sigma x+1} + \hat{c}_{\sigma x+1}^{\dagger}\hat{c}_{\sigma x}), \quad \hat{H}_{\mathrm{R}}^{\mathrm{finite}} = -J\sum_{\substack{x=M_{\mathrm{L}}+M_{\mathrm{S}} \\ \sigma}}^{M-2}(\hat{c}_{\sigma x}^{\dagger}\hat{c}_{\sigma x+1} + \hat{c}_{\sigma x+1}^{\dagger}\hat{c}_{\sigma x}),$$

$$(2.19)$$

$$\hat{H}^{\mathrm{finite}} = \hat{H}_{\mathrm{L}}^{\mathrm{finite}} + \hat{H}_{\mathrm{C,L}}^{\mathrm{finite}} + \hat{H}_{\mathrm{S}}^{\mathrm{finite}} + \hat{H}_{\mathrm{C,R}}^{\mathrm{finite}} + \hat{H}_{\mathrm{R}}^{\mathrm{finite}}, \qquad (2.20)$$

with M_{L} (M_{R}) lattice sites on the left (right) lead and M_{S} lattice sites on the structure. The system then consists of $M = M_{\mathrm{L}} + M_{\mathrm{S}} + M_{\mathrm{R}}$ lattice sites in total. For the IRLM, the Hamiltonian (2.15) can be correspondingly rewritten as

$$\hat{H}_{\mathrm{IRLM}}^{\mathrm{finite}} = -J\sum_{x=0}^{M_{\mathrm{L}}-2}(\hat{c}_{x}^{\dagger}\hat{c}_{x+1} + \hat{c}_{x+1}^{\dagger}\hat{c}_{x}) - J\sum_{x=M_{\mathrm{L}}+1}^{M-2}(\hat{c}_{x}^{\dagger}\hat{c}_{x+1} + \hat{c}_{x+1}^{\dagger}\hat{c}_{x}) + V_{\mathrm{g}}\hat{n}_{M_{\mathrm{L}}}$$

$$- J_{\mathrm{C}}(\hat{c}_{M_{\mathrm{L}}-1}^{\dagger}\hat{c}_{M_{\mathrm{L}}} + \hat{c}_{M_{\mathrm{L}}}^{\dagger}\hat{c}_{M_{\mathrm{L}}-1} + \hat{c}_{M_{\mathrm{L}}}^{\dagger}\hat{c}_{M_{\mathrm{L}}+1} + \hat{c}_{M_{\mathrm{L}}+1}^{\dagger}\hat{c}_{M_{\mathrm{L}}})$$

$$+ U_{\mathrm{C}}\left[(\hat{n}_{M_{\mathrm{L}}-1} - \frac{1}{2})(\hat{n}_{M_{\mathrm{L}}} - \frac{1}{2}) + (\hat{n}_{M_{\mathrm{L}}} - \frac{1}{2})(\hat{n}_{M_{\mathrm{L}}+1} - \frac{1}{2})\right]. \quad (2.21)$$

"Improved" boundary conditions   The problems due to the finite size of the system can be tackled in part by adopting an adjusted discretisation scheme for the energy levels in the leads. For example, for the computation of the response of the system to a small bias voltage, it is necessary to obtain a high energy resolution at the Fermi level. The setup we will consider later on involves a system described by one of the finite Hamiltonians introduced in this section with M lattice sites in total, and a finite and constant number N of electrons in this system. Since we want to consider metallic leads, we will adjust N to arrive at (close to) half filling[1] of the

---

[1] There are situations where the condition of half filling can not be met strictly. For example, for a system of spinless electrons with an *odd* number M of lattice sites, $N = M/2$ is not an integer number of electrons. For a discussion in more details see chapter 5.
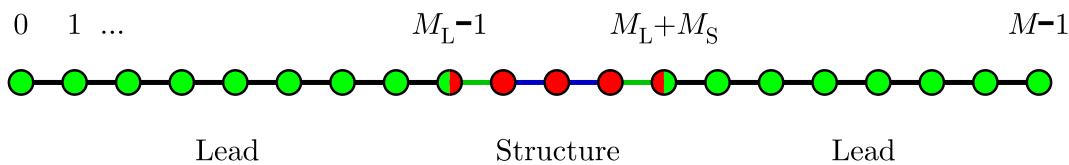
Figure 2.3 Interacting nanostructure coupled to two non-interacting *finite* leads. The system is represented as a linear tight-binding chain with an overall number of $M = M_{\mathrm{L}} + M_{\mathrm{S}} + M_{\mathrm{R}}$ lattice sites, with M_{L} (M_{R}) lattice sites in the left (right) lead and M_{S} lattice sites on the structure.

leads for the system in its ground state. This means that the Fermi level is at the center of the cosine band (2.11),

$$\varepsilon_{\mathrm{F}} = 0, \tag{2.22}$$

but unfortunately, this is exactly where the energy resolution is *lowest*. The level spacing for the single-particle energy levels of a finite, isolated tight binding lead with M_{α} lattice sites, as defined in Eq. (2.19), can be deduced from the dispersion relation (2.11) and approaches its maximum value $\Delta\varepsilon \sim 2\pi J/(M_{\alpha}+1)$ at the middle of the cosine band, cf. appendix A.

For an overview of the different methods that have been applied to adjust the level discretisation see for example Ref. [87]. In a real-space representation of the leads as in Eq. (2.19), a rearrangement of the discrete energy levels translates to a modification of the hopping matrix elements, which become position-dependent, $J \to J_x$. In this work we will use damped boundary conditions (DBC) that have repeatedly been applied before [30,60] in order to increase the energy resolution at the Fermi level ε_{F}, while keeping the overall number of lattice sites M fixed. We therefore modify the lead Hamiltonian[2] (2.19),

$$\hat{H}_{\mathrm{L}}^{\mathrm{DBC}} = -\sum_{\sigma,x=0}^{M_{\Lambda}-2} \Lambda^{-[M_{\Lambda}-(x-M_{\mathrm{B}}+2)]/2} J(\hat{c}_{\sigma x}^{\dagger}\hat{c}_{\sigma x+1} + \hat{c}_{\sigma x+1}^{\dagger}\hat{c}_{\sigma x})$$

$$- J\sum_{\sigma,x=M_{\Lambda}-1}^{M_{\mathrm{L}}-2} (\hat{c}_{\sigma x}^{\dagger}\hat{c}_{\sigma x+1} + \hat{c}_{\sigma x+1}^{\dagger}\hat{c}_{\sigma x}), \tag{2.23}$$

corresponding to the sketch in Fig. 2.4. The damping towards the boundaries exponentially reduces the level splitting at ε_{F} at half filling.[3] In chapter 5 we will study the enhanced energy resolution and give an interpretation in terms of an effectively

---

[2]Remark: We only show the modification for the left lead. The right lead has to be modified correspondingly.

[3]In fact, exponential damping is one of several possibilities to increase the energy resolution. Alternatively, smooth boundary conditions [59,88] can be used to mimic the thermodynamic limit.

left Lead   Structure

0   1 ... $M_\Lambda{-}1$ $M_L{-}1$

$\Lambda^{-M_\Lambda/2}J$ ...   ... $\Lambda^{-1/2}J$ J J J J J_C J_S

exponential   constant
damping   hopping

Figure 2.4 Damped boundary conditions (here: in the left lead). While keeping the overall number of lattice sites in the leads constant, the hopping matrix elements are damped towards the boundaries of the leads, with a damping parameter $\Lambda > 1$.

increased system size. The impact on finite size effects will be discussed in some detail, where we will focus on the effect on the time evolution of the system at finite bias voltage.

Chapter 3

Numerical Methods

This chapter is intended to give an overview of the numerical methods that build the basis for the computations, the results of which are presented in the remaining part of this work. In the light of the many different techniques that are in use we thereby have to concentrate on the basic principles, referring the interested reader to the literature for the details, for example Refs. [61,62,64–66,89–96]. Of course, all the topics discussed in this chapter have been studied before. However, we believe that in order to make this work self-contained, it is appropriate to address certain issues at this place due to their fundamental relevance in this context.

When investigating finite lattice models of electronic systems, the corresponding Hamiltonian (in fact, all operators that are relevant) can be represented in terms of matrices of finite dimension with complex entries, while quantum mechanical states can be represented as vectors with finite dimension. Many problems can be considered as solved when the eigenvalues and the corresponding eigenstates of a given Hamiltonian are known, being often sufficient to know only a few of them, such as the ground state of the system. Therefore numerical diagonalisation techniques play an important role, cf. section 3.1. However, the numerically exact diagonalisation is limited to very small systems of only a few lattice sites since the dimension of the underlying Hilbert space is growing very fast. Therefore, one may resort to iterative projective schemes that keep the dimension of the Hilbert space constant while repeatedly enlarging the system by adding (blocks of) lattice sites. A prominent example is the numerical renormalisation group (NRG) which is based on an iterative rescaling of the energy scale while keeping only the low lying energy eigenstates [97,98]. Because of the specific choice of states kept at each iteration step this method is tailor-made for problems which show a clear separation of energy scales, while it is not clear whether in a non-equilibrium situation the seperation of energy scales persists. Instead, we use the density matrix renormalisation group (DMRG) [61,62,64–66], cf. section 3.2, which is also based on iteratively enlarging the system size, but truncates the Hilbert space using a different selection criterion: only those states are kept which span a truncated Hilbert space that allows us to approximately represent an *arbitrary* set of states *optimally in a certain sense*, as will be discussed below. Given an initial non-equilibrium state it is then possible to compute the time evolution of the system. For this purpose different schemes have been developed [43–48,55]. In our case we use a method based on Krylov subspace

techniques [99] to obtain finite bias current and shot noise in chapter 5, which was first applied to electron transport in a 1D lattice on the basis of DMRG by Schmit- teckert [47]. The scheme preserves unitarity and can be accurate up to numerical precision (see section 3.3). Finally we investigate applications of orthogonal poly- nomials [89, 96] in the context of DMRG, highlighting some interesting features due to the possibility of expanding functions into a complete basis of polynomials, cf. section 3.4.

3.1 Applications of Exact Diagonalisation

The term "exact diagonalisation" in general refers to methods that yield numerically exact results for a finite lattice system by directly diagonalising the matrix represen- tation of the system's Hamiltonian [64]. This includes the complete diagonalisation of the matrix, which is either given in a many particle basis or which may result from a single particle decomposition as discussed below, but also iterative methods which make the ground state (as well as a few low lying excited states) available.

Unfortunately, for many-particle systems, the dimension of the underlying Hilbert space grows very fast with the size of the considered system. The description of an isolated electronic system that conserves particle number N and total magnetisation $S_{\text{tot}}^z = N_\uparrow - N_\downarrow$, where the number of spin up (spin down) electrons is given by $N_\uparrow$ ($N_\downarrow$), can be divided into parts with constant N and constant S_{tot}^z. The Hilbert space $\mathcal{V}(N, S_{\text{tot}}^z)$ for a given value of particle number and total magnetisation then has dimension

$$\dim(\mathcal{V}(N, S_{\text{tot}}^z)) = \binom{M}{N_\uparrow} \binom{M}{N_\downarrow} = \binom{M}{(N + S_{\text{tot}}^z)/2} \binom{M}{(N - S_{\text{tot}}^z)/2}. \quad (3.1)$$

Storing the complete matrix for a lattice with $M = 10$ lattice sites, $N_\uparrow = 5$, and $N_\downarrow = 5$, in double precision, will occupy about 15GB of RAM![1]

Given that only the extremal eigenstates are relevant, one can resort to the Lanc- zos or the Davidson method [64, 91]. By repeatedly applying the Hamiltonian on a given initial vector, a set of states $\{|\varphi_n\rangle\}$ is generated, which will eventually allow computation of the extremal eigenstates one is looking for. Since only the *action* of the Hamiltonian on a given state is computed, there is no need to store the whole ma- trix representation. Instead only the states $|\varphi_n\rangle$, which amount to $\dim(\mathcal{V}(N, S_{\text{tot}}^z))$ numbers in double precision, have to be stored. Still, for a system with $M = 18$ and $N_\uparrow = N_\downarrow = 9$, 18GB of RAM must be available *per vector*.

In the framework of the DMRG (cf. section 3.2), both, the complete as well as the iterative diagonalisation, are used. The projection of the many particle Hilbert space onto a subspace with a largely reduced dimension allows treatment of systems

---

[1]For many practical applications, as for example tight binding chains, only a small number of the matrix elements is different from 0. Therefore, sparse matrix techniques can be used to cut the memory footprint to a much smaller value.

with $M \gtrsim 100$ lattice sites. While low lying eigenstates of the Hamiltonian in the projected subspace have to be computed using iterative algorithms, complete diagonalisation is applied to obtain the complete eigenvalue spectrum of the reduced density matrix for a part of the system.

Single particle decomposition By contrast, for systems described by a Hamiltonian of the form[2]

$$\hat{H} = \sum_{x,y=1}^{M} H_{xy}\hat{c}_x^\dagger \hat{c}_y, \quad H_{xy}^* = H_{yx}, \tag{3.2}$$

a single particle representation can be obtained, which in contrast to the full N particle description allows treatment of systems with several thousand lattice sites.

In the remainder of this section we will derive formulas for computing expectation values of certain time-dependent operators. For the discussion of simulations of the time evolution in chapter 5 this is important, since it allows us to look for effects that result from the finite size of the system. Furthermore, the method described here allows us to check numerical results obtained by using other, more ambitious techniques, as for example the DMRG.

To begin with, we derive a single particle representation for the expectation value of the operator $\hat{c}_x^\dagger(t)\hat{c}_y(t)$, which is a prerequisite for calculating the time-dependent current in a non-equilibrium state. The fermionic operator $\hat{c}_x^\dagger$ *creates* a particle at the lattice site x, while the Hermitian conjugate *removes* a particle from the system. Therefore the particle number conserving operator $\hat{c}_x^\dagger \hat{c}_y$ can be referred to as a *hopping operator*. Let $|\varphi_N\rangle$ be a complete set of eigenstates for an N-particle system, where $E_N|\varphi_N\rangle = \hat{H}|\varphi_N\rangle = \sum_\kappa \epsilon_\kappa n_\kappa[\varphi_N]|\varphi_N\rangle$, with the one-particle energies ϵ_κ and the occupation number $n_\kappa[\varphi_N] \in \{0,1\}$ of the single particle level κ in the state $|\varphi_N\rangle$. Now, for a time-independent Hamiltonian $\hat{H}$, the time evolution operator $\exp(-\mathrm{i}\hat{H}t/\hbar)$ can be represented as

$$\mathrm{e}^{-\mathrm{i}\hat{H}t/\hbar} = \sum_{N=0}^{M} \sum_{\varphi_N} \mathrm{e}^{-\mathrm{i}\sum_\kappa \epsilon_\kappa n_\kappa[\varphi_N]t/\hbar} |\varphi_N\rangle\langle\varphi_N|, \tag{3.3}$$

where the sum extends over the full Fock space basis with dimension 2^M in the case of spinless electrons on a lattice whith M lattice sites. This allows us to express the time evolved hopping operator as

$$\mathrm{e}^{\mathrm{i}\hat{H}t/\hbar}\hat{c}_x^\dagger \hat{c}_y \mathrm{e}^{-\mathrm{i}\hat{H}t/\hbar} = \sum_{N,\varphi_N',\varphi_N} \mathrm{e}^{\mathrm{i}\sum_\kappa \epsilon_\kappa \{n_\kappa[\varphi_N']-n_\kappa[\varphi_N]\}t/\hbar} |\varphi_N'\rangle\langle\varphi_N'|\hat{c}_x^\dagger \hat{c}_y|\varphi_N\rangle\langle\varphi_N|. \tag{3.4}$$

If we finally introduce an appropriate unitary transformation $U_{x\alpha}$ that diagonalizes the matrix H_{xy} by $\epsilon_\alpha \delta_{\alpha\beta} = \sum_{xy} U_{\alpha x}^\dagger H_{xy} U_{y\beta}$, yielding the diagonal form of the

---

[2]Example: The resonant level model, described by the Hamiltonian (2.21), with $U_\mathrm{C} \equiv 0$, is of the form (3.2).

Hamiltonian (3.2),

$$\hat{H} = \sum_{\alpha} \epsilon_{\alpha} \hat{c}_{\alpha}^{\dagger} \hat{c}_{\alpha}, \quad \hat{c}_{\alpha} = \sum_{x} U_{\alpha x}^{\dagger} \hat{c}_{x}, \quad \hat{c}_{\alpha}^{\dagger} = \sum_{x} \hat{c}_{x}^{\dagger} U_{x\alpha}, \tag{3.5}$$

we arrive at a representation that does not contain a summation over the full Fock space basis anymore, but only over the single particle levels

$$\mathrm{e}^{\mathrm{i}\hat{H}t/\hbar} \hat{c}_{x}^{\dagger} \hat{c}_{y} \mathrm{e}^{-\mathrm{i}\hat{H}t/\hbar} = \sum_{\alpha\beta} U_{\alpha x}^{\dagger} U_{y\beta}\, \mathrm{e}^{\mathrm{i}(\epsilon_{\alpha}-\epsilon_{\beta})t/\hbar}\, \hat{c}_{\alpha}^{\dagger} \hat{c}_{\beta} = \sum_{x'y'} \hat{c}_{x'}^{\dagger} \mathcal{U}^{\dagger}(t)_{x'x} \mathcal{U}(t)_{yy'} \hat{c}_{y'}, \tag{3.6}$$

with the time evolution operator in the single particle representation[3]

$$\mathcal{U}(t) = \left[\sum_{\beta} U_{y\beta} \mathrm{e}^{-\mathrm{i}\epsilon_{\beta}t/\hbar} U_{\beta y'}^{\dagger} \right] = \mathrm{e}^{-\mathrm{i}Ht/\hbar}. \tag{3.7}$$

The matrix $\mathcal{U}$ can be obtained either by evaluating the sum (3.7), or directly from the matrix H_{xy} by means of a matrix exponential function, cf. Refs. [93–95], removing the need to explicitly compute the unitary transform $U_{x\alpha}$.

For an arbitrary initial state $|\Psi_0\rangle$, defined by the occupation numbers $\tilde{n}_{\nu}[\Psi_0] \in \{0,1\}$ of an *arbitrary* complete set of orthogonal single particle states, we now can express the expectation value $\langle \Psi_0 | \hat{c}_x^{\dagger}(t) \hat{c}_y(t) | \Psi_0 \rangle$ in terms of this single particle basis. Therefore we first introduce a second unitary transform U^0 that connects the annihilation and the creation operators $\hat{c}_x$, $\hat{c}_x^{\dagger}$ with an additional set of operators $\hat{c}_{\nu}^0$, $\hat{c}_{\nu}^{0\dagger}$, where the latter constitute the occupation number operators of the aforementioned single particle basis by $\hat{c}_{\nu}^{0\dagger} \hat{c}_{\nu}^0 |\Psi_0\rangle = \tilde{n}_{\nu}[\Psi_0] |\Psi_0\rangle$

$$\hat{c}_{\nu}^0 = \sum_{x} U_{\nu x}^{0\dagger} \hat{c}_{x}, \quad \hat{c}_{\nu}^{0\dagger} = \sum_{x} \hat{c}_{x}^{\dagger} U_{x\nu}^0. \tag{3.8}$$

In combination with Eq. (3.6), this finally leads to

$$\langle \Psi_0 | \hat{c}_x^{\dagger}(t) \hat{c}_y(t) | \Psi_0 \rangle = \sum_{x'y'\nu\mu} \langle \Psi_0 | \hat{c}_{\nu}^{0\dagger} \hat{c}_{\mu}^0 | \Psi_0 \rangle U_{\nu x'}^{0\dagger} \mathcal{U}^{\dagger}(t)_{x'x} \mathcal{U}(t)_{yy'} U_{y'\mu}^0 \tag{3.9}$$

$$= \sum_{x'y'\nu} \mathcal{U}(t)_{yy'} U_{y'\nu}^0 \tilde{n}_{\nu}[\Psi_0] U_{\nu x'}^{0\dagger} \mathcal{U}^{\dagger}(t)_{x'x} = \sum_{x'y'} \mathcal{U}(t)_{yy'} \Psi_0^{y'x'} \mathcal{U}^{\dagger}(t)_{x'x}, \tag{3.10}$$

$$\Psi_0^{y'x'} = \sum_{\nu} U_{y'\nu}^0 \tilde{n}_{\nu}[\Psi_0] U_{\nu x'}^{0\dagger}. \tag{3.11}$$

Eq. (3.10) is an important result of this section. In order to define the initial state $|\Psi_0\rangle$, we will later (cf. chapter 5) obtain the ground state of a Hamiltonian $\hat{H}_0 \neq \hat{H}$, which has the same form as given in Eq. (3.2) with a hermitian $M \times M$ matrix $H_{0,xy}$, by setting the occupation numbers $\tilde{n}_{\nu}$ of the N lowest single particle energy

---

[3]The matrix H has to be distinguished from the Hamiltonian $\hat{H}$, cf. Eq. (3.2).

eigenstates to 1, and of the $M - N$ upper eigenstates to 0. The unitary transform U^0 can be obtained by diagonalising $H_{0,xy}$ corresponding to Eq. (3.5).

Since we also want to compute shot noise, we need to evaluate the expectation value of operators of the form $\hat{c}_x^\dagger(t)\hat{c}_y(t)\hat{c}_{x'}^\dagger(t')\hat{c}_{y'}(t')$. After applying some commutator algebra, the generalisation of Eq. (3.10) is straightforward and amounts to

$$
\begin{aligned}
\langle \Psi_0 | \hat{c}_x^\dagger(t)&\hat{c}_y(t)\hat{c}_{x'}^\dagger(t')\hat{c}_{y'}(t') | \Psi_0 \rangle \\
&= \sum_{\bar{x}\bar{y}\check{x}\check{y}} \Big\{ \mathcal{U}(t)_{y\bar{y}} \Psi_0^{\bar{y}\bar{x}} \mathcal{U}^\dagger(t)_{\bar{x}x} \mathcal{U}(t')_{y'\check{y}} \Psi_0^{\check{y}\check{x}} \mathcal{U}^\dagger(t')_{\check{x}x'} \\
&\qquad\qquad - \mathcal{U}(t')_{y'\check{y}} \Psi_0^{\check{y}\check{x}} \mathcal{U}^\dagger(t)_{\bar{x}x} \mathcal{U}(t)_{y\bar{y}} \big(\Psi_0^{\bar{y}\check{x}} - \delta_{\bar{y}\check{x}} \big) \mathcal{U}^\dagger(t')_{\check{x}x'} \Big\}. \qquad (3.12)
\end{aligned}
$$

Finally we want to direct the readers attention to Ref. [100]. There, for non-interacting electrons in a one-dimensional tight-binding model the full counting statistics is evaluated numerically, which in principle allows for the extraction of current, noise as well as higher order cumulants.

## 3.2 Density Matrix Renormalisation Group (DMRG)

In general, the problem of diagonalising the Hamiltonian can not be reduced to a single particle picture. Instead, the full many-particle problem has to be considered. As already discussed in the previous section, the main difficulty here results from the dimension of the Hilbert space $\mathcal{V}$ growing very fast with the number M of lattice sites. In this section we will describe the density matrix renormalisation group (DMRG) method, which essentially reduces the dimension of the Hilbert space $\mathcal{V}$ by projecting onto a small subspace $\mathcal{V}_{\mathrm{cut}}$. The criterion for generating the projection scheme is based on minimizing the *discarded weight* of the reduced density matrix $\hat{\rho}_x$ of a part of the system, where the discarded weight is the sum of all eigenvalues of $\hat{\rho}_x$ which get lost during the projection onto $\mathcal{V}_{\mathrm{cut}}$.

The DMRG was introduced by Steven White in 1992 [61] in order to overcome problems with boundary errors that appear when Wilson's NRG [97] is applied to real space lattice problems. In keeping only the low-lying energy eigenstates, the NRG method fails to choose an appropriate set of basis states which can be used to represent the low lying states in a system of *increased size*. This is illustrated in Fig. 3.1 for the ground state of a particle on a lattice in a 1D box. For a discussion in more details see Ref. [101].

White applied the new method to 1D Heisenberg antiferromagnetic spin chains at zero temperature. Since then the method has been generalized to a number of problems, including finite temperature calculations [102, 103], 2D systems (for example [104]; for a more extensive list of references see [65]), and time evolution simulations of non-equilibrium states [43–48], the latter being fundamental to the

Figure 3.1

Ground state of a particle in a box on a discrete lattice. The black dots represent the lattice, which consists of $M = 8$ or $M' = 2 \cdot M = 16$ sites. An algorithm that looks for the ground state of the system by iteratively (a) looking for the low lying states in a Hilbert space $\mathcal{V}$ for a system of size M, (b) constructing a truncated Hilbert space $\mathcal{V}'$ for a system of increased size M' using the low lying states in $\mathcal{V}$ only, and (c) $M' \to M$, $\mathcal{V}' \to \mathcal{V}$, will fail since the ground state in $\mathcal{V}'$ can not be represented correctly.
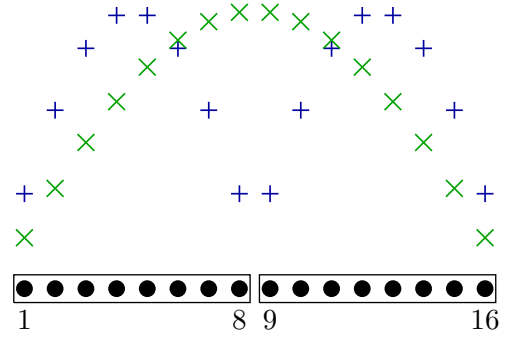
results of the present work. The method was also the topic of a number of reviews that have appeared in the last years [64–66].

3.2.1 Optimally truncated wave function

To define the truncation scheme that reduces the dimension of a given Hilbert space $\mathcal{V}$, we start with the following assumptions:

1. A number of states[4] $|\chi\rangle \in \mathcal{M} = \{|\Psi\rangle, |\Phi\rangle, |\Theta\rangle, \ldots\}$ of the many particle system with $\sqrt{\langle\chi|\chi\rangle} = \mathcal{N}_\chi$ is given in a product basis,[5]

$$|\chi\rangle = \sum_{i=0}^{D_A-1} \sum_{j=0}^{D_B-1} c_\chi^{ij} |\xi_A^i\rangle \otimes |\xi_B^j\rangle, \qquad (3.13)$$

with $|\xi_A^i\rangle$ a basis in $\mathcal{V}_A$ and $|\xi_B^j\rangle$ a basis in $\mathcal{V}_B$, where $\mathcal{V} = \mathcal{V}_A \otimes \mathcal{V}_B$, with $D_A = \dim(\mathcal{V}_A)$ and $D_B = \dim(\mathcal{V}_B)$,

2. the truncation is carried out separately in $\mathcal{V}_A$ and $\mathcal{V}_B$,

3. the truncated states $|\chi_{\text{cut}}\rangle$ must minimise

$$\sum_{\chi \in \mathcal{M}} \||\chi\rangle - |\chi_{\text{cut}}\rangle\|^2 / \mathcal{N}_\chi^2$$
$$= \||\Psi\rangle - |\Psi_{\text{cut}}\rangle\|^2 / \mathcal{N}_\Psi^2 + \||\Phi\rangle - |\Phi_{\text{cut}}\rangle\|^2 / \mathcal{N}_\Phi^2 + \||\Theta\rangle - |\Theta_{\text{cut}}\rangle\|^2 / \mathcal{N}_\Theta^2 + \ldots \qquad (3.14)$$

If we define a density operator for the states $|\chi\rangle \in \mathcal{M}$

$$\hat{\rho} = \sum_{\chi \in \mathcal{M}} \frac{1}{\mathcal{N}_\chi^2} |\chi\rangle\langle\chi|, \qquad (3.15)$$

---

[4]Example: for the time evolution of an initial non-equilibrium state $|\Psi_0\rangle$ vectors $|\Psi(t_n)\rangle = \exp(-i\hat{H}\Delta t/\hbar)^n |\Psi_0\rangle$ have to be computed, forming the set $\mathcal{M}$.

[5]The reason for this requirement will become clear in the following sections.
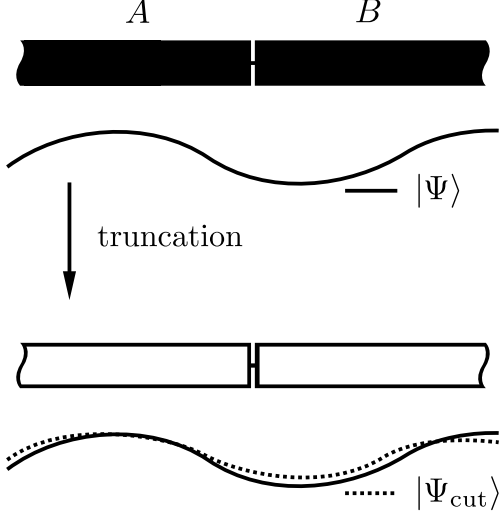
Figure 3.2
Truncation scheme. A wave function $|\Psi\rangle$ that is given in a product basis for subsystems A and B as described in Eq. (3.13) is truncated to a small subspace according to the minimality condition Eq. (3.14). The filled areas ● correspond to the full Hilbert space $\mathcal{V}_A$ and $\mathcal{V}_B$, whereas the framed areas ○ correspond to the Hilbert space $\mathcal{V}_{A,\text{cut}}$ and $\mathcal{V}_{B,\text{cut}}$ with reduced dimension. The resulting wave function $|\Psi_{\text{cut}}\rangle$ approximates the original one.

it turns out that the minimality condition (3.14) is fulfilled for a truncation that keeps those of the basis states in the subsystems A and B that are eigenstates of the reduced density operators $\hat{\rho}_A$ and $\hat{\rho}_B$ of $\hat{\rho}$ with the *largest* eigenvalues:

The reduced density operator $\hat{\rho}_A$ ($\hat{\rho}_B$) for the state of the subsystem A (B) is given as the trace over the disjoint subsystem

$$\hat{\rho}_A = \text{Tr}_B \hat{\rho} = \sum_{k=0}^{D_B-1} \sum_{l,m=0}^{D_A-1} |\xi_A^l\rangle \left[\langle\xi_A^l| \otimes \langle\xi_B^k| \right] \hat{\rho} \left[|\xi_A^m\rangle \otimes |\xi_B^k\rangle \right] \langle\xi_A^m|, \tag{3.16}$$

and

$$\hat{\rho}_B = \text{Tr}_A \hat{\rho} = \sum_{k=0}^{D_A-1} \sum_{l,m=0}^{D_B-1} |\xi_B^l\rangle \left[\langle\xi_A^k| \otimes \langle\xi_B^l| \right] \hat{\rho} \left[|\xi_A^k\rangle \otimes |\xi_B^m\rangle \right] \langle\xi_B^m|, \tag{3.17}$$

respectively. The matrix elements then are given as

$$\rho_A^{kl} = \sum_{\chi \in \mathcal{M}} \frac{1}{\mathcal{N}_\chi^2} \sum_i c_\chi^{ki} (c_\chi^{li})^* \quad \text{and} \quad \rho_B^{kl} = \sum_{\chi \in \mathcal{M}} \frac{1}{\mathcal{N}_\chi^2} \sum_i c_\chi^{ik} (c_\chi^{il})^*. \tag{3.18}$$

For the subsystem A, we introduce a new orthonormal basis set $|\tilde{\xi}_A^\alpha\rangle$ with

$$|\tilde{\xi}_A^\alpha\rangle = \sum_i u_{\alpha i} |\xi_A^i\rangle. \tag{3.19}$$

A truncation $|\chi_{\text{cut}}\rangle$ of the states $|\chi\rangle \in \mathcal{M}$ into a subspace $\mathcal{V}_{\text{cut}} = \mathcal{V}_{A,\text{cut}} \otimes \mathcal{V}_B \subseteq \mathcal{V}$ with $N_{\text{cut}} = \dim(\mathcal{V}_{A,\text{cut}}) \leq D_A$ is now given by

$$|\chi_{\text{cut}}\rangle = \sum_{\alpha=0}^{N_{\text{cut}}-1} \sum_j a_\chi^{\alpha j} |\tilde{\xi}_A^\alpha\rangle \otimes |\xi_B^j\rangle. \tag{3.20}$$

This truncation is *optimal*, if the minimality condition (3.14) is fulfilled, which we can rewrite as

$$1-2\mathrm{Re}\left[\sum_{\chi\in\mathcal{M}}\frac{1}{\mathcal{N}_\chi^2}\sum_{\alpha=0}^{N_{\mathrm{cut}}-1}\sum_{ij}(c_\chi^{ij})^*a_\chi^{\alpha j}u_{\alpha i}\right]+\sum_{\chi\in\mathcal{M}}\frac{1}{\mathcal{N}_\chi^2}\sum_{\alpha=0}^{N_{\mathrm{cut}}-1}\sum_j\left|a_\chi^{\alpha j}\right|^2 \ \mathrm{minimal.} \quad (3.21)$$

A necessary condition is *stationarity* of Eq. (3.21) with reference to the coefficients $a_\chi^{\alpha j}$

$$\Rightarrow \quad a_\chi^{\alpha j}\overset{!}{=}\sum_i c_\chi^{ij}(u_{\alpha i})^*. \quad (3.22)$$

Putting this into Eq. (3.21) we find

$$1-2\mathrm{Re}\left[\sum_{\chi\in\mathcal{M}}\frac{1}{\mathcal{N}_\chi^2}\sum_{\alpha=0}^{N_{\mathrm{cut}}-1}\sum_{ij}(c_\chi^{ij})^*a_\chi^{\alpha j}u_{\alpha i}\right]+\sum_{\chi\in\mathcal{M}}\frac{1}{\mathcal{N}_\chi^2}\sum_{\alpha=0}^{N_{\mathrm{cut}}-1}\sum_j\left|a_\chi^{\alpha j}\right|^2$$

$$=\quad 1-\sum_{\chi\alpha ii'j}\frac{1}{\mathcal{N}_\chi^2}(u_{\alpha i})^*c_\chi^{ij}(c_\chi^{i'j})^*u_{\alpha i'}\overset{(3.18)}{=}1-\sum_{\alpha ii'}(u_{\alpha i})^*\rho_A^{ii'}u_{\alpha i'} \quad (3.23)$$

$$\overset{(3.19)}{=}\quad 1-\sum_{\alpha=0}^{N_{\mathrm{cut}}-1}\langle\tilde{\xi}_A^\alpha|\hat{\rho}_A|\tilde{\xi}_A^\alpha\rangle \ \ \mathrm{minimal.} \quad (3.24)$$

Finally, we have to fix the basis $|\tilde{\xi}_A^\alpha\rangle$. Now, minimality requires stationarity with reference to the $|\tilde{\xi}_A^\alpha\rangle$. According to the Rayleigh-Ritz variational principle, $\langle\tilde{\xi}_A^\alpha|\hat{\rho}_A|\tilde{\xi}_A^\alpha\rangle$ is stationary for the basis states $|\tilde{\xi}_A^\alpha\rangle$ being the *eigenvectors* of the density operator $\hat{\rho}_A$. In order to obtain this basis and the corresponding eigenvalues it is necessary to apply a complete diagonalisation to the density operator. If we denote by w_A^α the eigenvalues of $\hat{\rho}_A$, we find the minimality condition fulfilled if

$$1-\sum_{\alpha=0}^{N_{\mathrm{cut}}-1}\langle\tilde{\xi}_A^\alpha|\hat{\rho}_A|\tilde{\xi}_A^\alpha\rangle=1-\sum_{\alpha=0}^{N_{\mathrm{cut}}-1}w_A^\alpha\equiv\varepsilon_A \quad (3.25)$$

only contains the N_{cut} *biggest eigenvalues* of the density operator. The error of this truncation is controlled by the truncation error ε_A, which we will in general denote as the *discarded weight* $\varepsilon_{\mathrm{disc}}$. The same argument holds true for the density operator $\hat{\rho}_B$ of the subsystem B.

In order to construct an optimally truncated Hilbert space $\mathcal{V}_{\mathrm{cut}}=\tilde{\mathcal{V}}_{A,\mathrm{cut}}\otimes\tilde{\mathcal{V}}_{B,\mathrm{cut}}$ (optimal in the sense described before), we therefore have to find a unitary transform $|\xi_A^l\rangle\rightarrow|\tilde{\xi}_A^\alpha\rangle$ and $|\xi_B^m\rangle\rightarrow|\tilde{\xi}_B^\beta\rangle$ that *diagonalises* the reduced density operators $\hat{\rho}_A$ and $\hat{\rho}_B$. Then, the new basis has to be truncated to those states with the biggest eigenvalues w_A^α and w_B^β.

Entanglement The *entanglement entropy* for the subsystem $x = A, B$, which is a measure for the entanglement of the two subsystems, can be defined as the von Neumann entropy of a reduced density matrix

$$\mathcal{S}_x = -\text{Tr}\hat{\rho}_x \log_2 \hat{\rho}_x. \tag{3.26}$$

For example, if we think of a totally disentangled state $|\Psi\rangle = |\Psi_A\rangle \otimes |\Psi_B\rangle$, the reduced density operator $\hat{\rho}_x$ for the subsystem $x = A, B$ is given as $\rho_x = |\Psi_x\rangle\langle\Psi_x|$. The entropy then equals to zero. In general any state that has the form given in Eq. (3.13) can be written as[6]

$$|\chi\rangle = \sum_{i=0}^{D_A-1} \sum_{j=0}^{D_B-1} c_\chi^{ij} |\xi_A^i\rangle \otimes |\xi_B^j\rangle \tag{3.27}$$

$$= \sum_{ij} \sum_{\alpha=0}^{D_A-1} \sum_{\beta=0}^{D_B-1} \left[U_{i\alpha} \Sigma_\chi^{\alpha\beta} V_{\beta j}^\dagger \right] |\xi_A^i\rangle \otimes |\xi_B^j\rangle \tag{3.28}$$

$$= \sum_{\alpha=0}^{D^*-1} \Sigma_\chi^{\alpha\alpha} |\bar{\xi}_A^\alpha\rangle \otimes |\bar{\xi}_B^\alpha\rangle, \quad D^* = \min(D_A, D_B). \tag{3.29}$$

The matrix elements of the reduced density operator then read

$$\rho_A^{\alpha\beta} = \rho_B^{\alpha\beta} = \frac{1}{\mathcal{N}_\chi} (\Sigma_\chi^{\alpha\alpha})^2 \delta_{\alpha\beta} \overset{!}{=} w_\chi^\alpha \delta_{\alpha\beta}, \tag{3.30}$$

identifying $\Sigma_\chi^{\alpha\beta} \equiv \sqrt{\mathcal{N}_\chi w_\chi^\alpha} \delta_{\alpha\beta}$. Additionally, based on the equivalence of the eigenvalue spectrum of the reduced density matrices for the two subsystems it may be concluded that[7]

$$\mathcal{S} \equiv \mathcal{S}_A \equiv \mathcal{S}_B. \tag{3.31}$$

The truncation scheme described above, applied to a pure state $|\chi\rangle$, therefore leads to a state $|\chi_{\text{cut}}\rangle$ with *reduced* entanglement $(N_{\text{cut}} \leq D^*)$

$$|\chi_{\text{cut}}\rangle = \sum_{\alpha=0}^{N_{\text{cut}}-1} \Sigma_\chi^{\alpha\alpha} |\bar{\xi}_A^\alpha\rangle \otimes |\bar{\xi}_B^\alpha\rangle, \quad \mathcal{S}_{\text{cut}} = -\sum_{\alpha=0}^{N_{\text{cut}}-1} w_\chi^\alpha \log_2 w_\chi^\alpha \equiv \mathcal{S} - \mathcal{S}_{\text{disc}}, \tag{3.32}$$

where we define the *discarded entropy* as

$$\mathcal{S}_{\text{disc}} = -\sum_{\alpha=N_{\text{cut}}}^{D^*-1} w_\chi^\alpha \log_2 w_\chi^\alpha, \tag{3.33}$$

the latter a measure for the information that is lost due to the truncation of the state. The minimality condition (3.14) guarantees that the loss of information $\mathcal{S}_{\text{disc}}$ for a pure state that entangles the both subsystems also is minimised.

---

[6]Using a singular value decomposition, the $D_A \times D_B$ matrix c_χ^{ij} can be expressed as $c_\chi^{ij} = \sum_{\alpha\beta} U_{i\alpha} \Sigma_\chi^{\alpha\beta} V_{\beta j}^\dagger$, with unitary matrices U and V and a diagonal $D_A \times D_B$ matrix Σ_χ with real, non-negative entries.

[7]It is well known that entropy is maximised if $w^\alpha = 1/D^*$. Therefore a pure state with maximum entanglement entropy can be written as $|\Psi\rangle = \sum_{\alpha=0}^{D^*-1} |\bar{\xi}_A^\alpha\rangle \otimes |\bar{\xi}_B^\alpha\rangle / \sqrt{D^*}$.

Errors During the DMRG iteration scheme, which will be described below, this truncation procedure is repeatedly applied to subsystems A and B of varying size which leads to an iterative accumulation of discarded weight $\varepsilon_{\mathrm{disc}}$. The resulting approximation is optimal in the sense of a least squares approximation, as lined out above. A big value of $\varepsilon_{\mathrm{disc}}$ leads to a big mismatch of the projected states $|\chi_{\mathrm{cut}}\rangle$ as compared to the original ones. Therefore it is crucial that the ordered weights w_x^α of the reduced density matrix $\hat{\rho}_x$ decay to zero fast.[8] On the other hand, since the complete spectrum of the reduced density matrices is computed in each iteration step, the truncation error can be steadily observed. The number of kept states N_{cut} then is an appropriate parameter to control $\varepsilon_{\mathrm{disc}}$.

The entanglement entropy recently has attracted a lot of interest [105]. For 1D systems, the scaling of $\mathcal{S}$ with respect to the length l of a subsystem x has been investigated. The entanglement entropy scales as

$$\mathcal{S}(l) \sim \mathrm{const} + \log l^*. \tag{3.34}$$

In the case of a gapped system, l^* is equivalent to the correlation length ξ, and hence independent of the size l of the subsystem x. In the case of an ungapped system, l^* is equivalent to the length l of the subsystem itself. For the present work, the latter case is relevant, since the models we want to study are gapless. The truncation procedure therefore leads to logarithmic growth of the disarded entropy for fixed N_{cut}. Increasing the dimension of the system > 1 leads to a modification of the scaling behaviour. For a gapped system, $\mathcal{S}$ scales linearly with the number of contact links A between the subsystem and the environment (area law; cf. also Ref. [105]).[9]

For time evolution simulations, we have to take into account that the evolution of an initial non-equilibrium state leads to the production of entanglement entropy. For a DC-biased quantum point contact, for example, it has been shown [74, 106] that the production rate is constant, $\partial\mathcal{S}/\partial t = \mathrm{const}$, in the long-time limit.

3.2.2 DMRG iteration scheme: infinite lattice algorithm

We are now ready to describe the algorithm that iteratively builds up a truncated Hilbert space together with the relevant wave functions, starting from a small system, by adding more and more lattice sites to the system [61]. The key ingredient here is to apply the truncation scheme described above subsequent to adding lattice sites in order to keep the dimension of the Hilbert space suitable.

1. Initially the system is divided into two equal subsystems (blocks) A and B which are composed of only a few ($l_A = M_{0,A}$, $l_B = M_{0,B}$) lattice sites. The particle number in the coupled subsystems can vary, therefore the dimension of

---

[8]A maximally entangled state, cf. footnote 7, will always lead to a bad approximation, if the discussed projection scheme is applied.

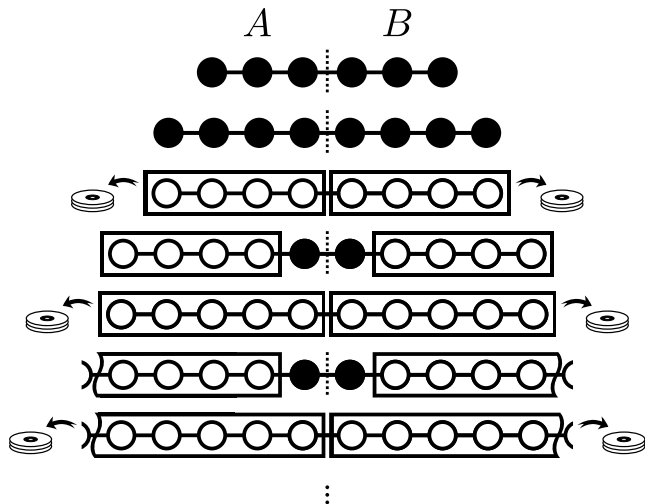[9]For this reason it is favourable to represent the leads as 1D tight-binding chains, cf. chapter 2.

Figure 3.3
DMRG infinite lattice algorithm. Starting from a small system (here: 3 sites in block A and B), the reduced Hilbert space is constructed iteratively by adding lattice sites ($A \rightarrow A\bullet$, $B \rightarrow \bullet B$) and subsequently truncating the subspaces to the desired dimension N_{cut} ($A\bullet \rightarrow A$, $\bullet B \rightarrow B$). Fig. 3.2. The truncated blocks must be stored 💾 for later usage during application of the finite size algorithm.

the Hilbert space of each of the subsystems $x = A, B$ is $D_x = d^{M_{0,x}}$, provided that each lattice site has dimension d. Let us denote the complete basis of each subsystem as $\{|m_x\rangle\}$. The first iteration then starts

2. by adding a lattice site to both blocks, resulting in new blocks $A\bullet$ and $\bullet B$. The additional sites are represented by a local basis $\{|\sigma_x\rangle\}$, the new basis of the enlarged blocks is equivalent to the set of product states, $\{|M_x\rangle = |m_x\rangle \otimes |\sigma_x\rangle\}$, which has dimension $D'_x = D_x \cdot d$. For the enlarged system one now has to find the ground state $|\Psi_0\rangle$ (and the low lying excited states, if desired) of the corresponding Hamiltonian by means of exact diagonalisation, which can be done using an iterative method, cf. the previous section. The full matrix representation of the Hamiltonian in the product basis $\{|M_A\rangle \otimes |M_B\rangle\}$ has $(D'_A \cdot D'_B)^2$ entries; note, however, that this number can be considerably reduced by employing restrictions like the overall conserved particle number and the total magnetisation, permitting to discard basis states of the product basis that do not match the restriction.

3. Then apply operators $\hat{O}$ to $|\Psi_0\rangle$ to obtain additional states $|\Phi\rangle = \hat{O}|\Psi_0\rangle$, where $\hat{O}$ can be any observable, creation / annihilation operator, time evolution operator, etc. At this point, expectation values can also be calculated.[10]

4. The ground state $|\Psi_0\rangle$ (as well as the low lying excited states) and, if available, the states $|\Phi\rangle$ from the previous step, are represented in the product basis $\{|M_A\rangle \otimes |M_B\rangle\}$ *by construction.* From this set of states form a density operator $\hat{\rho}$, as well as the reduced density operators $\hat{\rho}_{A\bullet}$ and $\hat{\rho}_{\bullet B}$. For $x = A\bullet$ and $x = \bullet B$,

   a) diagonalise $\hat{\rho}_x$ to obtain a basis of eigenvectors $|w_x^\alpha\rangle$ with eigenvalues w_x^α,

---

[10]This step can be omitted and only be applied during the finite lattice algorithm, cf. section 3.2.3.

b) keep only N_{cut} basis states with the biggest weights w_x^α and transform all states and operators to this reduced basis.

This now corresponds to finding the *optimally truncated basis* as outlined in the previous section. The full matrix representation of the reduced density operators $\hat\rho_x$ has $D_x'^2$ entries. Again, conserved quantities can be employed to realize that the matrix has block diagonal structure, where each block is labelled by a corresponding set of conserved quantum numbers (as, for example, particle number in block x), removing the need to store all of the matrix elements.

5. Replace $A\bullet \to A$ and $\bullet B \to B$, increasing the size of the blocks $l_x \to l_x + 1$, and start the next iteration $(\to 2. \ldots)$

This scheme is illustrated in Fig. 3.3. The iteration is stopped when the desired system size is reached.

3.2.3 DMRG iteration scheme: finite lattice algorithm

The infinite lattice algorithm has one major drawback. The projection to a small subspace discards a large number of states, which can lead to poor precision if some of the discarded states become important again at a later stage of the iteration procedure. Finding the ground state of a given system then is impossible since the relevant portion of the Hilbert space has been projected away in previous iterations.

For the infinite lattice algorithm, the discarded states are lost forever. This can be cured to a great extent using the finite lattice algorithm after the final system size has been approached. The main difference to the infinite lattice algorithm is constituted in *shrinking* of one of the blocks (say, B) while the other one (say, A) grows further – the overall system size is kept fixed. It is important to note that the properties of the shrinked block have been obtained before, either during the infinite lattice algorithm or during a preceeding finite lattice algorithm iteration step. As illustrated in Figs. 3.3, 3.4, the blocks of *reduced* size have been stored (as indicated by 🖫) and can now be restored during the finite size iterations. The truncation scheme here is applied only for the growing block, which has reached its maximum size when the shrinking block can be computed exactly (cf. Fig. 3.4). At this point, a *sweep* has been completed. The direction of growth and shrinking then has to be reversed. The sweeps should be repeated until the results (for example the expectation values of operators) have converged. This may take several sweeps, experience tells us to perform at least 5 sweeps.[11]

---

[11]For obtaining the ground state of a system, we typically use 11 sweeps, while for the time evolution simulations in chapter 5, this number may be increased by an order of magnitude.
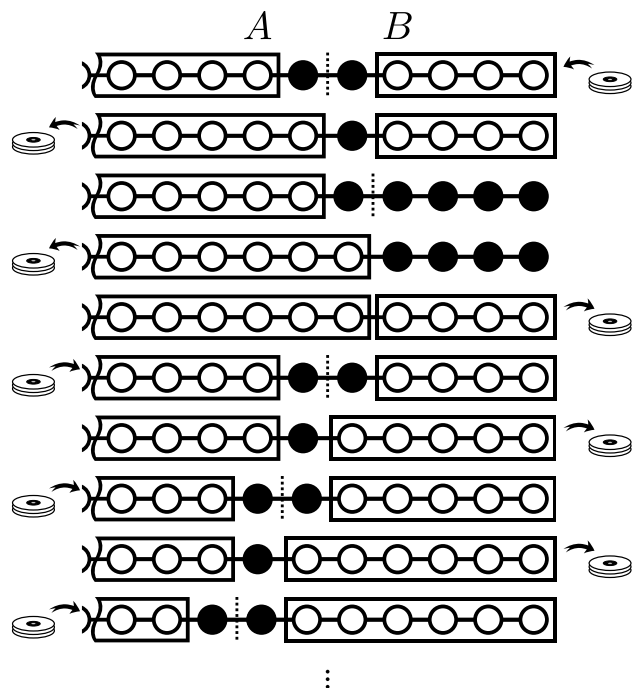
Figure 3.4
DMRG finite lattice algorithm. In contrast to the infinite lattice algorithm, the overall system size is fixed. ⊜ indicates either that data for the corresponding block has been computed before and can now be restored for further processing, or that recently computed data has to be stored for processing during a subsequent iteration step.

3.3 Time Evolution: the Krylov Subspace Method

The dynamics of a quantum mechanical system is described by the time-dependent Schrödinger equation [107]. For a time-independent Hamiltonian $\hat{H}$, this equation can formally be solved by introducing a time evolution operator $\hat{U}(t) = \exp(-\mathrm{i}\hat{H}t/\hbar)$, which then acts on an initial state $|\Psi\rangle$ to generate a time evolved state

$$|\Psi(t)\rangle = \hat{U}(t)|\Psi\rangle. \tag{3.35}$$

This time evolved state then can be used to compute the expectation value of time-dependent observables $\hat{A}(t)$ via

$$\langle\hat{A}(t)\rangle = \langle\Psi|\hat{U}^{\dagger}(t)\hat{A}\hat{U}(t)|\Psi\rangle, \quad \langle\hat{A}(t')\hat{A}(t)\rangle = \langle\Psi|\hat{U}^{\dagger}(t')\hat{A}\hat{U}(t'-t)\hat{A}\hat{U}(t)|\Psi\rangle, \tag{3.36}$$

etc. The numerical computation of the results of the time evolution simulations of current in interacting nanostructures presented in chapter 5 therefore depends on the availability of a method to obtain the action of an operator function (here: the time evolution operator) on a given state $|\Psi\rangle$. A very simple method consists in taylor-expanding the function f up to a certain order n, yielding an order n polynomial, which allows us to obtain $f(\hat{A})|\Psi\rangle$ approximately by knowledge of the expansion coefficients. However, this approximation leads to poor precision (or vice versa the need for a very high order n). Instead, it is desirable to implement a method that looks for a "better" polynomial approximation.

The Krylov subspace method [99] in combination with an orthogonalization scheme is a powerful tool to obtain a small subspace $\mathcal{K}$ of a given vector space $\mathcal{V}$, that contains the "most important" portion of the full space for a given problem. This

projection then can be used to obtain the quantity of interest efficiently, due to its reduced dimension.

Since we are looking for the action of a matrix function $f(\hat{A})$ on a given vector $|\Psi\rangle$, it is reasonable to ask for

$$|\Psi\rangle \in \mathcal{K}. \tag{3.37}$$

The definition of a matrix function in terms of the power series $f(z) = \sum_{j=0}^{\infty} c_j z^j$ also suggests

$$\hat{A}^j |\Psi\rangle \in \mathcal{K}. \tag{3.38}$$

The formal definition of the Krylov subspace $\mathcal{K}_r^{\hat{A},\Psi} \subseteq \mathcal{V}$ with $\dim(\mathcal{K}_r^{\hat{A},\Psi}) = r \leq \dim(\mathcal{V}) = d$,[12] generated by the operator $\hat{A}$ and the vector $|\Psi\rangle$, reads

$$\mathcal{K}_r^{\hat{A},\Psi} = \mathrm{span}\{|\Psi\rangle, \hat{A}|\Psi\rangle, \hat{A}^2|\Psi\rangle, \dots, \hat{A}^{r-1}|\Psi\rangle\}. \tag{3.39}$$

Therefore, any polynomial $p_{r-1}(z) = \sum_{j=0}^{r-1} b_j z^j$ of order $r-1$ generates an element of $\mathcal{K}_r^{\hat{A},\Psi}$ by

$$p_{r-1}(\hat{A})|\Psi\rangle \in \mathcal{K}_r^{\hat{A},\Psi}. \tag{3.40}$$

An orthogonal basis $|j\rangle$ in the subspace $K_r^{\hat{A},\Psi}$ can be constructed using an Arnoldi type algorithm [92], which also gives the matrix elements A_{ij} of $\hat{A}$ in this basis:

1. *Initialize:* Compute $|0\rangle = |\Psi\rangle / \sqrt{\langle \Psi | \Psi \rangle}$

2. *Iterate:* For basis state $|j\rangle$ with $j = 0 \dots r - 1$ repeat
   a) Compute $|\phi\rangle := \hat{A}|j\rangle$
   b) *Iterate:* Orthogonalize $|\phi\rangle$ on $|i\rangle$ with $i = 0 \dots j$ by repeating
      i. Compute $A_{ij} := \langle i|\phi\rangle = \langle i|\hat{A}|j\rangle$
      ii. Compute $|\phi\rangle := |\phi\rangle - A_{ij}|i\rangle$
   c) Compute $A_{j+1,j} := \sqrt{\langle \phi|\phi\rangle}$ and $|j+1\rangle = |\phi\rangle / A_{j+1,j}$.

This algorithm constructs an $r \times r$ upper Hessenberg matrix (tridiagonal matrix) A_{ij} for arbitrary (hermitian) operators $\hat{A}$, plus an additional $A_{r,r-1}$. Also, an orthonormal basis $\{|0\rangle, |1\rangle, \dots, |r-1\rangle\}$ of $\mathcal{K}_r^{\hat{A},\Psi}$ is computed, plus an additional vector $|r\rangle$. Since $\hat{A}|j\rangle \in \mathcal{K}_{j+2}^{\hat{A},\Psi} \subseteq \mathcal{K}_r^{\hat{A},\Psi}$, where $\mathcal{K}_{j+2}^{\hat{A},\Psi} = \mathrm{span}\{|0\rangle, |1\rangle, \dots, |j+1\rangle\}$, we know that

$$\langle i|\hat{A}|j\rangle = 0 \quad \forall \; i > j + 1. \tag{3.41}$$

Therefore

$$\hat{A}|j\rangle = \sum_{i=0}^{j+1} |i\rangle\langle i|\hat{A}|j\rangle = \sum_{i=0}^{r} |i\rangle\langle i|\hat{A}|j\rangle = \sum_{i=0}^{r-1} |i\rangle A_{ij} + |r\rangle A_{rj} \tag{3.42}$$

where $\langle i|\hat{A}|j\rangle = A_{ij}$ and $A_{rj} = A_{r,r-1}\delta_{j,r-1}$. Now, the matrix A_{ij} represents the projection of the operator $\hat{A}$ onto the Krylov subspace $\mathcal{K}_r^{\hat{A},\Psi}$ with respect to the

---

[12]If $\mathcal{V}$ decomposes into invariant subspaces w.r.t. $\hat{A}$, then $\dim(\mathcal{K}_r^{\hat{A},\Psi}) \leq r$.

given basis. If we denote the $d \times r$ matrix containing the r basis vectors $|j\rangle$ as columns as $B = [|0\rangle, |1\rangle, \ldots, |r-1\rangle]$, Eq. (3.42) translates to

$$\hat{A}B = BA + |r\rangle\langle r|\hat{A}B \quad \Rightarrow \quad A = B^\dagger \hat{A}B. \tag{3.43}$$

The projection operator of $\mathcal{V}$ on $\mathcal{K}_r^{\hat{A},\Psi}$ is given as $BB^\dagger$. If the considered function f is a polynomial of order $r-1$,

$$f(z) = p_{r-1}(z) = \sum_{k=0}^{r-1} c_k z^k, \tag{3.44}$$

the application of the corresponding matrix function evaluates to ($\beta = \sqrt{\langle\Psi|\Psi\rangle}$)

$$
\begin{aligned}
p_{r-1}(\hat{A})|\Psi\rangle &= \underbrace{\beta \sum_{k=0}^{r-1} c_k \hat{A}^k |0\rangle}_{\in \mathcal{K}_r^{\hat{A},\Psi}} = \beta \sum_{k=0}^{r-1} c_k BB^\dagger \hat{A}^k BB^\dagger |0\rangle \tag{3.45} \\
&= \beta \sum_{k=0}^{r-1} c_k B(B^\dagger \hat{A}B)^k B^\dagger |0\rangle = \beta B \sum_{k=0}^{r-1} c_k A^k B^\dagger |0\rangle \tag{3.46} \\
&= \beta B p_{r-1}(A) B^\dagger |0\rangle, \tag{3.47}
\end{aligned}
$$

where the equality $B^\dagger \hat{A}^k BB^\dagger |0\rangle = (B^\dagger \hat{A}B)^k B^\dagger |0\rangle$ is valid since $\hat{A}^k|0\rangle \in \mathcal{K}_{r-1}^{\hat{A},\Psi}$ for all $k \leq r-1$.[13]

For a general matrix function, given by an infinite power series $f(z) = \sum_{k=0}^{\infty} c_k z^k$, we now take the expression

$$f(\hat{A})|\Psi\rangle \approx \beta B f(A) B^\dagger |0\rangle \tag{3.48}$$

as an *approximation* to the exact value $f(\hat{A})|\Psi\rangle$. The interested reader may find a formal proof of the validity for the matrix exponential function in Ref. [92] where also error estimates are given. For practical computations especially the a posteriori error estimates matter since they allow us to determine "on the fly" whether the Krylov iteration can be stopped. The evaluation of the *full* matrix function $f(A)$ for the projected representation A of the operator $\hat{A}$ has to be carried out by means of other techniques, where we resort to the Padé approximation for the computation of the matrix exponential [93–95].

3.4 Polynomial Expansion

An alternative approach to evaluating the expectation value of operator functions is based on the expansion in terms of orthogonal polynomials. In contrast to the Krylov

---

[13]Note: $B^\dagger |0\rangle = (1, 0, 0, \ldots, 0)$.

method, the expectation value is not evaluated directly during the DMRG procedure but only as a second step, where the *polynomial moments* in combination with the *expansion coefficients* have to be summed up to constitute a specific function. The computationally expensive operations, as for example matrix-vector products, which build the basis for both the Krylov method as well as the evaluation of the polynomial moments, have to be carried out only *once* for different function parameters and even for *different functions* in the latter case, which can lead to a significant advantage over the Krylov approach.

In this section we want to discuss the application of the truncated series expansion of certain functions: the exponential functions $\exp(-\mathrm{i}xt)$ and $\exp(-\beta x)$, as well as $1/(z-x)$ with $x \in \mathbb{R}$, $\mathrm{Im}(z) \neq 0$. While the exponential function is suitable for time evolution simulations, or, in case of real-valued exponents, for the computation of thermodynamic quantities, $1/(z-x)$ can be used to evaluate resolvent expressions.

Closely related to the polynomial expansion is the so-called *kernel polynomial method* (KPM), which aims at eliminating Gibbs oscillations that occur when approximating non-continuous functions, such as the step function or the δ function, by truncated polynomial series [96]. Especially when computing the spectral density of a physical system which is represented by a finite matrix (cf. chapter 4), this is an important issue. Basically, the KPM modifies the expansion coefficients of the polynomial expansion of a given function, where the modification depends on the truncation order of the expansion. This is equivalent to a convolution of the function with an appropriate kernel. In the case of Green's functions, the KPM can be used to guarantee certain properties of the truncated series expansion, such as the poles being situated in the upper (lower) half of the complex plane for a retarded (advanced) Green's function. However, we choose another path to compute the spectral density. As pointed out before, resolvent expressions of the form $(E_0 - \hat{H} \pm \hbar(\omega + \mathrm{i}\eta))^{-1}$, $\eta > 0$, can be represented by $1/(z-x)$ when replacing $z \rightarrow \pm\hbar(\omega + \mathrm{i}\eta)$, $x \rightarrow \hat{H} - E_0$. In the limit $\eta \rightarrow 0^+$, the spectral density of the operator $\hat{H}$ is recovered by taking the imaginary part of this function – remember $\delta(\omega - x) = -1/\pi \lim_{\eta \rightarrow 0^+} \mathrm{Im}(\omega + \mathrm{i}\eta - x)^{-1}$. On the other hand, leaving η at a finite value corresponds to convoluting the δ-function with a Lorentzian, removing the discontinuity at $\omega = x$. Since we seek the broadened Green's function for reasons discussed later,[14] we do not rely on kernel polynomials but can apply the "pure" polynomial approximation, which yields a spectral function of which the broadening is well controlled by the parameter η.

Let us first recall the basic properties of expansions in orthogonal polynomials. For $w(x)$ being a positive weight function on the interval $[l, r]$, we define a scalar

---

[14]The broadened Green's function also suffers from the Gibbs oscillation problem. However, in contrast to the δ function, here we can give a truncation criterion for the series expansion that allows us to suppress the Gibbs oscillations in a controlled way. See below.

product,

$$(f, g) = \int\limits_{l}^{r} \mathrm{d}x \ w(x) f(x) g(x), \tag{3.49}$$

where $f, g : [l, r] \rightarrow \mathbb{R}$ integrable. There is a complete set of polynomials $p_n(x)$ with the properties

$$(p_n, p_m) = \delta_{nm}/h_n, \qquad h_n = 1/(p_n, p_n). \tag{3.50}$$

This now allows for an expansion of a given function f in terms of the p_n

$$f(x) = \sum_{n=0}^{\infty} \alpha_n p_n(x), \qquad \alpha_n = (p_n, f) h_n. \tag{3.51}$$

The series expansion may then be used to determine the expectation value of operator functions

$$\langle \Psi | f(\hat{O}) | \Psi \rangle = \sum_{n=0}^{\infty} \alpha_n \mu_n, \qquad \mu_n = \langle \Psi | n \rangle, \qquad | n \rangle = p_n(\hat{O}) | \Psi \rangle, \tag{3.52}$$

for operators $\hat{O}$ with a spectrum on the interval (l, r), where the vectors $|n\rangle$ can be obtained in linear time due to the recursion relations [89] for orthogonal polynomials

$$a_n^1 p_{n+1}(x) = (a_n^2 + a_n^3 x) p_n(x) - a_n^4 p_{n-1}(x)$$
$$\Rightarrow \quad a_n^1 | n + 1 \rangle = a_n^2 | n \rangle + a_n^3 \hat{O} | n \rangle - a_n^4 | n - 1 \rangle, \tag{3.53}$$

with numbers a_n^1, a_n^2, a_n^3 and a_n^4. The sequence (3.53) has the initial conditions

$$|0\rangle = p_0 |\Psi\rangle, \quad |1\rangle = p_1(\hat{O}) |\Psi\rangle. \tag{3.54}$$

The weight function $w(x)$, the normalisations h_n and the recurrence relation given by the p_0, $p_1(x)$ and a_n^i are specific for the type of polynomials and define them uniquely; compare also table 3.1 and Ref. [89]. While the polynomial moments μ_n have to be evaluated during the DMRG procedure based on the recurrence relation (3.53), the expectation value (3.52) of a function f is computed afterwards based on the expansion coefficients α_n as well as the μ_n, where the α_n have to be determined for the specific function f.

3.4.1 Properties of Chebyshev and Laguerre Polynomials

Chebyshev polynomials turn out to be the best choice for many applications [96]. However, numerical instabilities can lead to a limitation of the precision, as will be discussed later for the example of the real-valued exponential function $\exp(-\beta x)$. Therefore we also include the Laguerre polynomials in our discussion. While less favourable in terms of convergence of the expansion coefficients, we still obtain better results based on the Laguerre expansion as compared to the Chebyshev expansion.

$p_n(x)$	$[l, r]$	$w(x)$	h_n	p_0	p_1	a_n^1	a_n^2	a_n^3	a_n^4
$L_n^\alpha(x)$	$[0, \infty]$	$\mathrm{e}^{-x} x^\alpha$	$\dfrac{n!}{\Gamma(\alpha + n + 1)}$	1	$1 + \alpha - x$	$n+1$	$2n + \alpha + 1$	-1	$n + \alpha$
$T_n(x)$		$\dfrac{1}{\pi\sqrt{1 - x^2}}$	$\dfrac{2}{1 + \delta_{n,0}}$	1	x				
$U_n(x)$	$[-1, 1]$	$\pi\sqrt{1 - x^2}$	$\dfrac{2}{\pi^2}$	1	$2x$	1	0	2	1

Table 3.1 Integration limits, weight functions, normalisations and coefficients for the recurrence relation (3.53) for the generalized Laguerre polynomials (L_n^α) and the Chebyshev polynomials of first (T_n) and second kind (U_n). For a more complete list for different other types of orthogonal polynomials see Ref. [89].

Chebyshev Polynomials   The Chebyshev polynomials can be expressed in terms of trigonometric functions

$$T_n(\cos\theta) = \cos n\theta, \qquad U_n(\cos\theta) = \frac{\sin[(n+1)\theta]}{\sin\theta}. \tag{3.55}$$

For the T_n this yields the unique feature that on the interval $[-1, 1]$ all of the extrema have values that are either 1 or -1, thus

$$|T_n(x)| \leq 1 \ \forall \ x \in [-1, 1]. \tag{3.56}$$

Similarly, for the U_n one finds

$$|U_n(x)| \leq n + 1 \ \forall \ x \in [-1, 1]. \tag{3.57}$$

There are several interrelations between different sets of orthogonal polynomials [89], where we will later on use

$$T_n(x) = U_n(x) - xU_{n-1}(x), \tag{3.58}$$
$$T_{n+1}(x) = xU_n(x) - U_{n-1}(x), \tag{3.59}$$
$$\Rightarrow \quad U_n(x) = \frac{1}{1 - x^2}[T_n(x) - xT_{n+1}(x)]. \tag{3.60}$$

In order to apply the series expansion to operator functions (3.52), it is necessary to rescale the spectrum of the operator $\hat{O}$ to the interval $[-1, 1]$ via

$$\tilde{O} = (\hat{O} - b) \cdot a, \tag{3.61}$$

where

$$a = (2 - \varepsilon)/(\lambda_{\max} - \lambda_{\min}), \tag{3.62}$$
$$b = (\lambda_{\max} + \lambda_{\min})/2 \tag{3.63}$$

with the extremal eigenvalues $\lambda_{\min}$ and $\lambda_{\max}$ of the operator $\hat{O}$ as well as a small positive number ε of the order of the numerical precision. Then

$$\langle\Psi|f(\hat{O})|\Psi\rangle = \langle\Psi|f(\tilde{O}/a+b)|\Psi\rangle = \langle\Psi|\tilde{f}(\tilde{O})|\Psi\rangle, \qquad (3.64)$$

where $\tilde{f}(\tilde{x}) = \tilde{f}((x-b)\cdot a) = f(x)$. The α_n and μ_n now have to be obtained for the rescaled function $\tilde{f}$ and the rescaled operator $\tilde{O}$.

A very nice property of the expectation values $\mu_n = \langle\Psi|T_n(\tilde{O})|\Psi\rangle$ for Chebyshev polynomials of the first kind is

$$-1 \leq \mu_n \leq 1, \qquad (3.65)$$

as long as $|\Psi\rangle$ is normalised to $\langle\Psi|\Psi\rangle = 1$. This can be derived from the property (3.56), which leads to

$$\mu_n = \langle\Psi|T_n(\tilde{O})|\Psi\rangle = \sum_k T_n(\lambda_k)\langle\Psi|k\rangle\langle k|\Psi\rangle \overset{(3.56)}{\leq} \sum_k \langle\Psi|k\rangle\langle k|\Psi\rangle = 1, \qquad (3.66)$$

$$\mu_n = \langle\Psi|T_n(\tilde{O})|\Psi\rangle = \sum_k T_n(\lambda_k)\langle\Psi|k\rangle\langle k|\Psi\rangle \geq -\sum_k \langle\Psi|k\rangle\langle k|\Psi\rangle = -1, \qquad (3.67)$$

with eigenvalues λ_k and eigenvectors $|k\rangle$ of the operator $\tilde{O}$. Again, for the $\mu_n = \langle\Psi|U_n(\tilde{O})|\Psi\rangle$, we find

$$-n-1 \leq \mu_n \leq n+1. \qquad (3.68)$$

Laguerre Polynomials In order to apply the series expansion to operator functions (3.52), it is necessary to shift the spectrum of the operator $\hat{O}$ to the interval $[0,\infty]$ via

$$\tilde{O} = \hat{O} - \lambda_{\min}, \qquad (3.69)$$

with the smallest eigenvalue $\lambda_{\min}$ of the operator $\hat{O}$. Rescaling $\lambda_{\max} - \lambda_{\min}$ is not necessary in this case. Then

$$\langle\Psi|f(\hat{O})|\Psi\rangle = \langle\Psi|f(\tilde{O}+\lambda_{\min})|\Psi\rangle = \langle\Psi|\tilde{f}(\tilde{O})|\Psi\rangle, \qquad (3.70)$$

where $\tilde{f}(\tilde{x}) = \tilde{f}(x-\lambda_{\min}) = f(x)$. The α_n and μ_n now have to be obtained for the rescaled function $\tilde{f}$ and the rescaled operator $\tilde{O}$.

<div align="center">

***

</div>

In the remaining sections of this chaper we will discuss possible applications of the polynomial expansion. Due to the fact that our investigations of the method as well as the implementation are in an early stage at this point, only the results for spectral properties presented in chapter 4 are based on the methods described here, while the time evolution simulations for interacting nanostructures presented in chapter 5 are based on the Krylov subspace method. However, due to the versatility of the approach and with regard to future applications, we also include the discussion of the numerical computation of time evolution simulations and of thermodynamic properties, together with some simple examples.

3.4.2 The Exponential Function

Time evolution   To motivate the following discussion of the expansion of the exponential function in terms of Chebyshev polynomials, we mention three example applications.

1. For $|\Psi\rangle$ being the initial state of a system which is described by a Hamiltonian $\hat{H}$, the overlap of the time evolved state $|\Psi, t\rangle = \exp(-\mathrm{i}\hat{H}t/\hbar)|\Psi\rangle$ with the initial state is
$$\langle \Psi | \Psi, t \rangle = \langle \Psi | \mathrm{e}^{-\mathrm{i}\hat{H}t/\hbar} | \Psi \rangle. \tag{3.71}$$

2. The time-dependent Green's function of a system in its ground state $|\Psi_0\rangle$ (with energy E_0) can be obtained by computing the expectation value of
$$\langle \Psi_0 | \hat{A} \, \mathrm{e}^{-\mathrm{i}(\hat{H}-E_0)t/\hbar} \hat{B} | \Psi_0 \rangle \tag{3.72}$$

   and similar expressions. We want to note that the numerical data that has to be obtained for this computation can also be used to derive results for the Green's function in frequency space *without* the need for a numerical Fourier transformation of the results of Eq. (3.72). This will become clear in section 3.4.3.

3. The simulation of the time-dependent behaviour of observables $\hat{O}$, as for example current in a non-equilibrium state, amounts to the evaluation of expressions of the form
$$\langle \Psi | \mathrm{e}^{\mathrm{i}\hat{H}t/\hbar} \hat{O} \mathrm{e}^{-\mathrm{i}\hat{H}t/\hbar} | \Psi \rangle. \tag{3.73}$$

Chebyshev expansion   The expansion coefficients in (3.51) for the exponential function $f(x) = \mathrm{e}^{-\mathrm{i}xt}$ are given as [89, 108]

$$\alpha_n = \frac{2}{1 + \delta_{n,0}} \int\limits_{-1}^{1} \mathrm{d}x \, \frac{T_n(x)\mathrm{e}^{-\mathrm{i}xt}}{\pi\sqrt{1 - x^2}} = \frac{2 \cdot (-\mathrm{i})^n}{1 + \delta_{n,0}} J_n(t) \tag{3.74}$$

with the Bessel functions of first kind J_n and the Chebyshev polynomials of the first kind T_n. Here, the weight function reads $w(x) = 1/(\pi\sqrt{1 - x^2})$ and the normalisation $h_n = 2/(1 + \delta_{n,0})$. Assuming that the Bessel function can be calculated to arbitrary numerical precision, the numerical precision of the expectation values (3.71-3.73) is determined by the precision ε of the matrix elements μ_n (3.52). The asymptotic behaviour of the Bessel functions is

$$J_n(t) \approx \begin{cases} (t/2)^n/n! & \text{if } 0 < t \ll \sqrt{n+1}, \\ \sqrt{2/(\pi t)} \cos(t - \frac{n\pi}{2} - \frac{\pi}{4}) & \text{if } t \gg n^2. \end{cases} \tag{3.75}$$

Since for orders $n \ll \sqrt{t}$ for fixed t the values of J_n all are of the same order of magnitude up to a certain cutoff, cf. also Fig. 3.5, and $-1 < \mu_n < 1$, the absolute
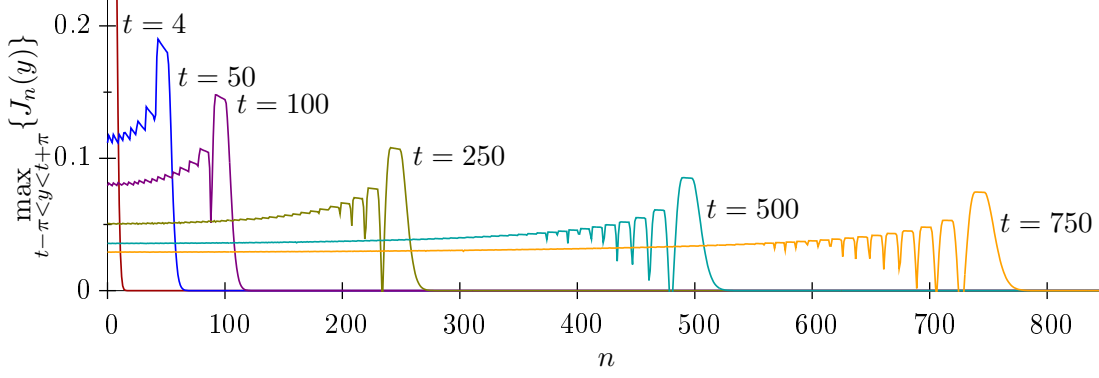
Figure 3.5 Order of magnitude of the Bessel functions $J_n(t)$ as function of the order n for different values of t.

numerical precision of the result is limited by $\varepsilon \cdot \max_{n \geq 0}(|\mu_n| \cdot J_n) \approx \varepsilon \cdot \max_{n \geq 0}(J_n) < \varepsilon$. For large n, the asymptotics for small t can be further simplified using the Stirling formula

$$J_n(t) \approx \frac{(t/2)^n}{\sqrt{2\pi n}} n^{-n} e^n = \left(\frac{e^1 \cdot t}{2n} \right)^n \frac{1}{\sqrt{2\pi n}}. \tag{3.76}$$

The $J_n(t)$ rapidly decay to 0 for fixed t. Fig. 3.5 shows the order of magnitude of J_n as a function of n for different values of t. This shows graphically that the Chebyshev series can be truncated already for orders on the scale of $n \gtrsim t$.

In order to demonstrate the effect of the truncation of the series (3.52) at a finite order $n = N$ we evaluate Eq. (3.71) for a simple case, where we assume $\hat{H}|\Psi\rangle = E|\Psi\rangle$, $E = \hbar\omega$. Then $\langle\Psi|\Psi(t)\rangle = e^{-i\omega t}$. According to table 3.1, the orthogonality relation (3.49) is fulfilled on the interval $[l, r] = [-1, 1]$ for Chebyshev polynomials. Therefore, in order to use the Hamiltonian $\hat{H}$ for the iterative construction of Chebyshev moments μ_n, cf. Eqns. (3.52) and (3.53), a rescaled version $\tilde{H}$ of $\hat{H}$ has to be computed according to Eqns. (3.61-3.63). The extremal eigenvalues $\lambda_{\min} = E_0$, $\lambda_{\max} = E_{\max}$ of $\hat{H}$ have to be computed by means of other techniques; cf. section 3.1. Then, with Eqns. (3.52), (3.64) and (3.74),

$$\langle\Psi|e^{-i\hat{H}t/\hbar}|\Psi\rangle = \langle\Psi|e^{-i(\tilde{H}/a+b)t/\hbar}|\Psi\rangle \tag{3.77}$$

$$= \langle\Psi|e^{-i\tilde{H}\tilde{t}}|\Psi\rangle e^{-ibt/\hbar} \approx e^{-ibt/\hbar} \sum_{n=0}^{N} \frac{2 \cdot (-i)^n}{1 + \delta_{n,0}} J_n(\tilde{t}) \mu_n[\tilde{H}], \tag{3.78}$$

where

$$\tilde{t} = t/(\hbar a). \tag{3.79}$$

For the given example we want to compute the series expansion for we still have to rescale $\tilde{\omega} = (\hbar\omega - b) \cdot a$. The Chebyshev moments then simply fulfill $\mu_n = T_n(\tilde{\omega})$. The real part of the series expansion is displayed in Fig. 3.6. Note, that for "real world" problems the rescaling of the time parameter represents a strong limitation to the approach. Assuming that the difference $E_{\max} - E_0$ scales approximately proportional
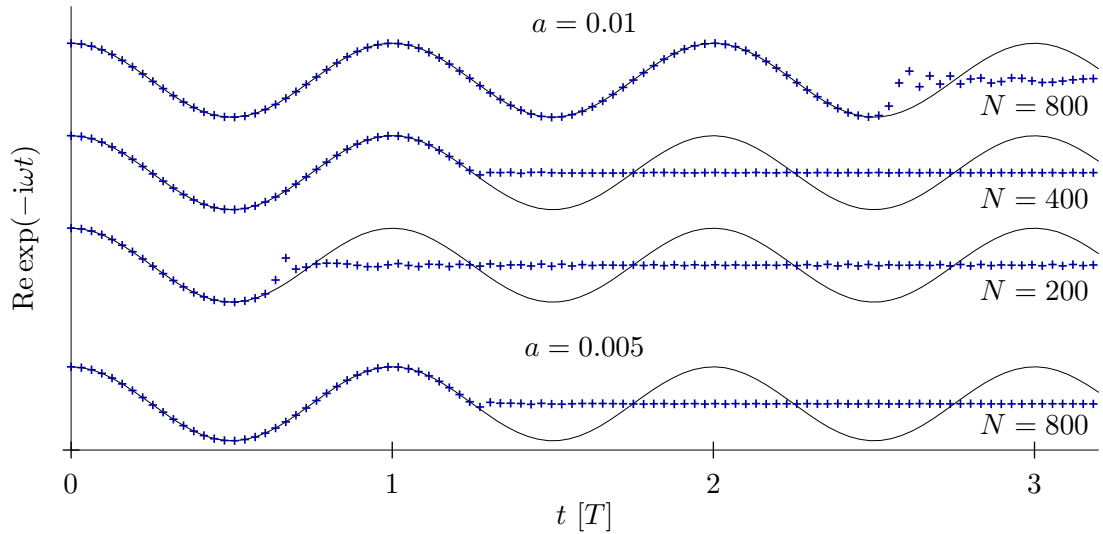
Figure 3.6   Real part of $\mathrm{e}^{-\mathrm{i}\omega t}$, computed using the truncated Chebyshev series expansion for different truncation orders N ($=800, 400, 200$) and for different rescaling factors a ($=0.01, 0.005$). $\omega = 2\pi/T = 2$, $b = 0$. Note, that for "real world" problems, the rescaling factor a and the shift b are determined by the spectrum of the given Hamiltonian. The maximum time is proportional to N and to a.

with the size L of the considered system, we find $\tilde{t} \propto L$ for a fixed t. Then, in order to enforce a certain truncation error, one has to scale the truncation order $N \propto L$.

Concerning the example application Eq. (3.73) for the time-dependent expectation value of an observable we finally have to add, that the expression can be computed by expanding the two time evolution operators *seperately*. This amounts to replacing Eq. 3.52 by

$$\langle\Psi|\mathrm{e}^{\mathrm{i}\hat{H}t/\hbar}\hat{O}\mathrm{e}^{-\mathrm{i}\hat{H}t/\hbar}|\Psi\rangle \approx \sum_{n,m}^{N} \alpha_n\alpha_m\mu_{nm}, \tag{3.80}$$

$$\mu_{nm} = \langle n|\hat{O}m\rangle, \qquad |n\rangle = T_n(\tilde{H})|\Psi\rangle, \qquad |\hat{O}m\rangle = \hat{O}|m\rangle. \tag{3.81}$$

While the numerical effort for computing the expectation value from a given set of Chebyshev moments μ_{nm} and expansion coefficients α_n scales quadratically with the truncation order N in this case, the main effort consists of the matrix-vector multiplications for computing the states $|n\rangle$. The need for the additional states $|\hat{O}m\rangle$ only doubles the number of matrix-vector multiplications.

Temperature evolution / imaginary time evolution   For the calculation of thermodynamic properties, it can be useful to obtain the expectation values

$$\langle\Psi|\mathrm{e}^{-\beta\hat{H}}|\Psi\rangle, \quad \text{and in general} \quad \langle\Psi|\hat{H}^k\mathrm{e}^{-\beta\hat{H}}|\Psi\rangle = (-1)^k\frac{\partial^k}{\partial\beta^k}\langle\Psi|\mathrm{e}^{-\beta\hat{H}}|\Psi\rangle, \tag{3.82}$$

with the temperature $\beta^{-1} = k_{\mathrm{B}}T$.

Chebyshev expansion   The previous considerations for the time evolution of a state $|\Psi\rangle$ suggest to simply replace the time t in (3.71) by the "imaginary" time $-\mathrm{i}\beta$ and, via analytic continuation to the complex plane, to obtain the Chebyshev coefficients α_n from (3.74) as

$$\alpha_n = \frac{2 \cdot (-\mathrm{i})^n}{1 + \delta_{n,0}} J_n(-\mathrm{i}\beta) = \frac{2 \cdot (-1)^n}{1 + \delta_{n,0}} I_n(\beta), \tag{3.83}$$

with the modified Bessel functions of first kind I_n. To obtain the derivatives w.r.t. the inverse temperature, the modified Bessel functions have to be replaced with their respective derivatives. The asymptotics [89] of the $I_n(\beta)$ for small arguments β as compared to the order n

$$I_n(\beta) \approx \frac{\mathrm{e}^{\sqrt{n^2+\beta^2}}}{\sqrt{2\pi n}} \frac{\beta^n}{(2n)^n} \tag{3.84}$$

suggests the validity of this approach, since the expansion coefficients get suppressed for $n \gg \beta$ rapidly. However, the asymptotics for the opposite case, $n \ll \beta$, where

$$I_n(\beta) \approx \frac{\mathrm{e}^{\beta}}{\sqrt{2\pi\beta}}, \tag{3.85}$$

shows that the approach does not work for numerical computations if β is chosen big in a certain sense; to be precise, if ε is the precision of the numerical computation of the Chebyshev moments μ_n, then the terms $\propto I_n(\beta)\mu_n$ of the sum (3.52) are afflicted with a numerical error of the order of δ, provided $\beta \gtrsim \ln(\delta/\varepsilon)$. Since in practical calculations an error of the order $\varepsilon \approx 10^{-5}$ has to be expected for the moments, $\delta \approx 0.1$ for $\beta \gtrsim 10$; given that the spectrum of the Hamiltonian $\hat{H}$ has to be rescaled according to (3.61), replacing $\beta \to \tilde{\beta} = \beta/a$, the available range for the inverse temperature is further reduced by a factor a.

The expansion to the Chebyshev polynomials of the second kind suffers from similar problems as can be shown using relation (3.60).

Laguerre expansion   Alternatively, the exponential function can be expressed in terms of an expansion in generalized Laguerre polynomials $L_n^{(\alpha)}(x)$ with $\alpha > -1$. The corresponding coefficients read

$$\alpha_n = \frac{\beta^n}{(1+\beta)^{n+1+\alpha}} = (1+1/\beta)^{-n}\alpha_0, \quad \alpha_0 = \frac{1}{(1+\beta)^{1+\alpha}}. \tag{3.86}$$

The expansion is convergent if (and only if) $\mathrm{Re}\beta > -1/2$. Again, the expectation value of $\hat{H}^k \exp(-\beta\hat{H})$ can be obtained by replacing the coefficients α_n with their corresponding derivatives w.r.t. β. For positive β, the coefficients decay exponentially with the order n. However, as can be deduced from the above formula, for growing β the decay slows down, which enforces an increase of the truncation order N of the polynomial approximation in order to keep the truncation error constant. This problem can be cured by rescaling the Hamiltonian. Since the upper limit of
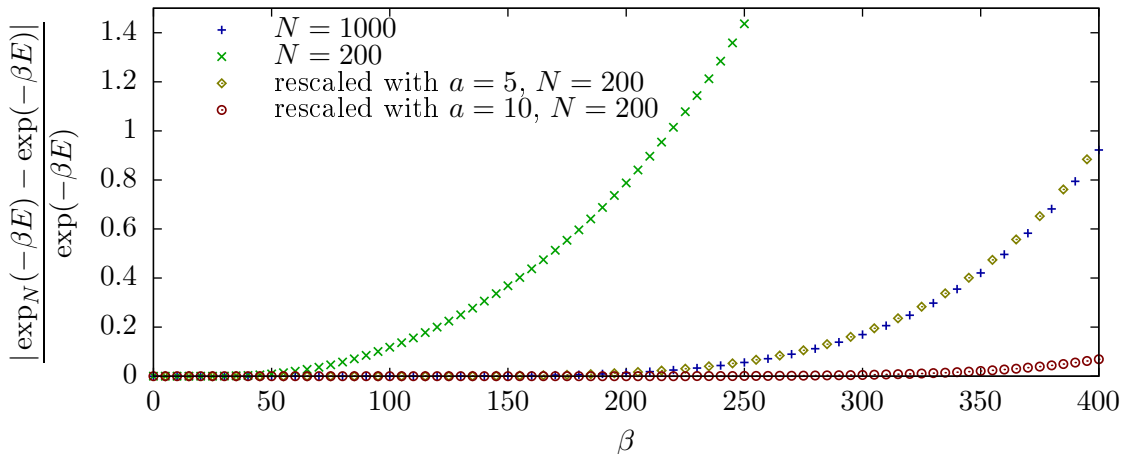
Figure 3.7 Relative truncation error of the Laguerre series expansion $\exp_N$ of the exponential function $\exp$ with truncation order N, as compared to the exact value, computed using the Laguerre series expansion ($\alpha = 0$ for $L_n^{(\alpha)}$) for different truncation orders ($N = 200, 1000$) and for different rescaling factors a ($= 1, 5, 10$). $E = 0.01$, corresponding to realistic values for the finite size energy gap of low lying excited states (in dimensionless units) in a system with ~ 100 lattice sites.

the integral in Eq. (3.49) is infinite in the case of Laguerre polynomials, we can introduce a rescaling $\hat{H} \rightarrow \tilde{H} = a \cdot \hat{H}$ with $a > 1$, resulting in a rescaling of the temperature $\beta \rightarrow \tilde{\beta} = \beta/a$.

To summarize this section, again we discuss a simple example where we assume $\hat{H}|\Psi\rangle = E|\Psi\rangle$. The computation of the Laguerre moments then amounts to $\mu_n = L_n^{(\alpha)}(E)$. To demonstrate the truncation error we plot the error of the truncated Laguerre expansion in Fig. 3.7 for different values of the truncation order N and for a rescaled energy scale. Since for the computation of the μ_n in general matrix vector multiplications are involved, it may be numerically cheaper to rescale the Hamiltonian by a factor $a > 1$ as compared to increasing the truncation order N.

3.4.3 Resolvent Expressions

The computation of Green's functions in the frequency representation is the last topic that will be discussed in the context of polynomial expansions. The evaluation of expressions of the form

$$\mathcal{G}^{\pm}_{\hat{A},\hat{B}}(z) = \langle\Psi|\hat{A}(E_0 - \hat{H} \pm z)^{-1}\hat{B}|\Psi\rangle, \qquad z = \hbar(\omega + \mathrm{i}\eta), \quad \omega \in \mathbb{R}, \quad \eta > 0 \quad (3.87)$$

can be traced back to the expansion of the function

$$f_z^{\pm}(x) = \frac{1}{\pm z - x} \quad \Rightarrow \quad \mathcal{G}^{\pm}_{\hat{A},\hat{B}}(z) = \langle\Psi|\hat{A}f_z^{\pm}(\hat{H} - E_0)\hat{B}|\Psi\rangle \qquad (3.88)$$

in terms of Chebyshev polynomials. Since the frequency-dependent Green's function (3.87) can be derived from the time-dependent counterpart (3.72) by means of

a Fourier transform, we now may benefit from the discussion of the Chebyshev expansion of the time-dependent exponential function in section 3.4.2. After rescaling the operator $\hat{H} - E_0 \to \tilde{H}$ to fit its spectrum into the interval $[-1, 1]$, the function $\tilde{f}_{\tilde{z}}^{\pm}(\tilde{x})$ can be rewritten as

$$\frac{1}{\pm\tilde{z} - \tilde{x}} = -\mathrm{i} \int\limits_0^{\pm\infty} \mathrm{d}t \; \mathrm{e}^{\mathrm{i}(\pm\tilde{z}-\tilde{x})t}, \tag{3.89}$$

which yields the coefficients for the expansion in terms of Chebyshev polynomials of the first kind (cf. Eq. (3.51) and table 3.1)

$$\alpha_n^{\pm}(\tilde{z}) = (T_n, \tilde{f}_{\tilde{z}}^{\pm})h_n = \frac{2/\pi}{1 + \delta_{n,0}} \int\limits_{-1}^{1} \mathrm{d}x \; \frac{T_n(x)}{\sqrt{1 - x^2}} \frac{1}{\pm\tilde{z} - x} \tag{3.90}$$

$$= \frac{-2\mathrm{i}/\pi}{1 + \delta_{n,0}} \int\limits_0^{\pm\infty} \mathrm{d}t \; \mathrm{e}^{\pm\mathrm{i}\tilde{z}t} \int\limits_{-1}^{1} \mathrm{d}x \; \frac{T_n(x)}{\sqrt{1 - x^2}} \mathrm{e}^{-\mathrm{i}\tilde{x}t} = \frac{2(-\mathrm{i})^{n+1}}{1 + \delta_{n,0}} \int\limits_0^{\pm\infty} \mathrm{d}t \; \mathrm{e}^{\pm\mathrm{i}\tilde{z}t} J_n(t) \tag{3.91}$$

$$= \frac{2/(1 + \delta_{n,0})}{(\pm\tilde{z})^{n+1}(1 + \sqrt{\tilde{z}^2}\sqrt{\tilde{z}^2 - 1}/\tilde{z}^2)^n \sqrt{1 - 1/\tilde{z}^2}}, \tag{3.92}$$

where we explicitly want to emphasize the relation to the Bessel functions of the first kind $J_n(t)$ in Eq. (3.91). Taking the correct rescaling into account, the Greens's function then is recovered as

$$\mathcal{G}_{\hat{A},\hat{B}}^{\pm}(\omega) = a \sum_{n=0}^{\infty} \alpha_n^{\pm}\big(a(\hbar(\omega + \mathrm{i}\eta) \mp b)\big)\mu_n, \tag{3.93}$$

where the Chebyshev moments μ_n are given as[15]

$$\mu_n = \langle\Psi|\hat{A}T_n(a(\hat{H} - E_0 - b))\hat{B}|\Psi\rangle. \tag{3.94}$$

It is now important to determine a suitable value for the truncation order N in order to obtain reliable numbers. From Eq. (3.65) we know that $-\mathcal{N}^2 \le \mu_n \le \mathcal{N}^2$, where $\mathcal{N}^2 = \langle\Psi|\hat{A}\hat{B}|\Psi\rangle$. Therefore it is again sufficient to study the behaviour of the coefficients $\alpha_n^{\pm}(z)$ for values of z in the desired range. A very simple estimate can be given by looking at the derivation of the $\alpha_n^{\pm}$, and especially by considering the properties of the Bessel function in Eq. (3.91): For $n > |t|$, $J_n(t)$ drops rapidly to zero, as already discussed before, relating the maximum time $|t|$ to N, so that $N \gtrsim |t|$. The maximum time, on the other hand, is determined by $\mathrm{Im}\tilde{z}$, the latter exponentially cutting of the infinite integration range of the time integration in

---

[15]Note, that for the computation of the time-dependent and of the frequency-dependent Green's function the *same* momenta μ_n have to be computed, while the expansion coefficients α_n are different, cf. example 2 in section 3.4.2.

Eq. (3.91). Therefore, we get an estimate $t \approx 1/\mathrm{Im}\tilde{z}$, which finally leads us to the expression

$$N \gtrsim \frac{1}{a\hbar\eta}. \tag{3.95}$$

This estimate also shows the limitation of the approach. Since a is proportional to the inverse difference of the extremal eigenvalues of the Hamiltonian of the system, $1/a$ grows with the system size (provided a corresponding scaling of the spectrum of $\hat{H}$), and hence the number of moments μ_n that has to be computed.[16] On the other hand, resolving narrow structures in the spectrum requires η to be chosen small as compared to the width of the spectral structure of interest.

---

[16]If investigating bosonic degrees of freedom as for example in a 1D waveguide, this limitation is not so important if the number of photons (and hence the relevant energy spectrum) is kept independent of the size of the system.

Chapter 4

Green's functions in the Resolvent Representation

Despite its simplicity, the interacting resonant level model (2.15) shows some interesting, if not surprising, features. For finite bias transport, a regime of negative differential conductance (NDC) has been found for finite electron-electron interaction U_C on the contact link [56]. Furthermore, the system shows non-monotonic behaviour when increasing U_C [31, 109]. The linear conductance as a function of the gate voltage V_g has Lorentzian shape, the width of which grows up to a certain value of $U_C = 2J$. By further increasing the interaction the width of the Lorentzian shrinks again [31]. In the present chapter we now pose the question how these effects are reflected in the spectral function of the interacting level. We will recover the Lorentzian shape for the spectrum, the width of which grows with increasing interaction U_C. However, in contrast to the linear conductance, the width does not decrease again for values of $U_C > 2J$. Instead, there are peaks showing up for energies *outside* the conduction band.

As a precondition to obtain the spectral function, we need to compute the single particle Green's function of the resonant level in frequency space. We therefore make use of the Chebyshev expansion of the function $(\pm z - x)^{-1}$ as discussed in section 3.4.3. The limitation of the numerical implementation of the treatment of systems with finite size, cf. section 2.3, leads to a finite energy level discretisation. In order to cure this shortcoming we first introduce a finite level broadening to average over a few discrete energy levels. Then we apply a quadratic extrapolation of the *self-energy* to zero broadening to obtain the Green's function for the thermodynamic limit.
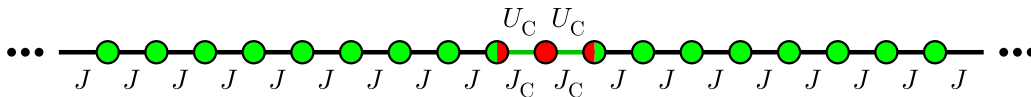

Figure 4.1   Sketch of the IRLM. The interacting level is coupled to two non-interacting leads.

4.1 Green's functions in time- and frequency representation

The time-dependent lesser (greater) Green's functions $G^<$ ($G^>$) and the retarded (advanced) Green's functions G^{r} (G^{a}) are defined [110] by[1]

$$G^>_{\hat{A},\hat{B}}(t,t') = -\mathrm{i}\langle\hat{A}(t)\hat{B}(t')\rangle, \quad G^<_{\hat{A},\hat{B}}(t,t') = -\mathrm{i}\zeta\hat{B}(t')\hat{A}(t), \tag{4.1}$$

$$G^{\mathrm{r}}_{\hat{A},\hat{B}}(t,t') = -\mathrm{i}\Theta(t-t')\langle[\hat{A}(t),\hat{B}(t')]_{-\zeta}\rangle \tag{4.2}$$

$$= \Theta(t-t')[G^>_{\hat{A},\hat{B}}(t,t') - G^<_{\hat{A},\hat{B}}(t,t')], \tag{4.3}$$

$$G^{\mathrm{a}}_{\hat{A},\hat{B}}(t,t') = \mathrm{i}\Theta(t'-t)\langle[\hat{A}(t),\hat{B}(t')]_{-\zeta}\rangle \tag{4.4}$$

$$= \Theta(t'-t)[G^<_{\hat{A},\hat{B}}(t,t') - G^>_{\hat{A},\hat{B}}(t,t')], \tag{4.5}$$

with arbitrary time-dependent operators $\hat{A}(t)$ and $\hat{B}(t)$.[2] The square brackets $[\hat{A},\hat{B}]_{-\zeta} = \hat{A}\hat{B} - \zeta\hat{B}\hat{A}$ denote the common fermionic ($\zeta = -1$) and bosonic ($\zeta = 1$) commutator. The expectation value is defined for an arbitrary pure quantum-mechanical state $|\Psi\rangle$

$$\langle\ldots\rangle = \langle\Psi|\ldots|\Psi\rangle. \tag{4.6}$$

In order to simplify the notation we furthermore introduce the Green's functions

$$G^+_{\hat{A},\hat{B}}(t,t') = -\mathrm{i}\Theta(t-t')\langle\hat{A}(t)\hat{B}(t')\rangle, \quad G^-_{\hat{A},\hat{B}}(t,t') = \mathrm{i}\Theta(t-t')\langle\hat{A}(t')\hat{B}(t)\rangle. \tag{4.7}$$

This allows rewriting

$$G^>_{\hat{A},\hat{B}}(t,t') = G^+_{\hat{A},\hat{B}}(t,t') - G^-_{\hat{A},\hat{B}}(t',t), \tag{4.8}$$

$$G^<_{\hat{A},\hat{B}}(t,t') = \zeta[G^+_{\hat{B},\hat{A}}(t',t) - G^-_{\hat{B},\hat{A}}(t,t')], \tag{4.9}$$

$$G^{\mathrm{r}}_{\hat{A},\hat{B}}(t,t') = G^+_{\hat{A},\hat{B}}(t,t') + \zeta G^-_{\hat{B},\hat{A}}(t,t'), \tag{4.10}$$

$$G^{\mathrm{a}}_{\hat{A},\hat{B}}(t,t') = \zeta G^+_{\hat{B},\hat{A}}(t',t) + G^-_{\hat{A},\hat{B}}(t',t). \tag{4.11}$$

Since throughout this work we are interested in properties of *steady* states,[3] we assume translational invariance with respect to time. Hence, the Green's functions only depend on $t - t'$, which allows the shift $t' \to 0$.

The frequency-dependent Green's functions $\mathcal{G}(\omega)$ are defined by means of the Fourier transform of their time-dependent counterpart. For the following discussion of the impurity Green's function of the IRLM, we now assume that the state $|\Psi\rangle$

---

[1]We largely follow the notation used in [87].

[2]Throughout this work, we always assume the Hamiltonian $\hat{H}$, that is driving the time-evolution of the system, to be *independent of time*. Then, for any operator $\hat{O}$, the time evolution is given by $\hat{O}(t) = \mathrm{e}^{\mathrm{i}\hat{H}t/\hbar}\hat{O}\mathrm{e}^{-\mathrm{i}\hat{H}t/\hbar}$.

[3]In this chapter, we assume $|\Psi\rangle$ to be the ground-state of the system, while in chapter 5 we assume $|\Psi\rangle$ to be a non-equilibrium steady state where the expectation value of time-dependent operators $\hat{O}(t)$ is *independent* of t, $\langle\Psi|\hat{O}(t)|\Psi\rangle = \mathrm{const}$.

is equivalent to the ground state of the system, with $\hat{H}|\Psi\rangle = E_0|\Psi\rangle$, E_0 the corresponding energy. Due to the definition of $G^\pm$, the $\mathcal{G}(\omega)$ then can be represented in terms of

$$\mathcal{G}^+_{\hat{A},\hat{B}}(\omega + \mathrm{i}\eta) = \frac{1}{\hbar}\int\limits_{-\infty}^{\infty} \mathrm{d}t \ \mathrm{e}^{\mathrm{i}(\omega+\mathrm{i}\eta)t}G^+_{\hat{A},\hat{B}}(t,0) = -\frac{\mathrm{i}}{\hbar}\int\limits_{0}^{\infty} \mathrm{d}t \ \mathrm{e}^{\mathrm{i}(\omega+\mathrm{i}\eta)t}\langle\hat{A}(t)\hat{B}(0)\rangle \quad (4.12)$$

$$= -\frac{\mathrm{i}}{\hbar}\int\limits_{0}^{\infty} \mathrm{d}t \ \langle\Psi|\hat{A}\mathrm{e}^{\mathrm{i}[(E_0-\hat{H})/\hbar+\omega+\mathrm{i}\eta]t}\hat{B}|\Psi\rangle = \langle\Psi|\hat{A}\frac{1}{E_0 - \hat{H} + \hbar(\omega + \mathrm{i}\eta)}\hat{B}|\Psi\rangle,$$
$$(4.13)$$

$$\mathcal{G}^-_{\hat{A},\hat{B}}(\omega + \mathrm{i}\eta) = \frac{1}{\hbar}\int\limits_{-\infty}^{\infty} \mathrm{d}t \ \mathrm{e}^{\mathrm{i}(\omega+\mathrm{i}\eta)t}G^-_{\hat{A},\hat{B}}(t,0) = \langle\Psi|\hat{A}\frac{1}{E_0 - \hat{H} - \hbar(\omega + \mathrm{i}\eta)}\hat{B}|\Psi\rangle,$$
$$(4.14)$$

with a convergence generating factor $\eta = 0^+$. For the numerical computation of $\mathcal{G}^\pm$, we later will choose η to be *finite* in order to average over some discrete energy levels of the *finite* system. Based on the decomposition in $+$ and $-$ part, the retarted and the advanced Greens's function in frequency representation read

$$\mathcal{G}^{\mathrm{r}}_{\hat{A},\hat{B}}(\omega) = \mathcal{G}^+_{\hat{A},\hat{B}}(\omega) + \zeta\mathcal{G}^-_{\hat{B},\hat{A}}(\omega), \quad\quad\quad\quad (4.15)$$

$$\mathcal{G}^{\mathrm{a}}_{\hat{A},\hat{B}}(\omega) = \zeta\mathcal{G}^+_{\hat{B},\hat{A}}(\omega) + \mathcal{G}^-_{\hat{A},\hat{B}}(\omega). \quad\quad\quad\quad (4.16)$$

Numerical computation   For the numerical computation we use the method discussed in section 3.4.3, which is based on the expansion of the function $f^\pm_z(x) = (\pm z - x)^{-1}$ in terms of Chebyshev polynomials, allowing to express the Green's functions as $\mathcal{G}^\pm_{\hat{A},\hat{B}}(\omega) = \langle\Psi|f^\pm_{\hbar(\omega+\mathrm{i}\eta)}(\hat{H} - E_0)|\Psi\rangle$. With the expansion coefficients of $f^\pm_z$

$$\alpha^\pm_n(z) = \frac{2/(1 + \delta_{n,0})}{(\pm z)^{n+1}(1 + \sqrt{z^2}\sqrt{z^2 - 1}/z^2)^n\sqrt{1 - 1/z^2}}, \quad\quad (4.17)$$

it is then possible to rewrite the Green's function as

$$\mathcal{G}^\pm_{\hat{A},\hat{B}}(\omega + \mathrm{i}\eta) = a\sum\limits_{n=0}^{\infty} \alpha^\pm_n(a(\hbar(\omega + \mathrm{i}\eta) \pm b))\mu_n, \quad\quad (4.18)$$

where $\mu_n = \langle\Psi|\hat{A}T_n(a(\hat{H} - E_0 - b))\hat{B}|\Psi\rangle$ with the Chebyshev polynomials of the first kind T_n. The Chebyshev moments μ_n can be constructed iteratively using the relation $T_{n+1}(x) = 2xT_n(x) - T_{n-1}(x)$. The rescaling a and the shift b of the spectrum of the Hamiltonian $\hat{H}$ into the interval $(-1, 1)$ has to be performed in order to meet the orthogonality relations for the Chebyshev polynomials. For a discussion in more details see section 3.4.

4.2 Single-particle spectrum

We define the spectral operator $\hat{\mathcal{A}}$ for a system described by a Hamiltonian $\hat{H}$ as

$$\hat{\mathcal{A}}(\varepsilon) = \delta\big(\varepsilon - (\hat{H} - E_0)\big). \tag{4.19}$$

For a given state $|\varphi\rangle$ it measures the contribution of eigenstates with energy ε to $|\varphi\rangle$. Here, E_0 is the energy of the ground state $|\Psi\rangle$ of the system. The single-particle spectral function then has to be computed for states $|\varphi^+\rangle = \hat{c}^\dagger|\Psi\rangle$ and $|\varphi^-\rangle = \hat{c}|\Psi\rangle$, and is given by

$$\mathcal{A}(\varepsilon) = \langle\Psi|\hat{c}^\dagger\hat{\mathcal{A}}(\varepsilon)\,\hat{c}|\Psi\rangle + \zeta\langle\Psi|\hat{c}\,\hat{\mathcal{A}}(\varepsilon)\,\hat{c}^\dagger|\Psi\rangle. \tag{4.20}$$

If we represent the δ-distribution by a Lorentzian in the limit of vanishing width η,

$$\delta(\varepsilon - x) = \frac{1}{\pi}\lim_{\eta\to0^+}\frac{\eta}{(\varepsilon - x)^2 + \eta^2} = \mp\frac{1}{\pi}\lim_{\eta\to0^+}\mathrm{Im}\frac{1}{\varepsilon - x \pm \mathrm{i}\eta}, \tag{4.21}$$

we understand that the single-particle spectral function is related to the retarded Green's function[4] $\mathcal{G}^{\mathrm{r}}_{\hat{c}\hat{c}^\dagger}$ by

$$\mathcal{A}(\varepsilon = \hbar\omega) = -\frac{1}{\pi}\lim_{\eta\to0^+}\mathrm{Im}\,\mathcal{G}^{\mathrm{r}}_{\hat{c}\hat{c}^\dagger}(\omega + \mathrm{i}\eta). \tag{4.22}$$

4.2.1 Numerical computation

Given that $|\Psi\rangle$ is the ground state of the system, $\mathcal{A}(\varepsilon)$ quantifies the excitation of an eigenstate with energy ε when a particle $\hat{c}^\dagger$ or hole $\hat{c}$ is added to the system. For a system with continuous spectrum, $\mathcal{A}(\varepsilon)$ will be a continuous function of the energy, while for a system with a discrete spectrum, $\mathcal{A}$ will show sharp δ-peaks for the discrete eigen-energies of the system. Now, the models we want to consider describe a nanostructure coupled to *infinite* leads, the latter providing for a continuous single-particle spectrum. In contrast, the models we implement the numerical simulation for are *finite*, with an overall number of M lattice sites, leading to a discretisation of the energy spectrum. In order to obtain an approximation to the thermodynamic limit, we therefore choose the convergence generating factor η to be finite, which leads to averaging over a few discrete energy levels. In the real-time representation, an excitation that is generated on the structure at an initial time will decay to the leads, generating a wave packet that runs towards the boundaries of the system. A finite value of η then causes the contributions to the integrals in Eqns. (4.12-4.14) to be damped exponentially for $t \to \infty$ with $\exp(-\eta t)$. A wave packet that gets reflected at the boundaries of the finite system will therefore be damped away before returning to the structure, if η is chosen sufficiently big. For a system with an overall number of $M = M_{\mathrm{L}} + M_{\mathrm{S}} + M_{\mathrm{R}}$ lattice sites, and with leads of (close to) equal size $M_{\mathrm{L}} \approx M_{\mathrm{R}}$, an estimate for the minimum value for η therefore is given by

$$\eta \gtrsim \frac{v_{\mathrm{F}}}{M}, \tag{4.23}$$

---

[4]A similar relation holds for the advanced Green's function.

with the Fermi velocity v_F in the leads. By means of the interpretation of the convergence generating factor η as a damping factor that removes effects resulting from reflections at the boundaries of the system we understand that this way we indeed can obtain results for the spectral function in the thermodynamic limit from a finite system. However, the broadening of the discrete energy levels also leads to a broadening of the spectral function $\mathcal{A}$ as a whole, which to overcome is desirable.

Poor man's deconvolution 2.0 In [87], a method to remove the broadening of the Green's function caused by a finite value of the convergence generating factor η was introduced. Based on the assumption that the self-energy $\Sigma(\omega)$, defined by

$$\mathcal{G}^\mathrm{r}(\omega) = \frac{1}{\hbar\omega - \Sigma(\omega) + \mathrm{i}\cdot 0^+}, \tag{4.24}$$

is shifted by $\mathrm{i}\eta$ for the situation with fininte broadening η, $\Sigma_\eta(\omega) = \hbar\omega + \mathrm{i}0^+ - [\mathcal{G}^\mathrm{r}(\omega+\mathrm{i}\eta)]^{-1} \overset{!}{=} \Sigma(\omega) - \mathrm{i}\hbar\eta$, a sharpened Green's function can be computed directly. This was succesfully checked for the energy eigenstates of a tight binding chain of free fermions, where the relation holds exactly.

In general, the broadened self-energy will depend on η in a more complicated way, which can spoil the approach. For example, for the impurity Green's function of the resonant level model with tight binding leads, the self-energy depends non-linearly on the broadening η – including the real part of Σ_η. Therefore we generalize the assumption where we now take the self-energy as a function of the broadening,

$$\Sigma_\eta(\omega) = \Sigma^{(0)}(\omega) + \Sigma^{(1)}(\omega)\eta + \Sigma^{(2)}(\omega)\eta^2 + \dots, \tag{4.25}$$

allowing for an extrapolation to $\eta = 0$ from numerical data with finite broadening. The self energy for the thermodynamic limit then can be identified as $\Sigma(\omega) \equiv \Sigma^{(0)}(\omega)$, which, in turn, yields the value for the Green's function in the thermodynamic limit

$$\mathcal{G}^\mathrm{r}(\omega) = \frac{1}{\hbar\omega - \Sigma^{(0)}(\omega) + \mathrm{i}\cdot 0^+}. \tag{4.26}$$

4.2.2 Impurity Green's function for the interacting resonant level model

The IRLM with tight binding leads is defined according to the Hamiltonian in Eq. (2.15). Since the numerical computation is performed on a compuer we are restricted to a finite version of the model as given in Eq. (2.21). The Hamiltonian of the system then reads

$$
\begin{aligned}
\hat{H} \equiv \hat{H}_\mathrm{IRLM}^\mathrm{finite} = &- J \sum_{x=0}^{M_\mathrm{L}-2} (\hat{c}_x^\dagger \hat{c}_{x+1} + \hat{c}_{x+1}^\dagger \hat{c}_x) - J \sum_{x=M_\mathrm{L}+1}^{M-2} (\hat{c}_x^\dagger \hat{c}_{x+1} + \hat{c}_{x+1}^\dagger \hat{c}_x) + V_\mathrm{g}\hat{n}_{M_\mathrm{L}} \\
&- J_\mathrm{C}(\hat{c}_{M_\mathrm{L}-1}^\dagger \hat{c}_{M_\mathrm{L}} + \hat{c}_{M_\mathrm{L}}^\dagger \hat{c}_{M_\mathrm{L}-1} + \hat{c}_{M_\mathrm{L}}^\dagger \hat{c}_{M_\mathrm{L}+1} + \hat{c}_{M_\mathrm{L}+1}^\dagger \hat{c}_{M_\mathrm{L}}) \\
&+ U_\mathrm{C}\Big[(\hat{n}_{M_\mathrm{L}-1} - \tfrac{1}{2})(\hat{n}_{M_\mathrm{L}} - \tfrac{1}{2}) + (\hat{n}_{M_\mathrm{L}} - \tfrac{1}{2})(\hat{n}_{M_\mathrm{L}+1} - \tfrac{1}{2})\Big]. \tag{4.27}
\end{aligned}
$$

The number of lattice sites in the left lead is given by M_{L}, the overall system size is $M = M_{\mathrm{L}} + M_{\mathrm{R}} + 1$, where we assume the structure to be situated in the middle of the system ($M_{\mathrm{L}} \approx M_{\mathrm{R}}$). A sketch of the model can be found in Fig. 4.1. The coupling of the structure to the leads is given by J_{C}, while the density-density interaction of the structure with the first lead site reads U_{C}. For the discussion of the spectrum we assume the level of the structure to be on resonance with the Fermi level and therefore set $V_{\mathrm{g}} \equiv 0$ in this chapter. Furthermore, we set the ratio of particle number N and number of lattice sites M (the filling factor) to $1/2$, corresponding to metallic leads.

The initial state $|\Psi\rangle$ is obtained by means of a ground state DMRG. This means that for each DMRG step, cf. section 3.2, the ground state is obtained in the truncated Hilbert space via a Davidson algorithm. Since we want to obtain the impurity Green's function, we furthermore compute $|\Phi_0\rangle = \hat{c}^\dagger_{M_{\mathrm{L}}} |\Psi\rangle$. To be able to calculate the Chebyshev moments μ_n we add $|\Phi_n\rangle = T_n(\tilde{H})|\Phi_0\rangle$, with the rescaled Hamiltonian $\tilde{H} = a(\hat{H} - E_0 - b)$.[5] Then $\mu_n = \langle \Phi_0 | \Phi_n \rangle$. For the numerical calculation, we set an upper bound to the dimension of the Hilbert space of the DMRG blocks, with $N_{\mathrm{cut}} \leq 7000$ at the maximum. Additionally we applied an upper bound to the discarded entropy $\mathcal{S}_{\mathrm{disc}} < 10^{-5}$, which allows the software to choose N_{cut} dynamically within the given bounds. The consumption of computer memory is largely determined by the dimension of the truncated Hilbert space, which strongly depends on the simulated system due to this dynamic approach. For the systems with the most unfavorable behaviour,[6] we needed to use computers with up to 48GB of RAM.

In Fig. 4.2 we now demonstrate the approach. For the noninteracting RLM with $U_{\mathrm{C}} = 0$, at half filling, the retarded Green's function with finite η was computed based on the evaluation of $\mathcal{G}^+$ and $\mathcal{G}^-$.[7] The data has been obtained based on the Chebyshev expansion of the resolvent up to order $N = 4000$; cf. also section 3.4. The two panels (a, b) show the imaginary and the real part of the self-energy as defined in Eq. (4.24), for different values of the convergence generating factor η, as well as $\Sigma^{(0)}$ as defined in Eq. (4.25), resulting from a quadratic fit to Σ_η. In order to visualize the discretisation of the single particle energy levels due to the finite size of the system, we include values for $\eta = 0.03$ on panel (a). However, for the fit procedure only those values of η are included that do not exhibit the finite size discretisation. The inset shows $-(\Sigma_\eta + i\eta)$ for two different values of ω, where the colours of the lines are associated with the respective imaginary or real part of Σ_η, cf. also the arrows on panels (a, b) of the figure. It can clearly be seen, that both, the real and the imaginary part of the broadened self-energy, depend non-linearly

---

[5]For the computation of the rescaling factor a and the shift b, a ground state DMRG calculation has to be carried out seperately in order to determine the ground state energy E_0 and the Energy $E_{\max}$ of the maximally excited state. Then $a \lesssim 2/(E_{\max} + E_0)$, $ab \lesssim 1$, where it has to be guaranteed that the spectrum of $\tilde{H}$ is on the interval $(-1, 1)$.

[6]For this work, we simulated systems according to Eq. (4.27), with $M = 48$, 96 and 168 lattice sites in total and with interaction $U_{\mathrm{C}} = 0.0 \ldots 4.0J$. For the bigger systems, and for stronger interaction U_{C}, the required size of the Hilbert space grows.

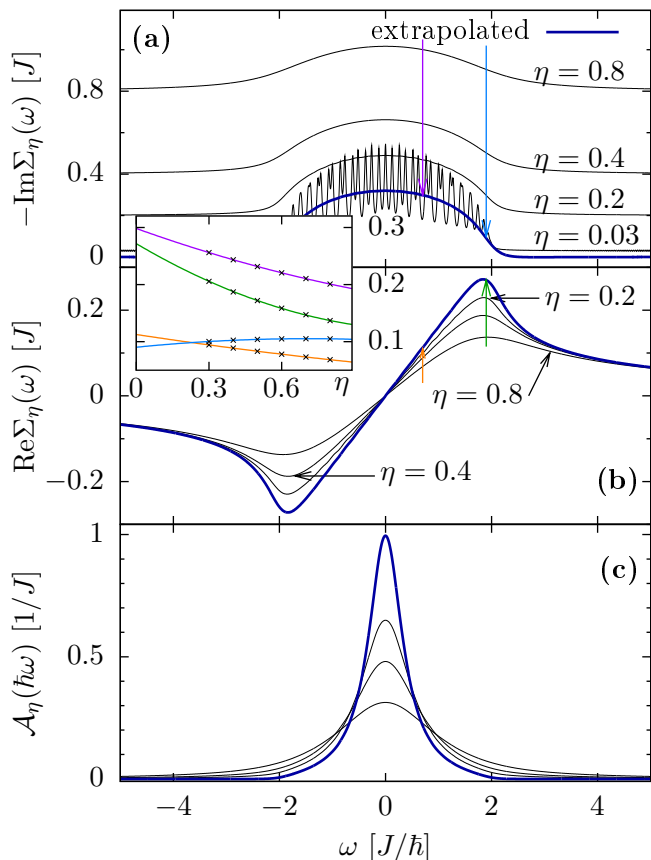[7]In fact, due to symmetry reasons, we can ommit the computation of $\mathcal{G}^-$.

Figure 4.2
(a) Imaginary and (b) real part of the broadening-dependent self-energy for different values of the convergence generating factor η. The thick lines represent $\Sigma^{(0)}$ as defined in Eq. (4.25), for a fit up to quadratic order. The system consist of $M = 48$ lattice sites in total, the impurity is coupled to the leads via $J_C = 0.4J$. For $\mathrm{Im}\Sigma$ we include values for $\eta = 0.03$ in order to demonstrate the effect of the discretisation of the lead levels. The inset shows $\mathrm{Re}\Sigma_\eta$ and $-(\mathrm{Im}\Sigma_\eta + \eta)$ as function of η for selected values of ω, compare the vertical arrows in the main plot. On panel (c) we show the η-broadened spectral function $\mathcal{A}_\eta(\hbar\omega)$, including the final $\mathcal{A}(\hbar\omega)$ after extrapolation $\eta \to 0$.

on η. The lines are quadratic fits to the data points, while the self-energy for $\eta \to 0$ is extracted from Eq. (4.25) as $\Sigma^{(0)}$. On panel (c), we show the η-broadened spectral function $\mathcal{A}_\eta$ for the corresponding values of η, as well as the final result $\mathcal{A}(\hbar\omega)$, obtained from Eq. (4.24) using $\Sigma^{(0)}(\omega)$ for the self-energy. In appendix B we provide an analytic expression for the spectral function, cf. Eq. (B.13), which allows us to check the numerical result for the noninteracting RLM. However we do not include it into the plot since it can not be discriminated from the numerical result by the eye.

We now turn to the behaviour of the spectral function, depending on the interaction U_C. Using the method described above we compute $\mathcal{A}(\varepsilon)$ in the thermodynamic limit for values in the range of $U_C = 0\ldots 4.0J$. In Fig. 4.3 we show results for two different couplings $J_C = 0.2J$ and $J_C = 0.15J$.[8] Increasing U_C has two effects: first, the central peak of the spectral function gets broadened. For values of $U_C \lesssim 2J$, the peak survives while for $U_C = 4.0J$, it seems to disappear completely. Reducing the coupling $J_C = 0.2J \to 0.15J$ leads to an increased height and a reduced width of the central peak, which leads us to the assumption that in the limit of very small

---

[8]The results have been obtained based on $N = 500$ ($N = 800$) Chebyshev moments for the system with $J_C = 0.2J$ and $M = 96$ ($J_C = 0.15J$ and $M = 168$) lattice sites.
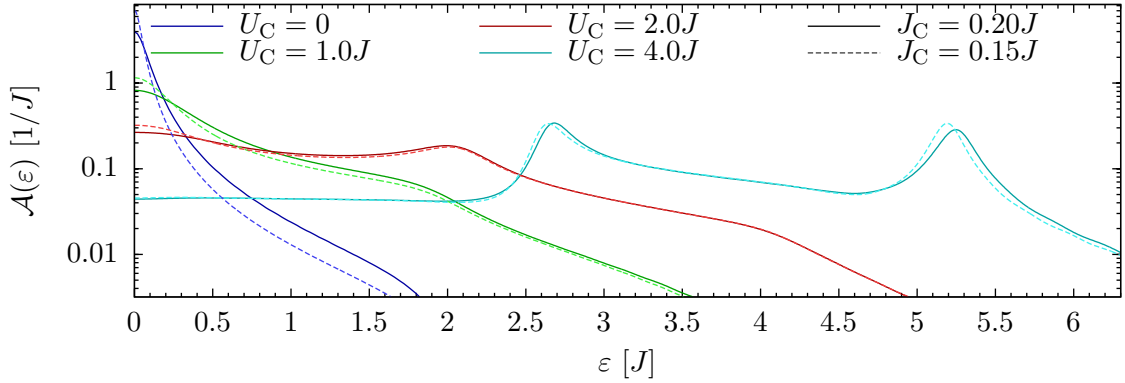
Figure 4.3 Spectral function $\mathcal{A}$ for the IRLM, on resonance ($V_g = 0$), for different values of the interaction $U_C = 0 \ldots 4.0J$. The system consists of $M = 96$ ($M = 168$) lattice sites in total, the impurity is coupled to the leads via $J_C = 0.2J$ ($J_C = 0.15J$). Increasing U_C leads to broadening of $\mathcal{A}$, while for $U_C \gtrsim 2.0J$, additional peaks appear, located *outside* the band.

J_C, the central peak could survive for values of $U_C > 4J$. The position of the side peaks seems not to be influenced by J_C, which leads us to the conclusion that their emergence is due to the finite band width $4J$.

The broadening of the central peak is represented in Fig. 4.4. On the left panel, we show the central peak of the spectral function $\mathcal{A}$, normalised to the maximum value $\mathcal{A}(\varepsilon = 0)$, for values of the interaction $U_C = 0 \ldots 3J$.[9] The red curves correspond to a Lorentzian,

$$\mathcal{A}_0(\varepsilon) = \frac{1}{\pi} \frac{\Gamma}{\Gamma^2 + \varepsilon^2}. \tag{4.28}$$

For the noninteracting RLM, $U_C = 0$, this expression corresponds to the wide-band limit of the spectral function $\mathcal{A}$, which can be obtained from Eq. (B.13) for $J_C \ll J$. In this case, the width $\Gamma \equiv \Gamma_0 = 2J_C^2/J$ is determined by the coupling J_C. We now fit this expression to the central peak of the numerical data for $\mathcal{A}(\varepsilon)$ in order to obtain its width Γ. In the non-interacting case a, we find good agreement of the numerical data and the wide-band limit $\mathcal{A}_0$, indicating that for the precise value of the coupling ($J_C = 0.15J$), band curvature effects do not play a major role, at least for vanishing interaction. The same still holds true for finite, increasing interaction, as long as $U_C \ll 1J$. For values of $U_C \gtrsim 1J$, we find strong deviations from the Lorentzian shape; cf. also Fig. 4.3. Nevertheless, the width Γ is still well defined for a small region at the Fermi level. However, for values of the interaction $U_C > 3J$, as discussed before, the central peak vanishes completly, rendering the width illdefined.

The behaviour of the width Γ depending on the interaction U_C, normalised to the width $\Gamma_0 = 2J_C^2/J$ of the noninteracting RLM, is represented on the right panel. We clearly find monotonous growth of Γ until the point where the central peak

---

[9] To be precise, in this case ($M = 168$ lattice sites, $J_C = 0.15J$), we did not compute $\mathcal{A}$ for the noninteracting case a $U_C = 0$. Instead, the curve a was computed based on the analytic expression (B.13).
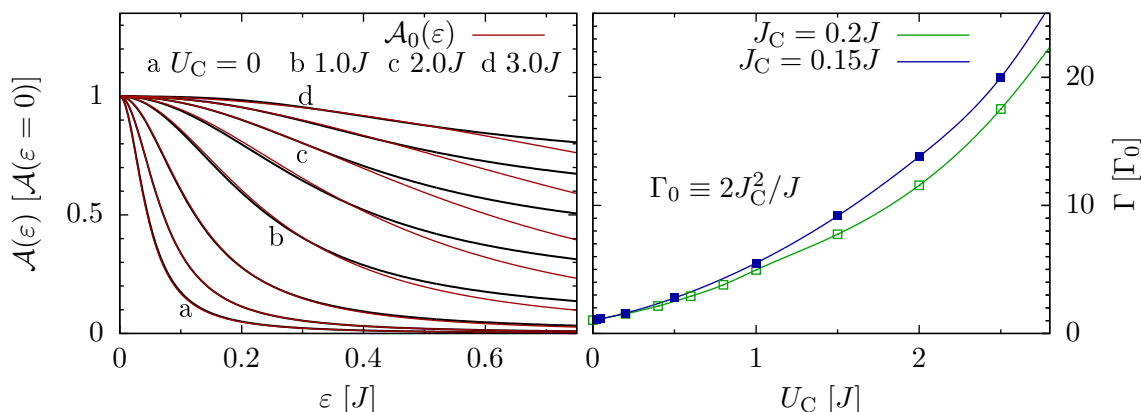
Figure 4.4 Left panel: Central peak of the spectral function for the IRLM, on resonance ($V_{\mathrm{g}} = 0$), normalized to the value for frequency $\varepsilon = 0$, for different values of the interaction U_{C}. The system consists of $M = 168$ lattice sites in total, the dot is coupled to the leads via $J_{\mathrm{C}} = 0.15J$. The red lines correspond to a fit of the non-interacting wide-band limit $\mathcal{A}_0(\varepsilon)$ to the numerical data (black lines). Right panel: Γ as function of U_{C}, for two different values of the coupling J_{C}, normalized to the width in the wide-band limit. Increasing U_{C} leads to monotonous growth of Γ. Lines are guides to the eye.

vanishes. Interestingly, Γ does not show any noticeable behaviour when passing the self-dual point $U_{\mathrm{C}} = 2J$, where certain non-equilibrium problems can be solved analytically [56, 85], and where the linear conductance obtains its maximum width [31]. Unfortunately, the plot for $\Gamma(U_{\mathrm{C}})$ can not be continued beyond $U_{\mathrm{C}} \approx 3J$ based on the available data due to the vanishing central peak. In order to do so, it will probably be necessary to further reduce J_{C} and at the same time to increase the energy resolution. This will then allow us to decide wether the vanishing of the central peak is an effect due to the poor energy resolution, or if it is an effect inherent to the system.

Summary and Outlook

In this chapter we have presented a method to extract the impurity Green's function of the IRLM by means of an expansion by orthogonal polynomials. We have compared the resulting spectral function for the situation with no electron-electron interaction with analytical results and find good agreement, even though the numerical data have been extracted from the simulation of a system with *finite size*, while the analytical calculation has been carried out for the thermodynamic limit. In order to remove the finite size broadening η, we applied a quadratic extrapolation of the self-energy for $\eta \to 0$, generalizing on the prescription discussed in [87] (*poor man's deconvolution*). We found the width of the central peak of the spectral function to grow monotonically, even for values of the interaction $U_{\mathrm{C}} > 2J$, beyond the self-dual point − in contrast, the linear conductance has been shown to grow in width up to

this point, and then to start shrinking again [31]. However, for values of $U_C > 3J$, the central peak disappears completely, which might be attributed to the poor energy resolution in the middle of the band. Improved boundary conditions [87] could help to decide wether this is an effect due to the poor energy resolution, or possibly a property that is inherent in the system, connected with the ratio of the coupling J_C and band width $4J$. Remarkably, for growing interaction, additional peaks show up, located *outside* the band. Since their positions seem to be independent of the coupling J_C, we conclude that these peaks must be related to the finite band width.

Finally we have to add that the results presented here are considered preliminary – more investigations have to be carried out to decide the open questions sketched above. Also, we did not yet carry out an error analysis. The Chebyshev moments μ_n, computed using the DMRG, contain a truncation error, related to the finite value of N_{cut}; cf. section 3.2. For the moment, we do not know if the results presented in this chapter show qualitative errors related to the truncation procedure.

Of course, this method is also applicable to other kinds of systems. For example, we are currently computing the local density of states for the 1D Hubbard model. Also, bulk Green's functions can be computed.

A great advantage over the correction vector method [30, 111] consists in the fact that the polynomial moments μ_n have to be computed only *once*, while the Green's function then can be evaluated for the whole range of values ω and η. Also, analytic manipulations can be incorporated on the level of the expansion coefficients α_n, which allows computation of the time-dependent correlation function $\langle \hat{c}^\dagger(t)\hat{c}(t=0)\rangle$ from the same set of numerical data, for example. The disadvantages of the method have also been discussed: the number of moments that has to be calculated for a given value of η scales *proportional* to the system size, and also *proportional* to $1/\eta$ (cf. section 3.4 and especially Eq. (3.95)). For resolving *narrow* structures in the spectrum, this method therefore might be inapplicable, or at least relatively expensive in terms of computation resources.

Non-equilibrium Green's functions   A generalisation to non-equilibrium Green's functions is straightforward. In view of the discussion of the extraction of current-voltage characteristics from real-time simulations in the next chapter, this would provide an alternative approach to the computation of current in a steady state, based on the direct evaluation of the Meir–Wingreen formula within the framework of DMRG. However, we did not yet implement the numerics that is necessary to compute the relevant polynomial moments, therefore we can not provide any results at this point. Instead, we contend ourselves with the discussion of the corresponding formulas, leaving the application to physical problems for future investigation.

Analogous to Eqns. (4.13, 4.14), we define ($\eta_1, \eta_2 > 0$, $\eta = \eta_1 + \eta_2$)

$$\mathcal{G}^+_{\hat{A},\hat{B}}(\omega + i\eta) = \frac{i\hbar}{2\pi} \int\limits_{-\infty}^{\infty} d\omega\,' \langle\Psi| \frac{1}{\hat{H} + \hbar(\omega' + i\eta_2)} \hat{A} \frac{1}{\hbar(\omega - \omega' + i\eta_1) - \hat{H}} \hat{B}|\Psi\rangle, \quad (4.29)$$

$$\mathcal{G}_{\hat{A},\hat{B}}^{-}(\omega+\mathrm{i}\eta) = -\frac{\mathrm{i}\hbar}{2\pi}\int\limits_{-\infty}^{\infty}\mathrm{d}\omega\,'\,\langle\Psi|\hat{A}\frac{1}{\hat{H}+\hbar(\omega'+\mathrm{i}\eta_2)}\hat{B}\frac{1}{\hbar(\omega-\omega'+\mathrm{i}\eta_1)-\hat{H}}|\Psi\rangle,\ (4.30)$$

for a non-equilibrium steady state $|\Psi\rangle$. Herefore we have made use of the relation

$$\frac{1}{2\pi}\int\limits_{-\infty}^{\infty}\mathrm{d}\omega\,\mathrm{e}^{-\mathrm{i}\omega t}\frac{\mathrm{i}}{x+\omega+\mathrm{i}\eta} = \frac{1}{2}\mathrm{e}^{\mathrm{i}(x+\mathrm{i}\eta)|t|}[1+\mathrm{sgn}(t)],\quad x,t\in\mathbb{R},\ \eta>0.\qquad(4.31)$$

Similar to Eqns. (3.80, 3.81) we may now apply a polynomial expansion to both operator functions,

$$f_{\hbar(\omega'+\mathrm{i}\eta_2)}^{+}(-\hat{H}) = \frac{1}{\hat{H}+\hbar(\omega'+\mathrm{i}\eta_2)},\quad f_{\hbar(\omega-\omega'+\mathrm{i}\eta_1)}^{+}(\hat{H}) = \frac{1}{\hbar(\omega-\omega'+\mathrm{i}\eta_1)-\hat{H}},\ (4.32)$$

separately, cf. Eq. (3.88). If we define the Chebyshev moments μ_{mn} as

$$\mu_{mn}^{+} = \langle\Psi|T_m(\tilde{H})\hat{A}T_n(\tilde{H})\hat{B}|\Psi\rangle,\quad \mu_{mn}^{-} = \langle\Psi|\hat{A}T_m(\tilde{H})\hat{B}T_n(\tilde{H})|\Psi\rangle,\qquad(4.33)$$

we can rewrite the Green's function as

$$\mathcal{G}_{\hat{A},\hat{B}}^{\pm}(\omega+\mathrm{i}\eta) = \pm\frac{\mathrm{i}\hbar}{2\pi}\sum_{m,n}\mu_{mn}^{\pm}\int\limits_{-\infty}^{\infty}\mathrm{d}\omega\,'\,\alpha_m^{+}\big(a(\hbar(\omega'+\mathrm{i}\eta_2)+b)\big)\times$$
$$\times\,\alpha_n^{+}\big(a(\hbar(\omega-\omega'+\mathrm{i}\eta_1)+b)\big),\quad(4.34)$$

with appropriate rescaling a and shift b, corresponding to a convolution of the expansion coefficients α_n^{+} as defined in Eq. (3.92).

Chapter 5

Non-Equilibrium Transport Simulations in Impurity Models

The numerical computation of the time evolution of an initial non-equilibrium state of a system that is composed of an interacting nanostructure coupled to noninteracting leads is the central subject of this work. In chapter 2 we shortly discussed how to cast the system in an appropriate model, while in chapter 3, we gave an overview of the numerical methods we used to obtain the time evolution of strongly correlated many-particle systems, based on the DMRG method. In the present chapter, we now turn to the application of the scheme to a situation, where a finite, time-dependent current is flowing through the nanostructure, driven by a bias voltage. The chapter is divided in two parts: First we discuss the concept of calculating the finite bias conductance of nanostructures based on real time simulations [43–49, 51–53, 55–60, 67] within the framework of the DMRG [61, 62, 64–66], with a strong focus on the effects resulting from the finite size of the model's Hamiltonian. Then we extend the approach to the evaluation of shot noise [84, 85].

In a first approach of time-dependent dynamics within DMRG, the time-dependent Schrödinger equation was integrated in the Hilbert space obtained in a finite lattice ground state DMRG calculation [43]. Since this approach does not include the density matrix for the time evolved states, its applicability is very limited. This problem was cured by extending the density matrix with the contributions of the wave function at intermediate time steps [44], while the DMRG was restricted to the infinite lattice algorithm. The calculations have been considerably improved by replacing the integration of the time-dependent Schrödinger equation with the evaluation of the time evolution operator using a Krylov subspace method for matrix exponentials and by using the full finite lattice algorithm [47]. An introduction to this approach has been given in chapter 3.

An alternative approach is based on wave function prediction [63]. There, one first calculates an initial state with a static DMRG. One iteratively evolves this state by combining the wave function prediction with a time evolution scheme. In contrast to the aforementioned full td-DMRG, one only keeps the wave functions for two time steps in each DMRG step. Different time evolution schemes have been implemented in the past using approximations like the Trotter decomposition, [45, 46, 55], or the Runge-Kutta method [48]. The idea of the adaptive DMRG method was combined

with the direct evaluation of the time evolution operator via a matrix exponential using Krylov techniques as described in Ref. [47]. Therefore the method involves no Trotter approximations, the time evolution is unitary by construction, and it can be applied to models beyond nearest-neighbour hopping.

In the first part of this chapter, we discuss the setup we use for the simulation in some detail. This includes a discussion of several possibilities to implement a finite bias voltage, the extraction of the current-voltage characteristics from numerical data that are strongly affected by finite-size effects, as well as a review of the results that have been obtained for a multi-level structure [49, 67]. Concerning finite-size effects, damped boundary conditions (DBC) have been applied in order to obtain an increased effective system size in the regime of small bias voltage [30, 59, 60, 88], where an improved scheme for linear conductance was presented in [31]. In the non-interacting case, this enhanced system size in the case of the DBC can be traced back to a shift of the discrete single particle energy levels of the system towards the center of the band. We demonstrate that this procedure can also be used when applying a bias voltage of the order of magnitude of the band width when handled carefully.

In the second part of this chapter (cf. section 5.6) we discuss a method to determine out-of-equilibrium shot noise in quantum systems from knowledge of their time evolution [84]. The main issues for the numerical computation do not depend on interaction effects. Therefore we first concentrate on the single resonant level model *without* interaction, where we obtain a complete characterisation of finite size effects at zero frequency. We find that the finite size corrections scale $\propto G^2$, where G is the differential conductance. We also discuss finite frequency noise, as well as the effects of DBC. For the interacting resonant level model, we show results at its self-dual point, where comparison with analytic calculations is possible [85], as well as for other values of the interaction. Finally we discuss the limitations of the method.

Interacting Nanostructure   The Hamiltonian for an interacting nanostructure coupled to two leads is given by Eqns. (2.16-2.20). For a sketch of the setup compare also Fig. 2.3. Since we concentrate on spinless fermions, we arrive at (structure: $\hat{H}_{\mathrm{S}}$, coupling: $\hat{H}_{\mathrm{C,L/R}}$, leads: $\hat{H}_{\mathrm{L/R}}$)

$$\hat{H}_{\mathrm{S}} = -\sum_{x=M_{\mathrm{L}}}^{M_{\mathrm{L}}+M_{\mathrm{S}}-2} J_{\mathrm{S},x}(\hat{c}_x^\dagger \hat{c}_{x+1} + \mathrm{H.c.}) + \sum_{x=M_{\mathrm{L}}}^{M_{\mathrm{L}}+M_{\mathrm{S}}-1} V_{\mathrm{g},x}\hat{n}_x + \sum_{x=M_{\mathrm{L}}}^{M_{\mathrm{L}}+M_{\mathrm{S}}-2} U_{\mathrm{S},x}(\hat{n}_x - \frac{1}{2})(\hat{n}_{x+1} - \frac{1}{2}), \quad (5.1)$$

$$\hat{H}_{\mathrm{C,L}} = -J_{\mathrm{C}}(\hat{c}_{M_{\mathrm{L}}-1}^\dagger \hat{c}_{M_{\mathrm{L}}} + \hat{c}_{M_{\mathrm{L}}}^\dagger \hat{c}_{M_{\mathrm{L}}-1}) + U_{\mathrm{C}}(\hat{n}_{M_{\mathrm{L}}-1} - 1/2)(\hat{n}_{M_{\mathrm{L}}} - 1/2),$$

$$\hat{H}_{\mathrm{C,R}} = -J_{\mathrm{C}}(\hat{c}_{M_{\mathrm{L}}+M_{\mathrm{S}}-1}^\dagger \hat{c}_{M_{\mathrm{L}}+M_{\mathrm{S}}} + \mathrm{H.c.}) + U_{\mathrm{C}}(\hat{n}_{M_{\mathrm{L}}+M_{\mathrm{S}}-1} - \frac{1}{2})(\hat{n}_{M_{\mathrm{L}}+M_{\mathrm{S}}} - \frac{1}{2}), \quad (5.2)$$

$$\hat{H}_{\mathrm{L}} = -J\sum_{x=0}^{M_{\mathrm{L}}-2}(\hat{c}_x^\dagger \hat{c}_{x+1} + \hat{c}_{x+1}^\dagger \hat{c}_x), \quad \hat{H}_{\mathrm{R}} = -J\sum_{x=M_{\mathrm{L}}+M_{\mathrm{S}}}^{M-2}(\hat{c}_x^\dagger \hat{c}_{x+1} + \hat{c}_{x+1}^\dagger \hat{c}_x), \quad (5.3)$$

$$\hat{H} = \hat{H}_{\mathrm{L}} + \hat{H}_{\mathrm{C,L}} + \hat{H}_{\mathrm{S}} + \hat{H}_{\mathrm{C,R}} + \hat{H}_{\mathrm{R}}. \quad (5.4)$$

The number of lattice sites in the leads (on the structure) is given by $M_{\mathrm{L/R}}$ (M_{S}), the structure is coupled symmetrically to the leads ($J_{\mathrm{C}} \equiv J_{\mathrm{C,L}} = J_{\mathrm{C,R}}$, the same for the electron-electron interaction U_{C}). We once more want to note that due to neglecting the spin degree of freedom, only nearest-neighbour interaction can be included, since an orbital can be occupied only once due to the Fermi statistics of the particles. The individual lattice sites are labelled according to Fig. 5.1.

Current   The current operator $\hat{I}_x$ at an arbitrary bond x can be derived from the charge operator $\hat{Q}_x = -e\hat{N}_x$ using a continuity equation $\partial_t \hat{Q}_x = -\hat{I}_x$, where for any one-dimensional tight-binding Hamiltonian the total particle number $\hat{N}_x$ in the subsystem "left of" a certain lattice site x is well defined by

$$\hat{N}_x = \sum_{x'=0}^{x} \hat{n}_{x'} \tag{5.5}$$

with the particle number $\hat{n}_{x'}$ on lattice site x'. In the Heisenberg picture this amounts to the equation of motion

$$\hat{I}_x \equiv -\frac{\mathrm{d}}{\mathrm{d}t}\hat{Q}_x = -\frac{\mathrm{i}}{\hbar}[\hat{H}, \hat{Q}_x]. \tag{5.6}$$

For the tight-binding Hamiltonian (5.4), the current operator and its expectation value with respect to a state $|\Psi\rangle$ take the form

$$\hat{I}_x = \mathrm{i}\frac{e}{\hbar}J_x\big[\hat{c}_x^\dagger \hat{c}_{x+1} - \hat{c}_{x+1}^\dagger \hat{c}_x\big] \quad \Rightarrow \quad I_x = -\frac{2e}{\hbar}J_x\,\mathrm{Im}\langle\Psi(t)|\hat{c}_x^\dagger \hat{c}_{x+1}|\Psi(t)\rangle. \tag{5.7}$$

We define the current through the nanostructure as an average over the current in the left and right contacts to the nanostructure

$$I(t) = [I_{M_{\mathrm{L}}-1}(t) + I_{M_{\mathrm{L}}+M_{\mathrm{S}}-1}(t)]/2. \tag{5.8}$$

Shot Noise   Shot noise is defined as the zero-temperature contribution to noise in a transport state. To obtain the noise power spectrum from a real time simulation, the current-current correlations in the time domain

$$S(t,t') = \frac{1}{2}\langle\Delta\hat{I}(t)\Delta\hat{I}(t') + \Delta\hat{I}(t')\Delta\hat{I}(t)\rangle \tag{5.9}$$

$$= \mathrm{Re}\langle\Delta\hat{I}(t)\Delta\hat{I}(t')\rangle \tag{5.10}$$

have to be calculated in a non-equilibrium zero-temperature state, where $\Delta\hat{I}(t) = \hat{I}(t) - \langle\hat{I}(t)\rangle$ [112, 113]. Therefore, the time-dependent expectation value

$$\langle\Delta\hat{I}(t)\Delta\hat{I}(t')\rangle = \langle\Psi|\mathrm{e}^{\mathrm{i}\hat{H}t/\hbar}\Delta\hat{I}\mathrm{e}^{-\mathrm{i}\hat{H}(t-t')/\hbar}\Delta\hat{I}\mathrm{e}^{-\mathrm{i}\hat{H}t'/\hbar}|\Psi\rangle \tag{5.11}$$

has to be evaluated. In a steady state with constant current the correlation function must fulfil $S(t,t') \equiv S(t-t')$. Then the noise power can be defined as the Fourier transform

$$2\pi\delta(\omega+\omega')S(\omega) = \langle\Delta\hat{I}(\omega)\Delta\hat{I}(\omega') + \Delta\hat{I}(\omega')\Delta\hat{I}(\omega)\rangle, \tag{5.12}$$

where

$$S(\omega) = 2 \int\limits_{-\infty}^{\infty} dt \ e^{i\omega t} S(t, t' = 0) = 4\mathrm{Re} \int\limits_{0}^{\infty} dt \ e^{i\omega t} S(t, t' = 0). \qquad (5.13)$$

The right-hand side of the equation accounts for the symmetry $S(t - t') = S(t' - t)$. In a steady state, of course, this expression should be independent of the choice of the time t'

$$S = 4\mathrm{Re} \int\limits_{t'}^{\infty} dt \ e^{i\omega(t-t')} S(t, t') \quad \forall \ t'. \qquad (5.14)$$

In the zero-frequency limit $\omega = 0$ this expression simplifies to

$$S \equiv S(\omega = 0) = 4 \int\limits_{t'}^{\infty} dt \ S(t, t') = 4 \int\limits_{t'}^{\infty} dt \ \mathrm{Re}\langle \Delta \hat{I}(t) \Delta \hat{I}(t') \rangle. \qquad (5.15)$$

Shot noise of the ground state We now assume that the expectation value $\langle \cdot \rangle$ is obtained for the ground state $|\Psi_0\rangle$ of the system. Based on general arguments it can be proven that in this case,

$$S(\omega = 0) = 0. \qquad (5.16)$$

For a proof, cf. section B.3. In section 5.6 we investigate shot noise for systems in a steady non-equilibrium state at finite bias voltage, where we focus on zero-frequency noise. For small values of the voltage we will find strong finite size effects, leading to non-zero shot noise even at zero bias voltage. For temperature $T = 0$, zero bias voltage is equivalent to the system being in its ground state, which means that there is a contradiction to Eq. (5.16). Under certain conditions it turns out to be possible to remove this finite size effect. In order to check the reliability of the numerical results, relation (5.16) therefore is very important in the context of this work.

5.1 Initial conditions and time evolution

The preparation of a strictly steady non-equilibrium state with constant finite current is possible only in the case of infinite leads. The "switching on" of the voltage, be it quenching of the leads by an additional chemical potential or connecting the initially isolated structure to leads with different potential, then is sent to the infinite past in analytic calculations in order to damp effects due to the voltage being switched. Instead, for the numerical simulation of the full time evolution of the complete system (including the structure *and* the leads), one is restricted to systems of finite size, as for example given by Eqns. (5.1-5.4). Then, strictly speaking, a steady non-equilibrium state is impossible. An excitation that is generated in the vicinity of the structure of interest will travel towards the boundaries of the system
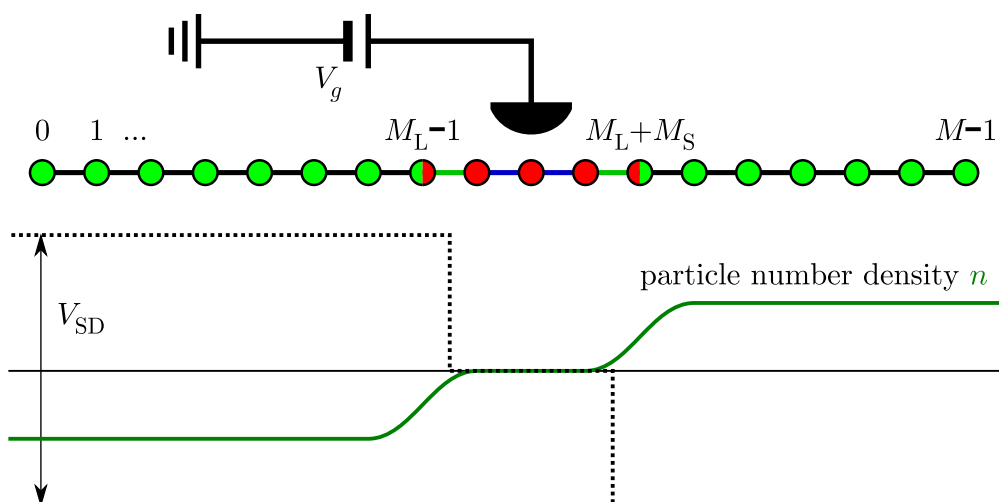
Figure 5.1 Interacting nanostructure attached to non-interacting leads and schematic density profile (green solid line) of the N-particle wavepacket at initial time $t = 0$. The density profile corresponds to the N-particle ground state of the Hamiltonian $\hat{H} + \hat{H}_{\mathrm{SD}}$, cf. Eq. (5.17), where the bias voltage enters as a local chemical potential V_{SD} (black dotted line).

where it gets reflected, disturbing the measurement at the structure. This imposes a maximum simulation time t_{R}, the *transit time*, which prohibits the initial time to be sent to the infinite past. On the other hand, after switching on the voltage at some initial time, the initial oscillating behaviour due to the switching will not decay before a certain *settling time* t_{S}. Knowing this, one has to restrict the measurement to a certain time interval $[t_{\mathrm{S}}, t_{\mathrm{R}}]$. The time scales of this type of finite size effect will be discussed in the following sections.

With that in mind, we now discuss several possible ways to generate a charge imbalance at initial time, imposing a voltage drop across the nanostructure. Following the prescription implemented in [47, 52] we add an external bias potential, namely the charge operator,

$$\hat{H}_{\mathrm{SD}} = \frac{V_{\mathrm{SD}}}{2}(\hat{N}_{\mathrm{L}} - \hat{N}_{\mathrm{R}}), \quad \hat{N}_{\mathrm{L}} = \sum_{x=0}^{M_{\mathrm{L}}-1} \hat{n}_x, \quad \hat{N}_{\mathrm{R}} = \sum_{x=M_{\mathrm{L}}+M_{\mathrm{S}}}^{M-1} \hat{n}_x \qquad (5.17)$$

to the unperturbed Hamiltonian $\hat{H}$, Eq. (5.4), and take the ground state $|\Psi_0\rangle = |\Psi(t = 0)\rangle$ of $\hat{H} + \hat{H}_{\mathrm{SD}}$, obtained by a standard finite lattice DMRG calculation, as the initial state at time $t = 0$ [47]. If the electron-electon interaction $U_{\mathrm{C}}, U_{\mathrm{S}}$ is neglected in Eqns. (5.1, 5.2), one may instead resort to exact diagonalisation techniques as described in section 3.1. The minimization of the energy of the system leads to a charge imbalance in the right (<u>s</u>ource) and the left (<u>d</u>rain) lead corresponding to V_{SD}, as sketched in Figs. 5.1, 5.2 (a). Alternatively, the bias voltage also can
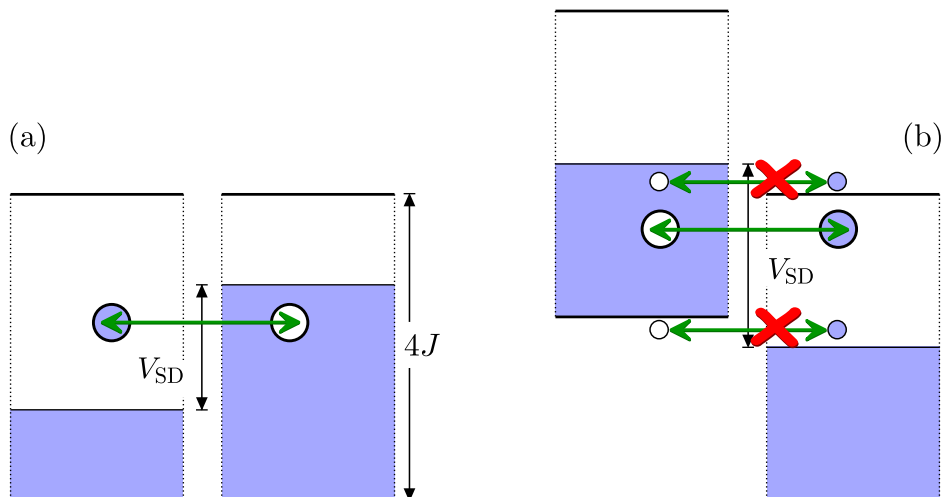
Figure 5.2 Different initial conditions, corresponding to (a) $\hat{H}_{\text{init.}} = \hat{H} + V_{\text{SD}}(\hat{N}_{\text{L}} - \hat{N}_{\text{R}})/2$ and (b) $\hat{H}_{\text{init.}} = \hat{H}$. The band width for the cosine band is $4J$. Assuming a single particle picture, we understand that in case (a), increasing the bias voltage V_{SD} to a value greater than the band width qualitatively does not change the initial state, since all particles populate only one of the two leads, while for case (b), quenching the leads to different energies at the initial time prevents some particles (holes) from tunneling from one lead to the other because of energy conservation. For this reason there is no current flow in the extreme case of $V_{\text{SD}} > 4J$, cf. Fig. 5.4.

be added to the time evolution. The initial state $|\Psi_0\rangle$ then has to be obtained as the ground state of the unperturbed Hamiltonian $\hat{H}$, while the time evolution is performed using $\hat{H} + \hat{H}_{\text{SD}}$, cf. also Figs. 5.2 (b).

5.1.1 Numerical time evolution

Starting from $|\Psi_0\rangle$, the time evolution of the system results from the time evolution operator $\hat{U}(t)$ with

$$|\Psi(t)\rangle = \hat{U}(t)|\Psi_0\rangle, \tag{5.18}$$

which leads to flow of the extended wave packet through the whole system until it is reflected at the hard wall boundaries as described in [47]. Corresponding to the two different schemes introduced before, $\hat{U}$ is given as either

$$\text{(a) } \hat{U}(t) = e^{-i\hat{H}t/\hbar} \quad \text{or (b) } \hat{U}(t) = e^{-i(\hat{H}+\hat{H}_{\text{SD}})t/\hbar}. \tag{5.19}$$

The time-dependent DMRG now computes a series of states $|\Psi(n\Delta t)\rangle$, $n \in \mathbb{N}$, starting from the initial state $|\Psi_0\rangle$, by repeatedly applying the time evolution operator for finite, but small time steps Δt

$$|\Psi((n+1)\Delta t)\rangle = U(\Delta t)|\Psi(n\Delta t)\rangle, \tag{5.20}$$

using the Krylov subspace method described in section 3.3. Typically, we choose Δt on the time scale determined by the hopping in the leads, $\Delta t \approx 0.5\hbar/J$, resulting in $\sim 10 \ldots 20$ Krylov iterations until the Krylov approximation has converged. The time-dependent current as defined in Eq. (5.7) then is evaluated as

$$I_x(t) = \langle \Psi_0 | U^\dagger(t) \hat{I}_x U(t) | \Psi_0 \rangle = \langle \Psi(t) | \hat{I}_x | \Psi(t) \rangle, \quad t = n\Delta t. \qquad (5.21)$$

Alternatively, for the non-interacting case, with $U_S = U_C \equiv 0$ in Eqns. (5.1-5.4), we can apply single-particle decomposition as discussed in section 3.1, since then the Hamiltonian of the system can be written in the form of Eq. (3.2). The time evolution of the current operator $\hat{I}_x$ can be expressed in terms of Eqns. (3.9-3.11),

$$\langle \Psi_0 | \hat{c}_x^\dagger(t) \hat{c}_{x+1}(t) | \Psi_0 \rangle = \sum_{x'y'} \mathcal{U}(t)_{x+1,y'} \Psi_0^{y'x'} \mathcal{U}^\dagger(t)_{x',x}, \quad \Psi_0^{y'x'} = \sum_\nu U_{y'\nu}^0 \tilde{n}_\nu[\Psi_0] U_{\nu x'}^{0\dagger}.$$

$$(5.22)$$

The time evolution here is given by $\mathcal{U}(t)$, the single-particle time evolution operator, constructed from the corresponding square form H_{xy} as defined in Eq. (3.2). The initial state enters in form of the matrix $\Psi_0^{y'x'}$. The unitary transform U^0 diagonalises the square form of the Hamiltonian the ground state of which serves as the initial state $|\Psi_0\rangle$ of the calculation. Finally, $n_\nu[\Psi_0]$ denotes the occupation number of the single particle states at zero temperature for the eigenstates of the *initial* Hamiltonian.

5.1.2 Analysis of the different time evolution schemes

The sudden switching of the bias voltage at initial time results in a ringing of the current in a transient time regime [114], see also Fig. 5.3 (a). Here we show the short time behaviour of the current through a single impurity coupled to two leads in a system with $M = 120$ lattice sites in total. This transient behaviour with its characteristic oscillations decays to a quasi-stationary state on the time scale $t_S \propto \Gamma$, where Γ is the width of the conductance peak. By smearing out the voltage drop over a few lattice sites one may reduce this effect. Furthermore, the finite size of the system leads to reflection of wave packets at the boundaries, cf. Fig. 5.3 (b). A wave packet travelling with Fermi velocity v_F from the impurity towards the boundaries will return to the impurity after a transit time given by $t_R \propto M/v_F$, which is the characteristic time scale for finite size effects appearing in the expectation value of time-dependent observables.

To compare the approaches (a) and (b), we show a current-voltage characteristics in Fig. 5.4 for the resonant level model with a single impurity ($M_S = 1$, cf. Fig. 5.1) coupled to two leads via the hopping matrix element $J_C = 0.4J$ and the gate voltage as well as the interaction set to $U_C = V_g = 0$. The dots correspond to results obtained numerically using exact diagonalisation, while the lines correspond to analytic calculations included for comparison. Here, the straight line shows the current assuming linear scaling with V_{SD} with linear conductance $g = e^2/h$, while the curved line overlaid by the numerical results for approach (a) has been obtained
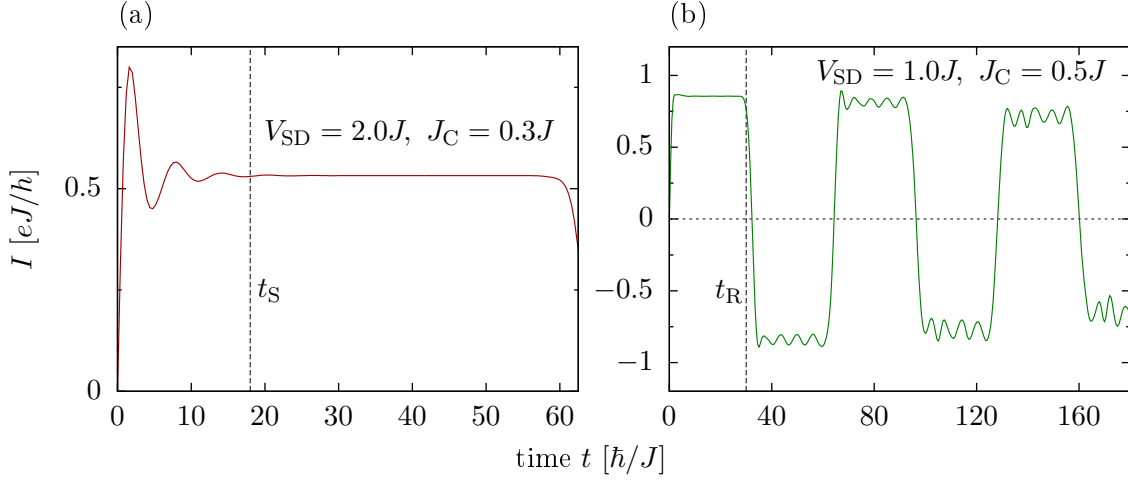
Figure 5.3 Time-dependent current through a single non-interacting impurity coupled to noninteracting 1D leads for vanishing gate voltage $V_\mathrm{g} = 0$. The system consists of M lattice sites and N particles at nominal filling $N/M = 0.5$. We find three time domains: 1. an initial transient regime with decaying oscillations, 2. a pseudo stationary current plateau and 3. finite size reflections. (a) Shortly after the initial switching of the bias voltage the time-dependent behaviour is dominated by oscillations which decay to a constant current plateau on the time scale t_S (here: $J_\mathrm{C} = 0.3J$, $M = 120$). (b) The finite size of the system leads to reflections at the boundaries. A wave packet that runs through the system starting at the impurity will be reflected at the boundaries and returns to the impurity after time t_R. This results in the typical pattern with recurrent sign changes of the current (here: $J_\mathrm{C} = 0.5J$, $M = 60$).
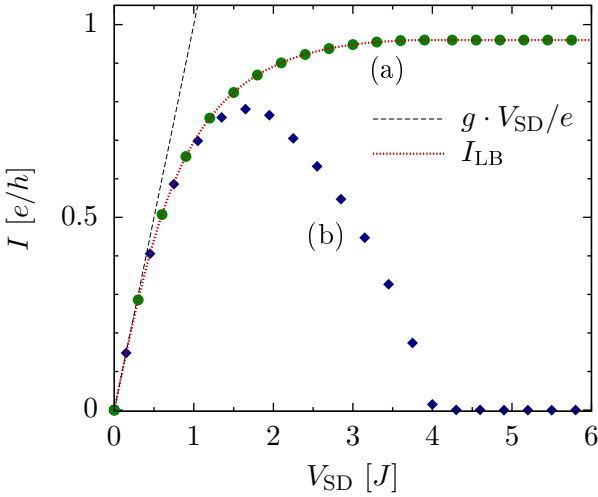
Figure 5.4
I–V-characteristics for the resonant level model with $J_\mathrm{C} = 0.4J$ and $V_\mathrm{g} = U_\mathrm{C} = 0$. The linear conductance is $g = e^2/h$. The plot shows results for two different time evolution schemes: (a) the initial state $|\Psi_0\rangle$ of the system is the ground state of the Hamiltonian $\hat{H} + \hat{H}_\mathrm{SD}$, while the time evolution is performed as $|\Psi(t)\rangle = \exp(-\mathrm{i}\hat{H}t/\hbar)|\Psi_0\rangle$. (b) $|\Psi_0\rangle$ is the ground state of $\hat{H}$, time evolution is performed as $|\Psi(t)\rangle = \exp[-\mathrm{i}(\hat{H} + \hat{H}_\mathrm{SD})t/\hbar]|\Psi_0\rangle$. For further discussion see Fig. 5.2 and the text.

using the Landauer–Büttiker approach, cf. also section B.1 in the appendix, taking cosine-dispersion into account.

The procedure of extracting the current from the numerical data will be described in the next section. Here we want to emphasize the different results we get for the I–

V-curve for the two different cases. For the tight-binding Hamiltonian the dispersion relation is given by $\varepsilon_k = -2J \cos k$, with a finite band width $4J$. For the approach (a), in the non-interacting case, this leads to a saturation of $I(V_{\mathrm{SD}})$ for all values of the bias voltage $V_{\mathrm{SD}} \geq 4J$. Further increasing V_{SD} beyond the band edge does not change the initial occupation of energy levels. In contrast, for the case (b), the particles will be distributed equally over the left and the right lead in the initial state $|\Psi_0\rangle$, whereas the voltage enters in the time evolution operator. For small values of V_{SD} we find a good agreement for $I(V_{\mathrm{SD}})$ for (a) and (b), while for $V_{\mathrm{SD}} \gtrsim 2J$ there is a mismatch which finds its expression in a current maximum for $0 < V_{\mathrm{SD}} < 4J$ with a subsequent break down to $I = 0$ for $V_{\mathrm{SD}} > 4J$. This behaviour has been predicted in [115] and can be understood from Fig. 5.2 (b), which explains how energy conservation prevents particles (holes) to tunnel from one lead to the other which removes contributions to the current. More recently, a detailed analysis of the negative differential conductance for the situation (b) has been carried out [116]. In this work, it has been realised that the density of states in the leads adds a major contribution to the breakdown of the current. Note that (a) corresponds to the situation of wide band metallic leads. Since our emphasis lies on the description of nanostructures attached to metallic leads we prefer to work in this approach. When describing situations with band gap materials as leads one should refer to approach (b).

Moreover, there are other approaches to how the initial state and the time evolution can be defined. For example, in addition to prescription (a), the coupling J_{C} and the interaction U_{C} can be set to zero for the calculation of $|\Psi_0\rangle$. In this case (c), both leads as well as the structure are totally independent systems, and there is a very intuitive connection of V_{SD} and the difference of the particle number in the left and the right lead, because the isolated leads can be described in a single particle picture. The drawback of this approach, which adds a sudden switching of J_{C} and U_{C} in addition to the switching of V_{SD} at initial time $t = 0$, is an enhanced transient regime and therefore a reduced plateau of constant current that we need to extract the I–V-curve from. In Fig. 5.5 we compare the time-dependent current obtained using the different initial conditions (a) and (c) for a single impurity coupled to two leads via $J_{\mathrm{C}} = 0.4J$, including a finite density-density interaction $U_{\mathrm{C}} = 2.0J$, for different values of V_{SD}. To evaluate the time evolution of a system with finite interaction numerically, we used the td-DMRG method, with parameters as described in the figure caption of Fig. 5.5. For both approaches (a) and (c), we find a time regime of (quasi) constant current. However, approach (a) has several advantages over (c): the current plateau is more consistent, which simplifies analysis, and to keep the discarded entropy $\mathcal{S}_{\mathrm{disc}}$ in the td-DMRG calculation below a predefined threshold, the number of states, which have to be kept in the DMRG, is considerably higher for (c) as compared to (a), making approach (c) computationally much more expensive. The latter point is illustrated in Fig. 5.6, where we compare the maximum dimension N_{cut} of the DMRG projection scheme that is necessary to keep $\mathcal{S}_{\mathrm{disc}} \lesssim 10^{-3}$, for different values of the bias voltage V_{SD}, of the gate voltage V_{g} and of the interaction U_{C}. We always find a much smaller value of N_{cut} for (a) as compared to (c).
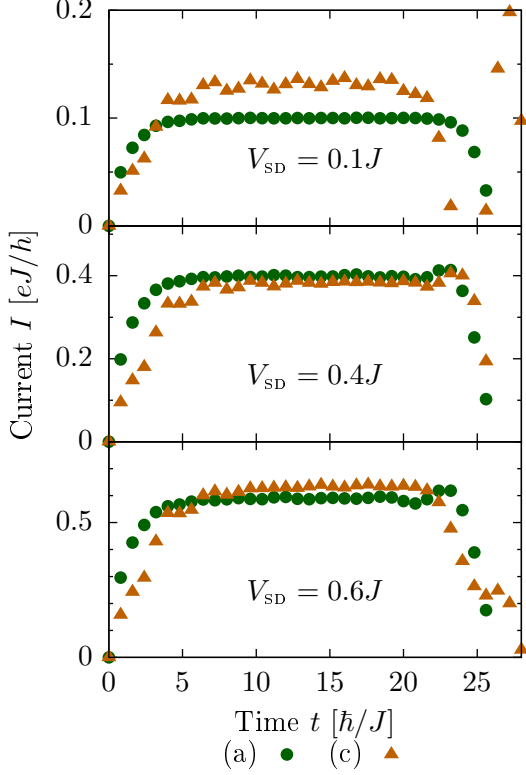
Figure 5.5
Time-dependent current through a single impurity coupled to noninteracting 1D leads with $J_C = 0.4J$ and $U_C = 2.0J$ for different values of V_{SD} and vanishing gate voltage $V_g = 0$. The system consists of $M = 48$ lattice sites and N particles at nominal filling $N/M = 0.5$. The current is obtained from a td-DMRG calculation by performing the time evolution on an initial non equilibrium state, using a DMRG projection scheme with a variable number of kept states $100 \leq N_{cut} \leq 5600$ with the discarded entropy $\mathcal{S}_{disc}$ kept below a certain value (here: $\mathcal{S}_{disc} \lesssim 10^{-3}$; cf. also Fig. 5.6). (a) The initial state $|\Psi_0\rangle$ corresponds to the situation sketched in Fig. 5.2(a) where $|\Psi_0\rangle$ is obtained as the ground state of $\hat{H}_{init} = \hat{H} + \hat{H}_{SD}$, (c) The initial state $|\Psi_0\rangle$ is obtained as the ground state of $\hat{H}_{init}\big|_{J_C=0, U_C=0}$. The current plateau we are looking for can be obtained more reliable when using prescription (a).

| | I $U_C = 1.0J$, $V_g = 0.0J$ | III $U_C = 2.0J$, $V_g = 0.0J$ | (a) |
| | II $U_C = 1.0J$, $V_g = 0.5J$ | IV $U_C = 2.0J$, $V_g = 0.5J$ | (c) |
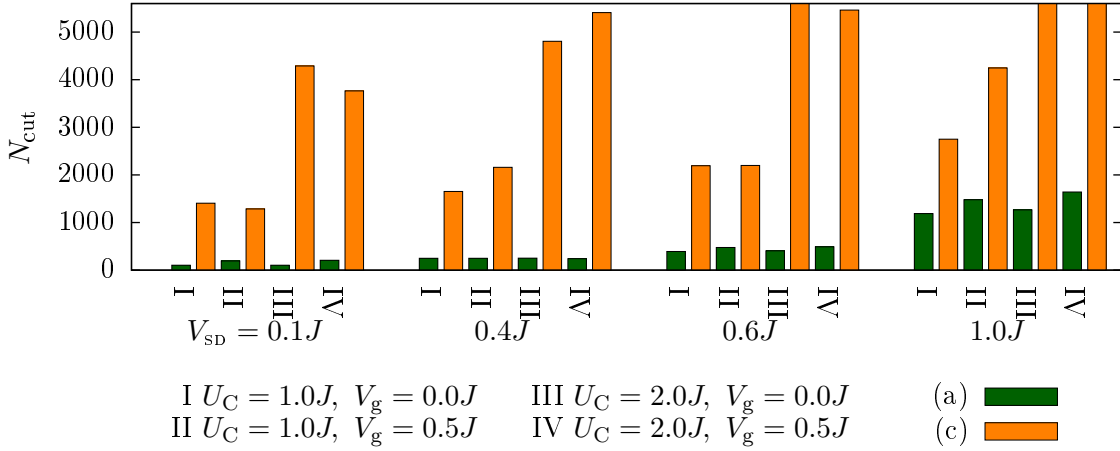
Figure 5.6 Maximum dimension N_{cut} of the DMRG projection scheme for an I–V-calculation necessary to keep the discarded entropy $\mathcal{S}_{disc}$ below a certain value (here: $\mathcal{S}_{disc} \lesssim 10^{-3}$) for different configurations I to IV and different values of the bias voltage V_{SD}, where we used $100 \leq N_{cut} \leq 5600$ states as a second limitation. Here, the current through the contact links to a single impurity with $J_C = 0.4J$ is obtained for 70 time steps ($\Delta t = 0.4\hbar/J$) in a system with $M = 48$ lattices sites at half filling. (a) The initial state $|\Psi_0\rangle$ is the ground state of $\hat{H}_{init} = \hat{H} + \hat{H}_{SD}$, (c) $|\Psi_0\rangle$ is obtained as the ground state of $\hat{H}_{init}\big|_{J_C=0, U_C=0}$.

Another problem of approach (c) is the discretization of the I–V-curve into steps resulting from the discrete single particle energy levels of the initial state; when increasing the voltage, the particles get transferred from one lead to the other one by one, as long as leads and structure are decoupled, whereas a finite coupling at initial time allows for continous charge transfer in between the leads. This could probably be handled using a procedure similar to the one described in section 5.3.2.

For these reasons we will use approach (a) throughout the remainder of this chapter.

5.2 Differential and linear conductance

For the calculation of the DC-conductance through the nanostructure the time evolution has to be carried out for sufficiently long times until a quasi-stationary state is reached and the steady state current I can be calculated. If the stationary state corresponds to a well-defined applied external potential V_{SD}, the differential conductance is given by $G(V_{SD}) = e \, \partial I(V_{SD})/\partial V_{SD}$. In the limit of a small applied potential, $V_{SD} \to 0$, the linear conductance is given by $g(V_{SD}) = eI(V_{SD})/V_{SD}$.

To discuss the general behaviour of the time evolution from an initial non-equilibrium state we first consider the most simple case we can think of: transport through a single impurity. The current rises from zero and settles into a quasi-stationary state, Fig. 5.3 (a). After the wavepackets have traveled to the boundaries of the system and back to the nanostructure, the current falls back to zero and changes sign, cf. Fig. 5.3 (b). Additionally there is a third type of finite size oscillations, Fig. 5.7. Here we show the time-dependent current for different configurations, from the leads to the impurity on a single (left or right) contact link, and through the impurity as defined in Eq. (5.8). After the initial oscillations have decayed on the time scale t_S, the current through a single contact link shows remaining oscillations, with an amplitude depending on V_{SD} and V_g, and proportional to the inverse of the system size $1/M$. The latter is demonstrated in Fig. 5.8. The period of the oscillation depends on the applied bias voltage, compare Fig. 5.7 (b, c), but is independent of the system size, Fig. 5.7 (b-d), and of the gate potential, Fig. 5.9, and is given by $t_J = 2\pi\hbar/|V_{SD}|$. In the resonant tunneling case (Fig. 5.7 (a), $V_g = 0$), the oscillations on the left and the right contact link cancel in the current average Eq. (5.8) due to a different sign in the amplitude of the oscillations $\tilde{I}_J$, which does not hold in general (Fig. 5.7 (b-d), $V_g \neq 0$), where the amplitude of the oscillations as a function of the gate potential V_g varies differently on the individual contact links, Fig. 5.9.

In Fig. 5.9 we plot the fit of the oscillation frequency $\tilde{\omega}_J = 2\pi/\tilde{t}_J$ as a function of the gate potential V_g for a fixed value of V_{SD}, where we find $\tilde{\omega}_J$ to be independent of the gate potential. To be precise, the fit nicely confirms the above relation of V_{SD} and oscillation period. This periodic contribution to the current is reminiscent of the Josephson contribution in the tunneling Hamiltonian, obtained by gauge transforming the voltage into a time-dependent coupling $\tilde{J}_C(t) = J_C \exp(iV_{SD}t/\hbar)$ [49, 110]. Like in a tunnel barrier in a superconductor, we have a phase coherent
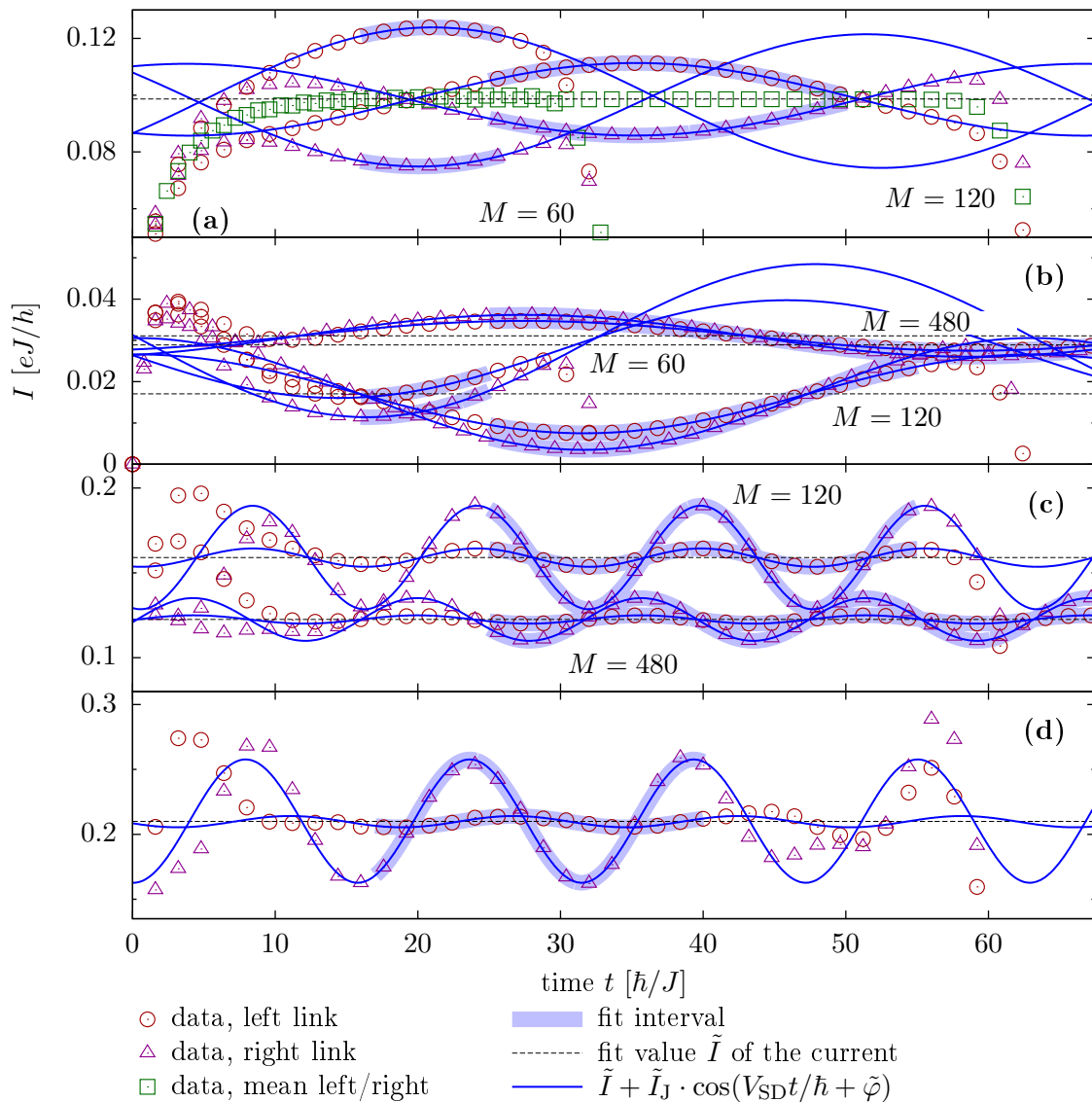
Figure 5.7 Current through a single impurity ($M_S = 1$) with $J_C = 0.3J$ at nominal filling $N/M = 0.5$ obtained from exact numerical diagonalization (a-c), or DMRG including interaction (d), respectively – (a) for different system sizes M at bias voltage $V_{SD} = 0.1J$ and gate voltage $V_g = 0$. The black dashed line corresponds to the mean value of the fit values $\tilde{I}$ for the left and right contact link, for $M = 60$ lattice sites. The fit interval has to be chosen carefully – initial oscillations from the bias voltage switching and the finite transit time have to be taken into account. Even though the period of the finite size oscillations considerably exceed the system size $M = 60$ for $V_{SD} = 0.1J$, the fit current $\tilde{I}$ is in nice agreement with the current plateau of the $M = 120$ system. However, finite size effects still have to be addressed (b, $V_g = 0.3J$, $V_{SD} = 0.1J$, and c, $V_g = 0.3J$, $V_{SD} = 0.4J$) since in general the fit current can strongly depend on the system size – in particular, a non-zero gate voltage changes the particle number density in the leads when the overall particle number is fixed. The same fit procedure can be applied to interacting systems (d, $U_C = 2.0J$, $V_{SD} = 0.4J$, $V_g = 0.3J$).

quantum system, namely the ground state at zero temperature. Instead of the superconducting gap we have a finite size gap resulting from the finite nature of the leads. Therefore the amplitude of this residual wiggling vanishes proportional to the finite size gap provided by the leads.

The stationary current is given by a fit to $\tilde{I} + \tilde{I}_J \cos(2\pi t/t_J + \tilde{\varphi})$ with the fit-parameters tagged by a tilde, where we do not fit the oscillation period t_J because it is known. In general, the density in the leads, and therefore also the current, depends on the system size and a finite size analysis has to be carried out in order to extract quantitative results (Fig. 5.7 (b,c), see also discussion of Fig. 5.17). Only in special cases (particle-hole symmetry, half filled leads, and zero gate potential) the stationary current is independent of the system size, cf.Fig. 5.7 (a).

5.3 Finite size effects

Finite size effects such as the finite transit time of a wave packet travelling through the system and the periodic contribution to the current make it difficult to obtain a pseudo-stationary state where a constant current can be extracted from the time evolution. This problem can be treated by a fit procedure as discussed in the previous section. However, in the small bias regime, where the amplitude of the oscillations is bigger than the (expected) current and the oscillation time t_J exceeds the transit time, this approach is unreliable. In section 5.5 we discuss the possibility of effectively enlarging the system using damped boundary conditions (DBC) while keeping the system size M constant (cf. Fig. 2.4). Furthermore, the time evolution of the current strongly depends on the number of lattice sites of the leads being even or odd, Figs. 5.10, 5.12. In Fig. 5.10 we compare this effect for a non-interacting two-dot structure for different system sizes in the regime of very small voltage $V_{SD} \ll J$, where we consider three qualitatively different cases, (a) $t_R \ll t_J$, (b) $t_R \approx t_J$ and (c) $t_R \gg t_J$, where t_R, t_J denote the transit time and oscillation period respectively, as discussed in section 5.1. Since the number of single particle energy levels is equal to the number of lattice sites, these relations are connected to V_{SD} and the level spacing $\Delta\varepsilon$ as, (a) $\Delta\varepsilon \gg V_{SD}$, (b) $\Delta\varepsilon \approx V_{SD}$ and (c) $\Delta\varepsilon \ll V_{SD}$. Intuitively one would expect that the level discretisation must be small compared to the energy scales of interest, and indeed we find, that on the time scale $t < t_R$ the numerical simulation fits best with the analytic result I_{LB} obtained from the Landauer–Büttiker approach in case (c) (see Fig. 5.10; cf. also section B.1 in the appendix). However, in all cases, the time evolution of the current depends on the different configurations of the leads with even or odd number of lattice sites. Two aspects must be distinguished: (1) the qualitative difference in the time evolution depending on whether the number of lead sites is equal (as for the e2e and the o2o configuration), or unequal (as for the e2o and the o2e configuration), is clearly demonstrated in the figure. For the two-dot structure, this holds true even for $t_R \gg t_J$, Fig. 5.10 (c). For the o2o and the e2e configurations we find a behaviour where the current suddenly increases by a factor of ~ 2 after the transit time t_R has passed, as opposed to the "expected" behaviour
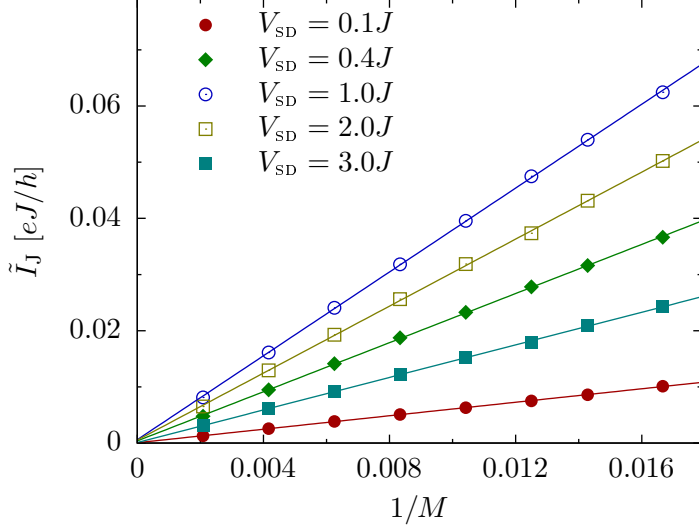
Figure 5.8
Oscillation amplitude $\tilde{I}_J$ from fits as shown in Fig. 5.7, as function of the inverse system size $1/M$ for different values of V_{SD}, of the time-dependent current through a single contact link to a single impurity, with $J_C = 0.5J$ and $V_g = 0$.
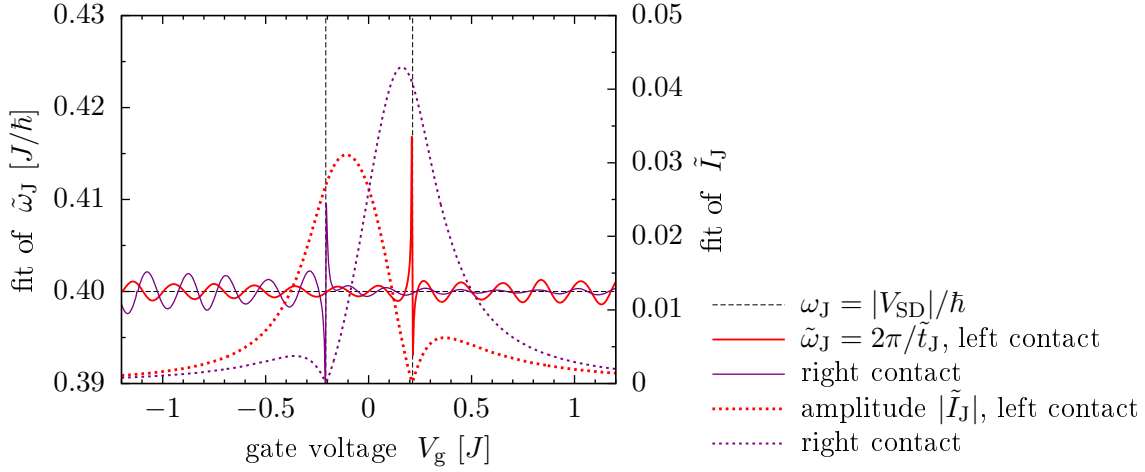

Figure 5.9 Fit of the oscillation frequency $\tilde{\omega}_J = 2\pi/\tilde{t}_J$ of the Josephson oscillations in a system with $M = 120$ lattice sites and a single resonant level with $J_C = 0.3J$ at a bias voltage $V_{SD} = 0.4J$. The oscillation period extracted from the time evolution of the current is in excellent agreement with the analytical expression $\omega_J = |V_{SD}|/\hbar$. The kinks that appear in $\tilde{\omega}_J$ can be traced back to the fact that the amplitude of the oscillations $\tilde{I}_J$ vanishes for $V_g \approx \pm V_{SD}/2$ at either the left or the right contact link. The residual wiggling (its amplitude as well as its frequency) depends on the size and the position of the fit interval, $[t_{min}, t_{max}]$, and is therefore consistent with a finite fitting interval in time domain.

with a sign change, seen for the o2e and the e2o configuration. (2) An overall odd number of lattice sites M (the o2e and the e2o configurations, for example) shifts the filling factor in the leads away from 0.5 due to their finite size. A similar effect results from applying a gate voltage $V_g \neq 0$, which imposes a problem to the extraction of the linear conductance. A possible solution is discussed in Sec. 5.3.2.

5.3.1 Even-odd effect

In [58], a detailed analysis of finite size effects resulting from an even or odd number of lattice sites in the leads for a single-dot and for a three-dot structure with on-site interaction including the spin degree of freedom has been carried out. The behaviour of the time dependence of the current resulting from the type of the lead (<u>e</u>ven or <u>o</u>dd number of sites) has been traced back to the different magnetic moment of the system which is $S_{\text{total}}^z = 1/2$ for an overall odd number M of lattice sites and $S_{\text{total}}^z = 0$ for M being even. The reduction of the current in a situation where the leads both consist of an even number of sites (ene) as compared to the other possible combinations (one, ono) has been explained by the accumulation of spin on the structure in the first case corresponding to the effect of applying an external magnetic field.

We already find parity effects in the time dependence of noninteracting spinless fermions in a system with a single-dot or a two-dot structure, Figs. 5.10, 5.12. In the following we will trace the parity effects back to the level structure in the leads. The single particle levels ε_k of an uncoupled, noninteracting lead with M_α sites ($\alpha = \text{L}, \text{R}$) are given by $\varepsilon_k = -2J \cos[\pi k/(M_\alpha + 1)]$, $k = 1, \ldots, M_\alpha$. The energy of a particle residing on a decoupled single dot structure ($J_\text{C} = 0$) is simply given by the gate voltage $\varepsilon_\text{d} = V_\text{g}$, which is at the Fermi edge for $V_\text{g} = 0$. For a decoupled M_S-dot structure one gets $\varepsilon_{\text{d},j} = -2J_\text{S} \cos[\pi j/(M_\text{S}+1)] + V_\text{g}$, $j = 1, \ldots, M_\text{S}$. For an equal number of sites on both leads (as for example eM_Se or oM_So) there is a twofold degeneracy of the single particle lead levels which does not exist if $M_\text{L} = M_\text{R} \pm 1$. In the degenerate case, single particle eigenfunctions can be constructed with a fully delocalized particle density while for $M_\text{L} = M_\text{R} \pm 1$, the density profile of the single particle wave functions shows an alternating confinement of the particle on either the left or the right lead. The same holds true for the energy levels of the structure: if degenerate with a lead level, the single particle wave function can be distributed over the whole lead while it is localized on the structure otherwise. In the e1e case, the single-dot level is not degenerate with the lead levels when $\varepsilon_\text{d} = 0$. As a result, a single particle occupying the dot level generates a sharp peak in the density profile (as well as the spin profile). For the o1o case on the other hand, both leads have one energy level in the middle of the band, which together with the dot level generates a threefold degeneracy. For finite coupling $J_\text{C} > 0$, the degeneracy of the lead levels and of the levels of the structure with the lead levels gets lifted. The single particle wave functions must be divided equally on both leads, when $M_\text{L} = M_\text{R}$, while the alternating confinement is preserved for $M_\text{L} = M_\text{R} \pm 1$. Concerning the energy level of the dot, the threefold degeneracy in the uncoupled o1o case results in two levels with strong localization on the dot, one lifted above the Fermi edge and one pushed below, and a third level with vanishing particle density on the dot, remaining on the Fermi edge. Compare also appendix A.

In a system with an odd number of lattice sites M and spinless electrons, half filling can not be realized strictly since $N = M/2$ is not an integer. Adding spin shifts the particle number at half filling to $N = M$ but leaves a total spin $S_{\text{tot}}^z = \pm 1/2$,
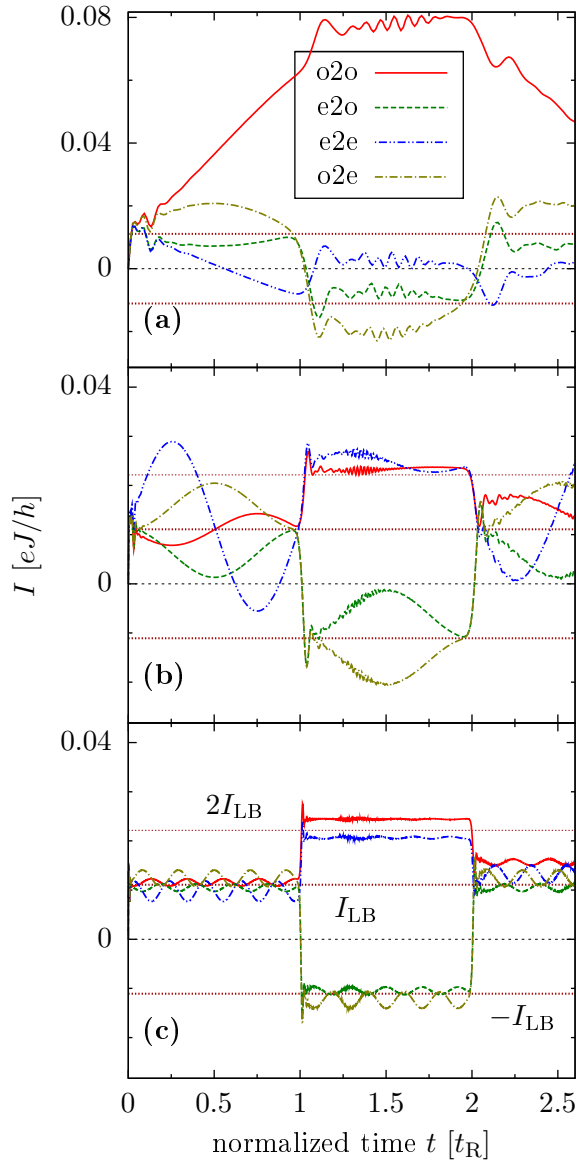
Figure 5.10
Current through the contact link of a structure with two dots ($J_S = J$), coupled to leads with a finite number of sites M and $J_C = 0.5J$ (compare also Fig. 5.1), at nominal half filling $N/M = 0.5$ obtained from exact numerical diagonalization for bias voltage $V_{SD} = 0.05J$. The horizontal dotted lines represent the analytical result I_{LB} obtained from the Landauer–Büttiker approach. The current is measured on the left link to the structure. The time axis is normalized to the transit time $t_R = M\hbar/(2J)$. Here, the focus is on finite size effects in the low voltage regime. We distinguish three cases: the system size is very small in case (a) where $M = 60+x$ with $x = 0$ (29 lattice sites on the left and right which is an <u>o</u>dd number in both cases o2o), $x = 1$ (now 30 sites on the left which is an <u>e</u>ven number e2o), $x = 2$ (e2e) and $x = 3$ (o2e). Here, the single particle level spacing $\Delta\varepsilon$ is much bigger than V_{SD}, while the period of the Josephson oscillations $t_J = 2\pi\hbar/|V_{SD}|$ is much bigger than the transit time t_R. Case (b) shows an intermediate situation with $M = 252 + x$ lattice sites ($\Delta\varepsilon \approx V_{SD}$, $t_J \approx t_R$). (c) $M = 1200 + x$ ($\Delta\varepsilon < V_{SD}$, $t_J < t_R$). For the e2o and the o2e case one has to do a density shift correction of the result since the total number of particles $N \neq M/2$, cf. Sec. 5.3.2.

which will occupy the highest single particle level. Since for the doubly occupied levels the spin adds up to 0, the level at the Fermi edge determines the spin density profile which then explains the density peak on the dot in the e1e case and the absence of a peak in the o1o case. The time-dependent behaviour of the current can now be traced back to the single particle energy levels being confined in a single lead (fully delocalized) in the case of different numbers of lattice sites $M_L = M_R \pm 1$ (equal number of lattice sites $M_L = M_R$). For the eM_So and oM_Se configurations, applying a bias voltage as in Eq. (5.17) leads to an alternating occupation of the energy levels corresponding to the alternating confinement of the single particle wave functions in the left or the right lead. In contrast we find an occupation number

of 1/2 in the energy range $-V_{\rm SD}/2 \ldots V_{\rm SD}/2$ when $M_{\rm L} = M_{\rm R}$, corresponding to the fully delocalized single particle wave functions. We demonstrate this behaviour for the non-interacting resonant level model (RLM) in Fig. 5.11.

So far, we have a connection of the degeneracy of the single particle energy levels for the situation where the impurity is decoupled from the leads with the respective class of the system ($eM_{\rm S}o$ / $oM_{\rm S}e$, $oM_{\rm S}o$, $eM_{\rm S}e$). The situation changes when adding a constant local potential

$$\Delta \hat{V} = \Delta V_{\rm L} \hat{N}_{\rm L} + \Delta V_{\rm R} \hat{N}_{\rm R} \tag{5.23}$$

to *both*, the initial *and* the time evolution Hamiltonian. To obtain the data of the *dotted* lines in Fig. 5.12 we calculated the single particle energy levels for a system with an even (odd) number of lattice sites in the leads and then applied a relative shift of the lead levels with $\Delta V_{\rm L} = -\Delta V_{\rm R} \in \{\Delta\varepsilon/4, \Delta\varepsilon/2\}$ for the two-dot structure and $\Delta V_{\rm L} \in \{\pm\Delta\varepsilon/2\}$, $\Delta V_{\rm R} = 0$ for the single dot structure, where $\Delta\varepsilon$ is the energy gap to the first unoccupied energy level. This allows us to change the level structure of a certain lead configuration in a way that it resembles one of the other configurations in the vicinity of the Fermi edge without changing the number of lattice sites in the leads. In Fig. 5.12 we see that the time-dependent behaviour of the system on the time scale $t < t_{\rm R}$ is only given by the structure of the single particle energy levels that contribute to the current, and the bias voltage $V_{\rm SD}$, at least as long as we do not include interaction. We therefore conclude that $oM_{\rm S}o$ as
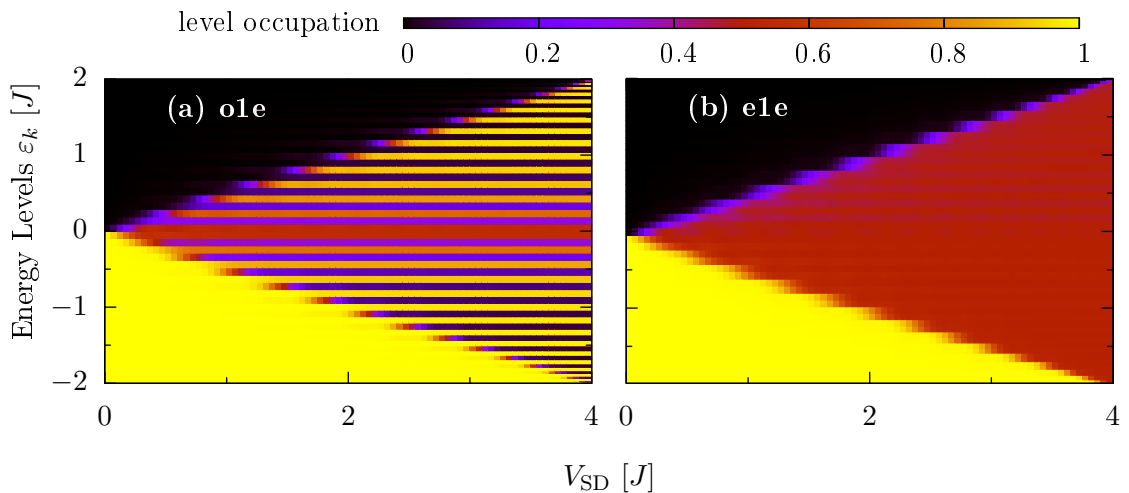
Figure 5.11 Initial occupation of the single particle energy levels in the non-interacting RLM ($J_{\rm C} = 0.4J$) at half filling. The number of lattice sites is $M = M_{\rm L} + M_{\rm R} + 1$ with the number of lattice sites in the left (right) lead $M_{\rm L}$ ($M_{\rm R}$). (a) $M_{\rm L} + 1 = M_{\rm R} = 30$. The alternating occupation can be traced back to the alternating constraint of the single particle wave functions in either the left or the right lead. (b) $M_{\rm L} = M_{\rm R} = 30$. In the uncoupled case ($J_{\rm C} = 0$), the energy levels of the leads are degenerate. Therefore the energy levels can not be associated with only one lead.
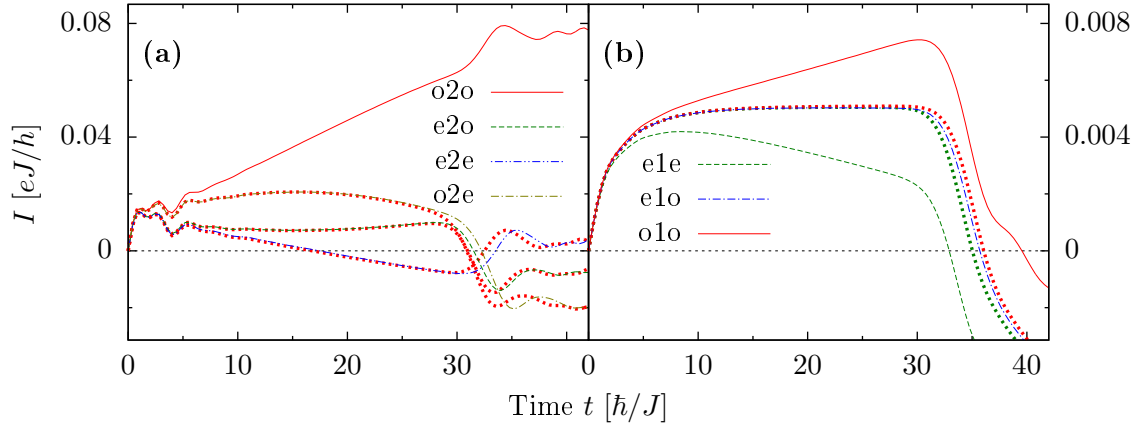
Figure 5.12 Current through a structure coupled to two leads (mean value of left and right contact link) with an overall finite system size M at half filling obtained from exact diagonalization. The figure demonstrates the influence of the number of lattice sites in the leads (<u>e</u>ven or <u>o</u>dd) on the current for a bias voltage V_{SD} smaller than the single particle level spacing. The dotted lines represent a situation where an additional constant voltage ΔV is applied to both leads (a) or to the left lead (b), respectively. $\Delta V \neq 0$ results in a shift of the single particle levels in the uncoupled leads which can be used to "mimic" the different combinations of leads with an even or odd number of lattice sites. (a) $M = 60 + x$, $x = 0$ (o2o), 1 (e2o), 2 (e2e) and 3 (o2e) where the number of electrons is $N = 30$ for $M = 60, 61$ and $N = 31$ for $M = 62, 63$. The dotted lines all together are generated using a system with $M = 60$ lattice sites, with $\Delta V \neq 0$. The different situations e2o and o2e can be recovered by changing the particle number from $N = 30$ to $N = 31$, cf. section 5.3.2. (b) $M = 61 + x$, $x = 0$ (e1e), 1 (o1e) and 2 (o1o) where the particle number is fixed to $N = 31$. Here, the green (red) dotted line is generated from the e1e (o1o) system.

well as eM_{S}e configurations also can be used to study the I–V-characteristics in the low voltage regime. This may be interesting when investigating structures with an even number of lattice sites on the structure, when the constraint $N = M/2$ has to be fulfilled strictly.

5.3.2 Density shift in the leads resulting from finite system size

For the single resonant level model (RLM) the condition of half filling is easily fulfilled by setting the particle number $N = M/2$ as long as the dot level resides in the middle of the band. Then the overall particle number density is $N/M = 1/2$ in the equilibrium case. This can change for different reasons: for example, for a model with two lattice sites in the structure and an overall odd number of lattice sites as discussed before half filling is not realisable, since $M/2$ is not an integer. But even for the RLM, applying a gate voltage $V_{g} \neq 0$ changes the particle number on the structure by ΔN_{S} while changing the particle number per site in the leads by $-\Delta N_{S}/(M-1)$ which shifts the lead filling away from 1/2 as long as the system

size M is finite. In this section we will concentrate on the latter case.

The impact on the current can be quite large, compare Figs. 5.13, 5.14. The total number of particles must therefore be corrected in such a way that $N_{\text{Leads}}/(M-1) = 1/2$ where $N_{\text{Leads}} = N - N_{\text{S}}$ is the particle number in the leads. Thus an initial state $|\Psi_{\text{i}}\rangle$ has to be a mixture of states with different particle numbers $|\Psi_N\rangle$ and $|\Psi_{N+1}\rangle$, or $|\Psi_{N-1}\rangle$, respectively, depending on the sign of ΔN_{S}

$$|\Psi_{\text{i}}\rangle = \alpha|\Psi_N\rangle + \beta|\Psi_{N\pm1}\rangle, \tag{5.24}$$

so that

$$\langle\Psi_{\text{i}}|\hat{N}_{\text{Leads}}|\Psi_{\text{i}}\rangle = \frac{M-1}{2}. \tag{5.25}$$

For particle number conserving operators $\hat{O}$ the expectation value reads

$$\langle\Psi_{\text{i}}|\hat{O}|\Psi_{\text{i}}\rangle = |\alpha|^2\langle\Psi_N|\hat{O}|\Psi_N\rangle + |\beta|^2\langle\Psi_{N\pm1}|\hat{O}|\Psi_{N\pm1}\rangle \tag{5.26}$$

which leads to the condition

$$|\alpha|^2\langle\Psi_N|\hat{N}_{\text{Leads}}|\Psi_N\rangle + |\beta|^2\langle\Psi_{N\pm1}|\hat{N}_{\text{Leads}}|\Psi_{N\pm1}\rangle = \frac{M-1}{2}, \qquad |\alpha|^2 + |\beta|^2 = 1. \tag{5.27}$$

Since the current operator $\hat{I}_x$ also is particle number conserving, the resulting time-dependent current expectation value is an interpolation of the results for N and for
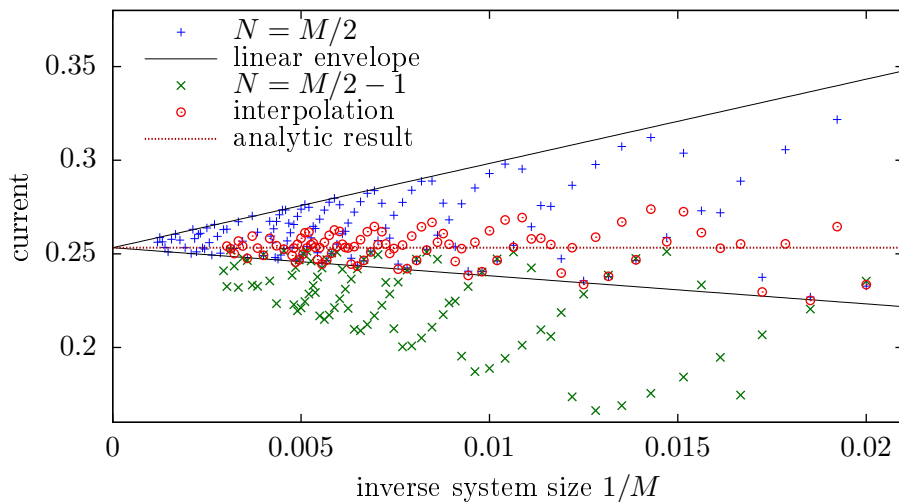
Figure 5.13   Current through a single impurity with an applied gate voltage $V_{\text{g}} = 0.21J$ for $V_{\text{SD}} = 0.5J$, coupled to two leads ($J_{\text{C}} = 0.3J$), as a function of the system size. The analytic result is obtained using the Landauer–Büttiker formula. While for different fillings ($N = M/2$ and $N = M/2 - 1$) there is a systematic deviation from the analytic result, the interpolation results in a substantial improvement. The linear envelope is plotted to highlight the $1/M$-dependency of the finite size effects. For an explanation of the sinusoidal oscillations see also Fig. 5.14 and the text.

$N \pm 1$ particles in the system

$$I_x(t) = |\alpha|^2 I_x(t; N) + (1 - |\alpha|^2) I_x(t; N \pm 1). \tag{5.28}$$

In Fig. 5.13 we show the dependency of the current through a single impurity coupled to two leads on the system size for different fillings $N = M/2$ as well as $N = M/2 - 1$, for a constant value of the bias voltage V_{SD} and the gate voltage V_{g}. Furthermore we include the interpolated value, following the procedure described before. We find that the interpolated results are centered around the analytic value, in contrast to the case with fixed particle number. However a distribution with an amplitude $\propto 1/M$ remains. A potential relation of the sinusoidal oscillations in the original data to the relative position of $V_{\text{SD}}/2$ to the single particle energy levels is illustrated in Fig. 5.14. Here, we show the current as a function of V_{SD} with $V_{\text{g}} \neq 0$, where we also apply the interpolation procedure. We compare the analytical result obtained using the Landauer–Büttiker approach with numerical data for the current through a single impurity coupled to two leads with a system size of $M = 62$ lattice sites in total. In order to interpolate the current as described before, Eq. (5.28), we simulated the time evolution of the current expectation value with $N = 30$ and $N = 31$ particles in the system. In comparison to Fig. 5.13 we conclude that one
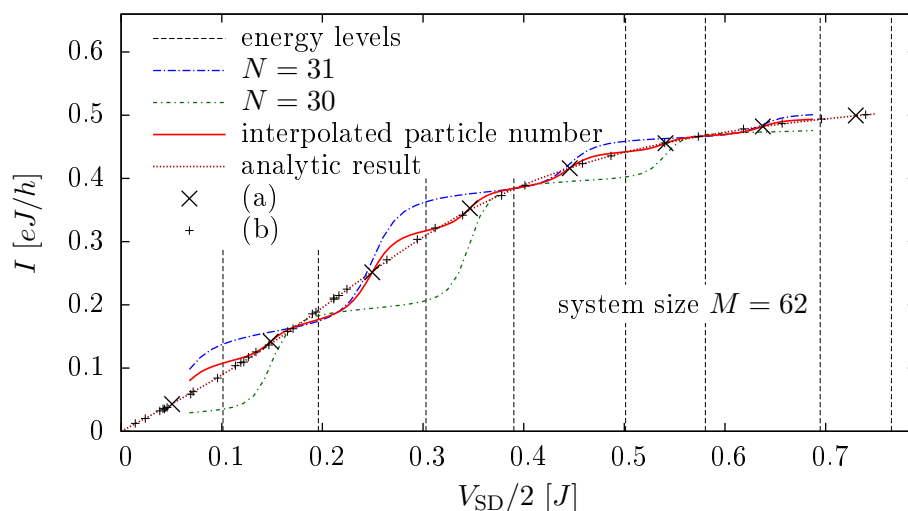
Figure 5.14 Current through a single impurity with an applied gate voltage $V_{\text{g}} = 0.21J$, coupled to two leads ($J_{\text{C}} = 0.3J$), as a function of the voltage V_{SD}. The vertical lines represent the single particle energies of a system with uncoupled leads ($J_{\text{C}} = 0.0$); we find that the interpolated value of the current fits best with the analytical result if the bias voltage is chosen as the mean value of two neighbouring energy levels (a). However, this condition restricts the bias voltage to only a few values. The restriction can be circumvented by either increasing the number of lattice sites M or by using damped boundary conditions. The latter was used to obtain the values (b) without changing M – see section 5.5.3 for discussion.
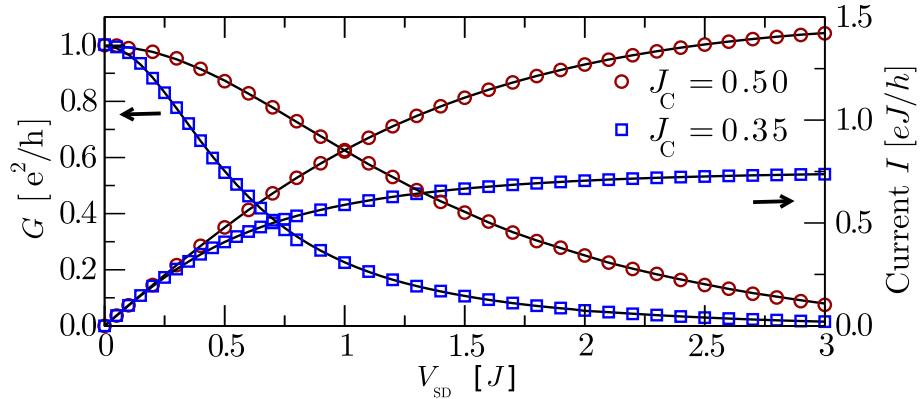
Figure 5.15 Current and differential conductance as function of applied potential through a single impurity with $V_g = 0$ and half filled leads: $N/M = 0.5$. Circles (squares) show results for $J_C = 0.5J$ $(0.35J)$. System size was $M = 48$ $(M = 96)$ and $N_{cut} = 200$ (400) states were kept in the DMRG. Lines are exact diagonalization results for $M = 512$.

has to choose the system size in relation to the bias voltage carefully to get the desired relation of V_{SD} and the single particle levels. More precisely, the data points (a), that fit nicely with the analytic curve, correspond to the interpolated current obtained for a bias voltage where $V_{SD}/2$ has been chosen as the mean value of two neighbouring energy levels of the uncoupled ($J_C = 0$) system. Another possibility is the use of damped boundary conditions to shift the single particle levels, which yields the data points (b). This idea will be discussed in Section 5.5.3.

A generalisation of this concept to systems with structures of $M_S > 1$ sites with a corresponding number of energy levels is straightforward. A varying gate voltage will change the occupation of the structure in a range $N_S \in [0, M_S]$ with a corresponding change of the particle number in the leads. To get reliable results for the current at half filling in the leads it is then necessary to perform an interpolation of currents with appropriate particle numbers. Results for the linear conductance of a 7-site structure are discussed in the next section.

5.4 Results for the conductance

The result[1] for the differential conductance through a single impurity in Fig. 5.15 is in excellent quantitative agreement with exact diagonalization results already for moderate system sizes and DMRG cutoffs. Accurate calculations for extended systems with interactions are more difficult, mainly because the numerical effort required for our approach depends crucially on the time to reach a quasi-stationary state. For the single impurity, the quasi-stationary state is reached on a timescale

---

[1]The results of this section have been presented in [49] for the first time. In order to demonstrate the reliability of the methods discussed before, we include these results at this point.
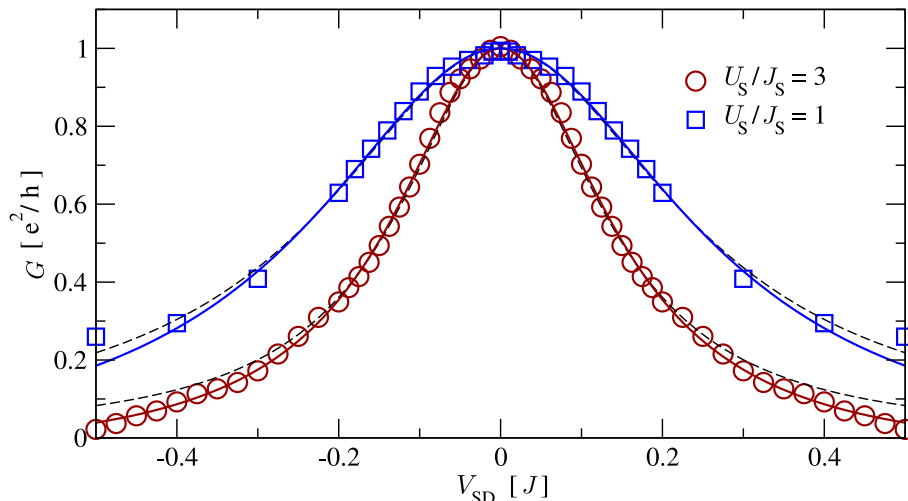
Figure 5.16 Differential conductance as a function of bias voltage through a 7 site nanostructure with nearest neighbour interaction. Parameters are $J_C = 0.5J$, $J_S = 0.8J$, and N/M=0.5. Squares (circles) denote weak (strong) interaction with $U_S/J_S = 1$ (3) (here: $U_C = 0.0$). Lines are fits to a Lorentzian with an energy-dependent self-energy $\Sigma = i\eta_0 + i\eta_1\mu^2$. Dashed lines: $\eta_1 = 0$. System size is $M = 144$ ($M = 192$) and 600 (800) states were kept in the DMRG.

proportional to the inverse of the width of the conductance resonance, $J/(2J_C^2)$, in agreement with the result in Ref. [114]. In general, extended structures with interactions will take longer to reach a quasi-stationary state, and the time evolution has to be carried out to correspondingly longer times.

In Fig. 5.16 we show results for the first differential conductance peak of an interacting $M_S = 7$-site nanostructure. Careful analysis of the data shows, that in order to reproduce the line shape accurately, one has to introduce an energy-dependent self-energy for $U_S/J_S = 3$. Since the effect is small, we approximate it by a correction quadratic in the bias voltage difference $\mu = V_{SD} - V_{peak}$. It is important to note that for the strongly interacting nanostructure, $U_S/J_S = 3$, the conductance peaks are very well separated. Therefore the line shape does not overlap with the neighbouring peaks, and the fit is very robust. Performing the same analysis for a non-interacting nanostructure with a comparable resonance width, we obtain negligible corrections to η_1 in the self-energy, indicating that the change of the line shape is due to correlation effects.

The linear conductance as a function of applied gate potential can be calculated in the same manner, if a sufficiently small external potential is used. We study the same 7-site nanostructure as before, with interaction $U_S = 0$, and use a bias voltage of $V_{SD} = 2 \cdot 10^{-4}J$. For half filled leads, the result for the linear conductance calculated with a fixed number of fermions, $N/M = 0.5$, is qualitatively correct, but the conductance peaks are shifted to higher energies relative to the expected peak positions at the energy levels of the non-interacting system (Fig. 5.17). Varying the gate
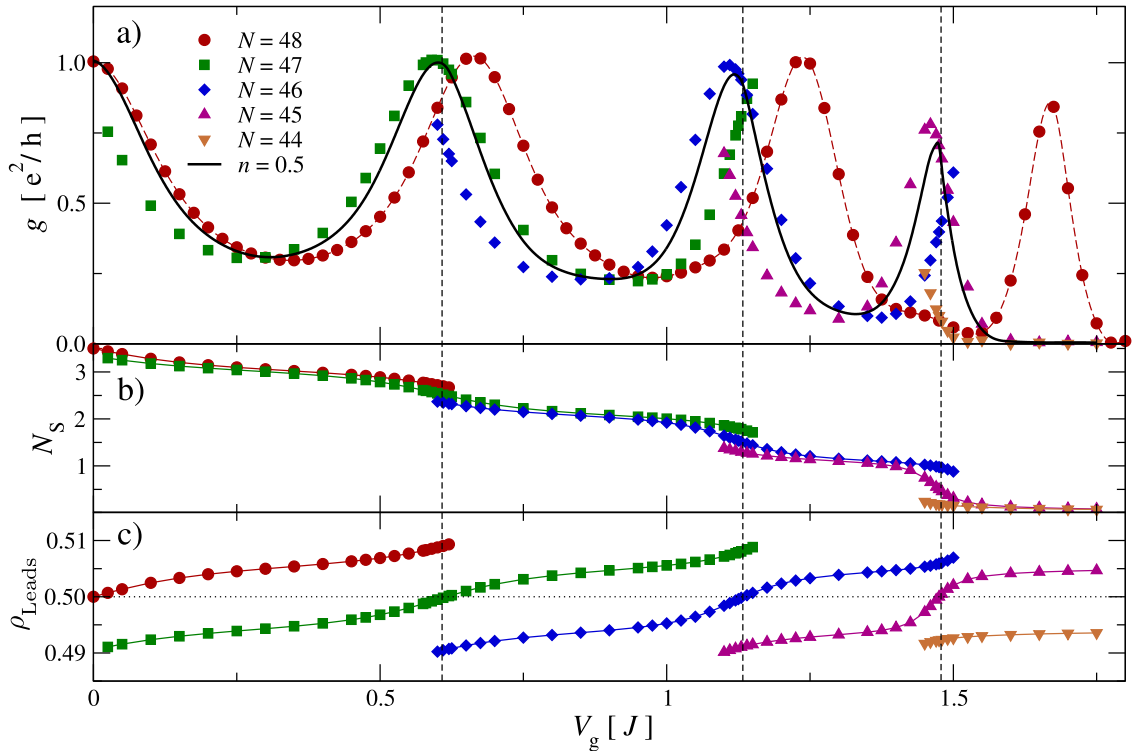
Figure 5.17 Transport through a non-interacting 7-site nanostructure with $J_C = 0.5J$ and $J_S = 0.8J$. The energy levels of the nanostructure are indicated by dashed vertical lines. (a) Linear conductance for different N. The result after applying finite size corrections is shown as straight line (see text for details). (b) Number of fermions on the 7-site nanostructure. (c) Density $\rho = (N - N_S)/(M - M_S)$ in the leads. The system size is $M = 96$ and the number of states kept in the DMRG is $N_{\text{cut}} = 400$.

potential V_g increases the charge on the nanostructure by unity whenever an energy level of the nanostructure moves through the Fermi level, cf. Fig. 5.17 (b). The density in the leads varies accordingly, cf. Fig. 5.17 (c). Since the number of fermions in the system is restricted to integer values, direct calculation of the linear conductance at constant particle density ρ *in the leads* is not possible and one must resort to interpolation. Using linear interpolation in $\rho(N, V_g)$ for $N = 44 \ldots 48$ yields our final result for the linear conductance at half filling, cf. Fig. 5.17 (a). The agreement in the peak positions is well within the expected accuracy for a 96 site calculation. Our results for the conductance through an interacting extended nanostructure are presented in Fig. 5.18. The calculation for the weakly interacting system requires roughly the same numerical effort as the non-interacting system. In the strongly interacting case, where the nanostructure is now in the charge density wave regime, the time to reach a quasi-stationary state is longer, and a correspondingly larger system size was used in the calculation. In both cases we obtain peak heights for the central and first conductance resonance to within 1% of the conductance for a
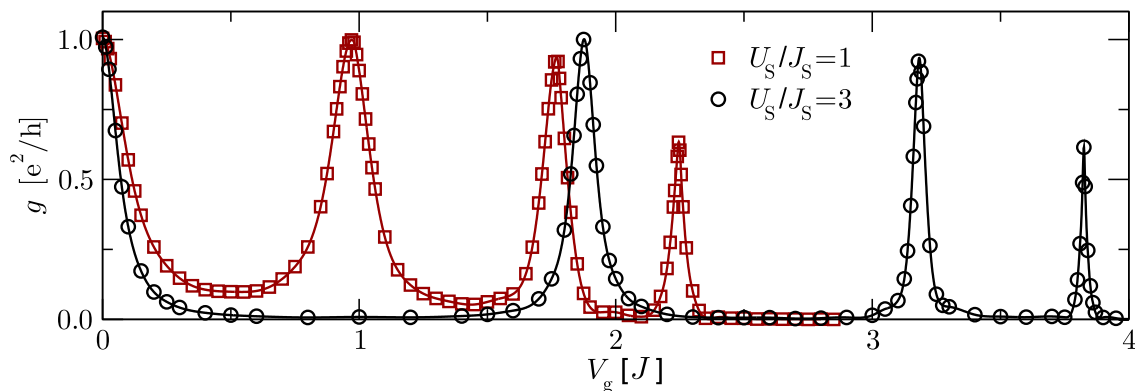
Figure 5.18 Linear conductance through an interacting 7 site system with $J_C = 0.5J$ and $J_S = 0.8J$ for weak (squares) and strong (circles) interaction. System size is $M = 96$ ($M = 192$) and 400 (600) states were kept in the DMRG. Finite size corrections have been included. Lines are guides to the eye.

single channel.

5.5 Exponential damping

In this section we study the effects and potential applications of damped boundary conditions (DBC). DBC have been introduced into DMRG calculations before, in order to reduce finite size effects [30, 59, 60, 88]. Here we would like to reduce the limitations arising from a finite transit time t_R and Josephson wiggling, which especially in the low voltage regime spoils the accuracy of current measurements. We have already seen how to exploit the voltage dependency of the finite size wiggling by using a fit procedure, which allows for the calculation of current-voltage characteristics even with an applied gate voltage. We now discuss the possibility of combining the fit procedure with DBC, where the damping effectively increases the system size. Furthermore we want to use DBC to adjust the single particle energy levels in order to increase the resolution with respect to V_{SD} when $V_g \neq 0$, cf. Fig. 5.14.

5.5.1 Estimate for Transit Time in a system with DBC at half filling

In Fig. 5.19 we show the time-dependent current through a single impurity with $V_g = 0$, for different values of the bias voltage V_{SD}, from the initial transient regime, until after the first finite size reflection. We compare two different system sizes with $M = 120$ and $M = 240$ lattice sites, and apply exponentially DBC in order to demonstrate the increased effective system size. The hopping matrix element is damped towards the boundaries of the system using a damping constant Λ as
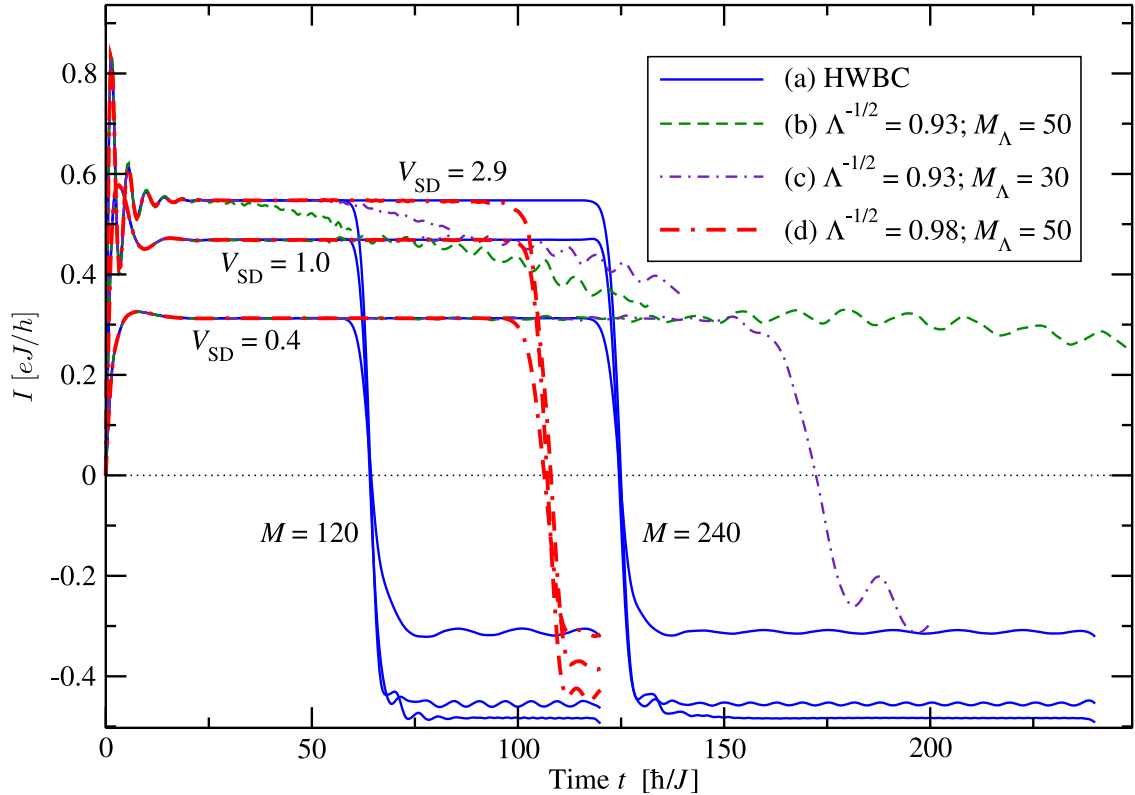
Figure 5.19 Time-dependent current through a single impurity with $J_C = 0.3J$, $V_g = U_C = 0$, at nominal half filling $N/M = 0.5$, obtained from exact numerical diagonalization for different bias voltages V_{SD} and different damping conditions. For small bias voltage, finite size reflections from hard wall boundary conditions (HWBC, a) can be suppressed significantly using damped boundary conditions (DBC). Using an exponential damping with $\Lambda^{-1/2} = 0.93$, $M = 120$ and $M_\Lambda = 50$ (b) yields a plateau of constant current for $V_{SD} = 0.4J$ considerably bigger than in the undamped case. However, with increasing bias voltage, the current plateau starts to decay before the estimated transit time according to Eq. (5.30) is reached (here: $t_R \approx 670$). Reducing the damping (c, d) can lead to good agreement with the estimate ($t_R(c) \approx 178$, $t_R(d) \approx 123$).

sketched in Fig. 2.4, over a range of M_Λ lattice sites. The total number of lattice sites is left unchanged (here: $M = 120, 240$). In most cases, we find an enhanced size of the current plateaus, however, under certain conditions, the damping can also lead to an early breakdown of the current.

An estimate for the transit time of a wave packet travelling in undamped leads of size M can be obtained from the Fermi velocity $v_F = 2J/\hbar$, which leads to

$$t_R \approx \frac{M}{v_F} = \frac{M\hbar}{2J}. \qquad (5.29)$$

Assuming a local Fermi velocity $v_F(x) = 2J(x)/\hbar$ in damped leads with damping
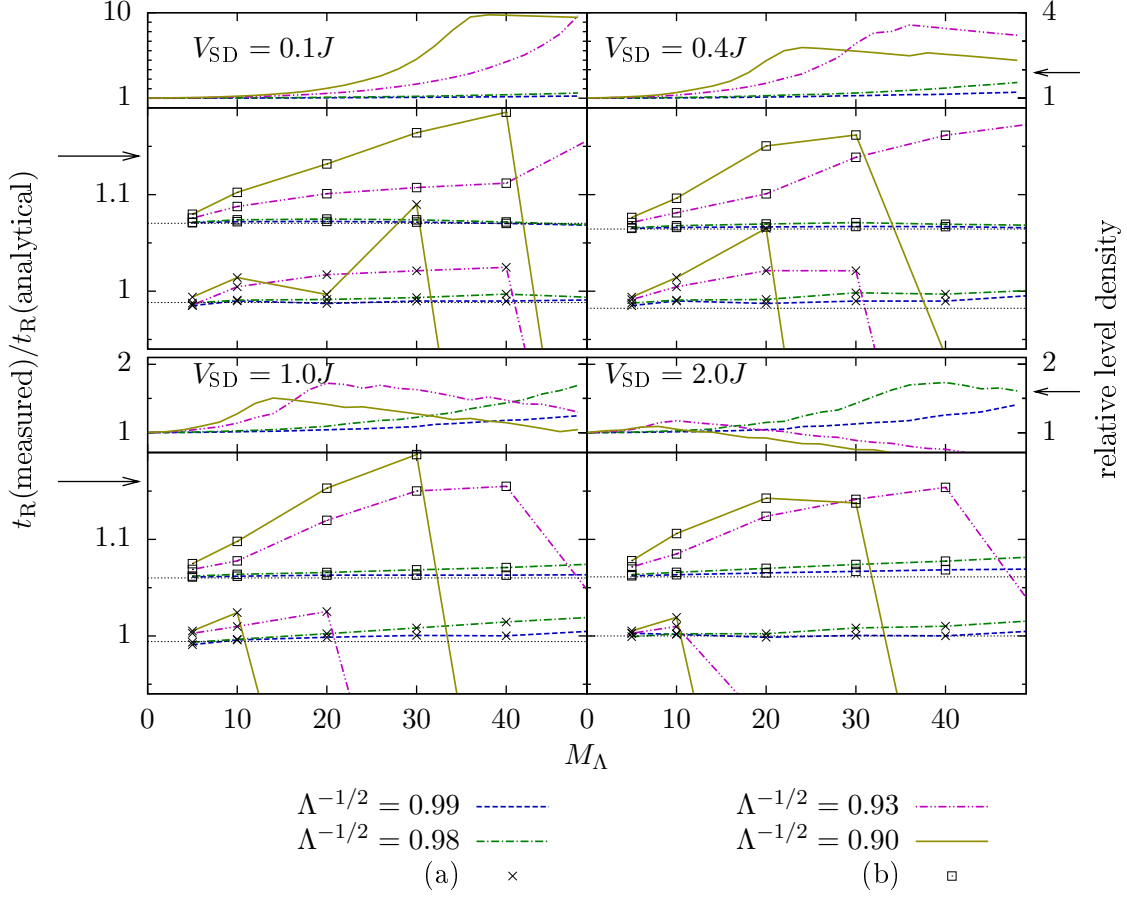
Figure 5.20   Test for the transit time estimate t_{R} of the current through a single impurity at half filling, Eqns. (5.29, 5.30), where the black dotted line is the undamped case. All values are plotted as functions of the damped lead size M_Λ. The top panels show the single particle level density for the energy given by the bias voltage, in units of the level density for the undamped case. (See text for details)

$\Lambda > 1$ leads to an expression of the form

$$t_{\mathrm{R}} \approx \frac{M\hbar}{2J}\left(1 - \frac{2M_\Lambda}{M}\right) + \frac{2\hbar}{J\ln\Lambda}\left(\Lambda^{M_\Lambda/2} - 1\right) \tag{5.30}$$

where M_Λ is the size of the damped leads. Eq. (5.30) can then be used to estimate an effective system size

$$M_{\mathrm{eff}} \approx M - 2M_\Lambda + \frac{4}{\ln\Lambda}\left(\Lambda^{M_\Lambda/2} - 1\right), \tag{5.31}$$

in agreement with the results for the pseudo-steady current found for the noninteracting case, Fig. 5.19. For a quantitative test of the expression for t_{R}, we compare the transit time, extracted from a current measurement, to the estimate given by

Figure 5.21
Level discretisation in a finite system ($M = 120$) with a single impurity, coupled to leads ($J_C = 0.3J$) as function of the damping rate $\Lambda^{-1/2}$ (a, b), as well as function of the size M_Λ of the damped leads (c). The damping lead size is set to (a) $M_\Lambda = 30$ and (b) $M_\Lambda = 50$, while for (c) the damping rate is set to $\Lambda^{-1/2} = 0.98$. The implementation of damped leads in combination with leads described by a uniform tight binding chain can be used to increase the level density in the vicinity of the Fermi edge while allowing for direct access to real space quantities like the current at a specific lattice site, as for example the impurity.
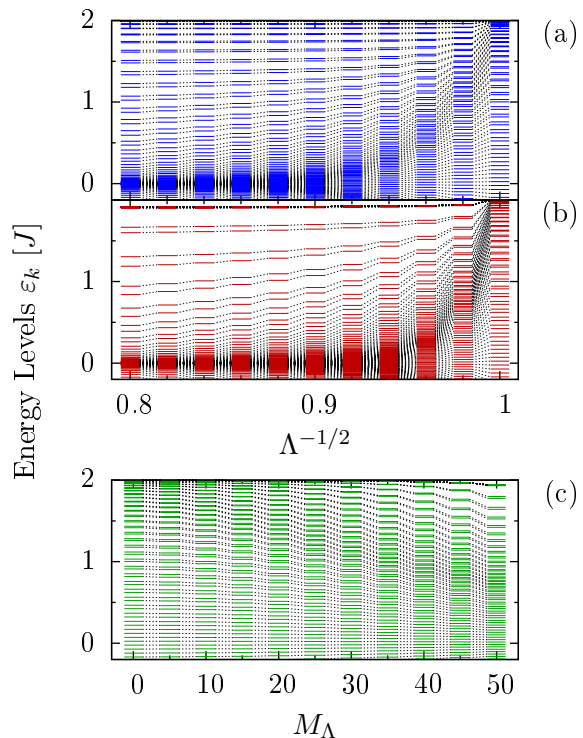
Eq. (5.30); cf. Fig. 5.20. We use two different criteria: (a) the time $t_R^{(a)}$ where $\dot{I}(t)$ becomes negative at the end of the first plateau (crosses), and (b) the time $t_R^{(b)}$ where the current changes sign after one round trip (squares). The black dotted lines show $t_R^{(a)}$ and $t_R^{(b)}$ for the undamped case. For values of $\Lambda^{-1/2}$ close to 1 we find good agreement between Eq. (5.30) and the simulations over a wide range of values of M_Λ for both conditions, (a) and (b), and even for large bias voltages. The growth of $t_R^{(a,b)}/t_R$ can be explained by different excitation velocities for $|V_{SD}| > 0$. However, the estimate becomes less accurate and even wrong for small bias voltages and small values of M_Λ, provided $\Lambda^{-1/2}$ becomes too small. For each case, the top panels show the relative single particle level density at energy $V_{SD}/2$. As can be expected, cf. Fig. 5.21, the level density grows with M_Λ until a maximum is reached. The position of the maximum is determined by the bias voltage. It can clearly be seen that, using condition (a), the position of the maximum, in combination with the values of $t_R^{(a)}/t_R$, gives a strong indication if a current plateau is still well defined for times on the order of the estimate of t_R, since $t_R^{(a)}/t_R \simeq 1$ for values of M_Λ on the left side of the maximum of the single particle level density. In comparison, condition (b) is a weak criterion, since for strong damping the current plateau starts decaying for times much shorter than t_R, cf. Fig. 5.19. In Fig. 5.21, we show the single particle energy levels of a system with $M = 120$ lattice sites with a single impurity, as function of the damping constant $\Lambda^{-1/2}$ and of the size of the damped leads M_Λ. The plot demonstrates the growth of the level density on the scale $\Lambda^{-M_\Lambda/2}$, which in conjunction with Fig. 5.20 allows for an estimate of the maximum value of V_{SD} up to which a current plateau can be expected in a system with DBC.

5.5.2 Fit Procedure

As already mentioned in Sec. 5.3, the fitting procedure becomes unreliable when the oscillation time t_J substantially exceeds the range $[t_S, t_R]$. We now demonstrate how to use the estimate for the transit time to implement damping conditions in order to sufficiently increase the effective system size, enforcing $t_J \simeq t_R - t_S$. As an example, we simulate the time evolution of a system with M lattice sites and a single, non-interacting impurity with $V_g = 0$, and apply a small bias voltage $V_{SD} > 0$. An
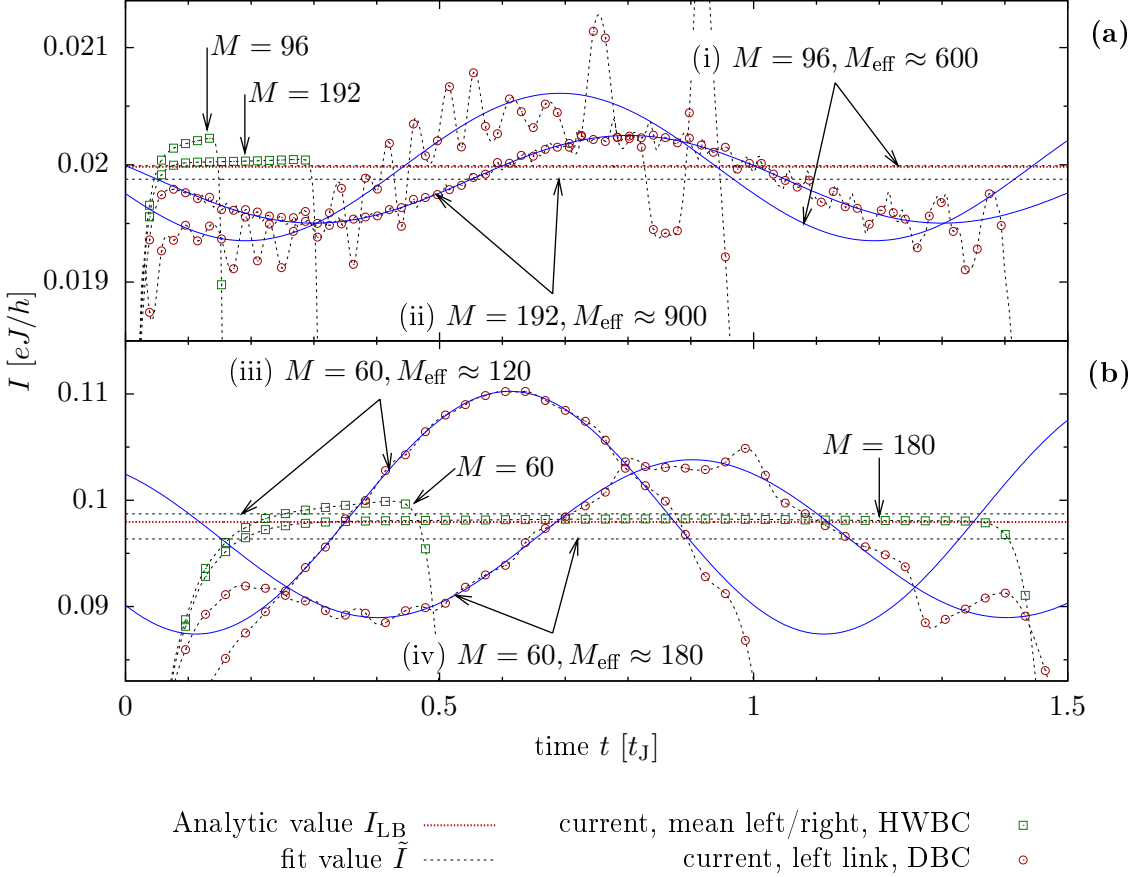
Figure 5.22 Current through a single impurity with $J_C = 0.3J$ and $V_g = U_C = 0$. The time axis is normalized to the oscillation period $t_J = 2\pi\hbar/V_{SD}$, with (a) $V_{SD} = 0.02J$ and (b) $V_{SD} = 0.1J$. For $V_{SD} = 0.02J$ (a), the oscillation period is $t_J = 314\hbar/J$. To obtain a current plateau containing at least one Josephson oscillation one has to simulate the time evolution of a system with $M \gtrsim 630$, which is very difficult on present days computers when interaction is included. Here, we apply DBC on a system with $M = 96$ ($M = 192$) to effectively increase the system size using (i) $\Lambda \approx 0.903$, $M_\Lambda = 32$ (ii, $\Lambda \approx 0.969$, $M_\Lambda = 84$). Accidentally, the fit value agrees with the analytic value nearly perfectly for configuration (i). For $V_{SD} = 0.1J$ (b), $t_J = 63\hbar/J \Rightarrow M \gtrsim 126$. The damping conditions are characterized by (iii) $\Lambda \approx 0.93$, $M_\Lambda = 20$ and (iv) $\Lambda \approx 0.900, M_\Lambda = 20$, respectively.

effective transit time $t_{\mathrm{R}}^{\mathrm{eff}} \approx t_{\mathrm{J}}$ can be obtained using DBC, according to Eqns. (5.30, 5.31).

The result is presented in Fig. 5.22, where we show the time-dependent current through one of the contact links of a single impurity for different damping conditions and two different values of V_{SD}. Again, we fit $\tilde{I} + \tilde{I}_{\mathrm{J}} \cos(V_{\mathrm{SD}} t / \hbar + \tilde{\varphi})$ to the oscillating part of the current expectation value. The extracted current $\tilde{I}$ for the calculations including DBC agrees with the analytic result within $\sim 1\%$, which is of the same order of magnitude as the mean value extracted from the very small plateau regime that can be found for the system with hard wall boundary conditions. We conclude that DBC can be used to obtain a first guess, but for high precision measurements, hard wall boundary conditions together with an increased system size have to be used, c.f. $M = 180$ in Fig. 5.22(b). The failure of DBC for short leads can also be understood as an inverse tsunami effect, compare [87]. Due to the exponentially reduced hopping elements the leads fail to provide a structureless bath of particles.

5.5.3 Correction of the single particle energy levels using DBC

In Section 5.3.2 we found that the effects resulting from a finite density shift in the leads when applying a gate voltage can be significantly suppressed when extracting the current only for certain values of V_{SD} determined by the single particle level spacing. Since these finite size effects particularly arise in the middle of the band where the density of single particle levels is the lowest – and where the current has to be extracted for the calculation of the linear conductance – one would like to somehow shift the single particle levels towards the center of the band. This can be achieved by increasing the number of lattice sites, but at the same time also increases the numerical effort.

Applying DBC also results in a shift of the single particle energy levels in the leads towards the center of the band, cf. Fig. 5.21. We therefore ask the question if the criterion for the relation of bias voltage and single particle energy levels formulated in Sec. 5.3.2 still holds for DBC. The result is shown in Fig. 5.14 (data set (b), pluses). To obtain the additional data points (b), we used damping conditions with values of $\Lambda^{-1/2} = 0.91 \ldots 0.98$ and $M_\Lambda = 15, 20, 23$. We calculated the single particle energy levels for the decoupled leads and obtained the current for values of the bias voltage with $V_{\mathrm{SD}}/2$ in the middle of two neighbouring energy levels. To increase the resolution for the high voltage regime only moderate damping conditions are required ($\Lambda^{-1/2} = 0.98$, $M_\Lambda = 15, 20$), while strong damping is required to achieve high resolution in the low voltage regime. For V_{SD} approaching the band edge, however, DBC have to be avoided for the reasons discussed earlier.

5.6 Shot Noise in the Resonant Level Model

It seems reasonable to expect that time-dependent DMRG can also be used to determine current fluctuations, which could also, in some setups, be determined analytically [117]. In order to reach this goal, it is crucial to be able to extract cumulants – in particular the shot noise – from real time simulation methods. In this section we discuss a method to do this, including results for the IRLM.

The main problem in the determination of noise is the finite size analysis of the results of non-equilibrium correlation functions for finite systems. To concentrate on this aspect, we first discuss results for the non-interacting resonant level model (RLM) where the numerical data can be obtained using exact diagonalisation (ED) techniques [84]; cf. also section 3.1. Since in this specific case there are straightforward analytical solutions of the problem, we can check the reliability of our approach in great detail. As a main result of this work we then proceed to present results for shot noise in the IRLM with finite interaction, at the self-dual point of the model, where we can compare to analytic results based on the thermodynamic Bethe ansatz [85]. To show the general applicability and the limitations of the scheme, we also include results for other values of the interaction.

We note that prior to our work, a numerical study of the full counting statistics for another non-interacting model appeared in [100]. The method used there is however tailored to the free case and uses intermediate analytical results from [77]. Our approach, in contrast, is based directly on the 'experimentally' measured time-dependent correlation of the current. It is also not specific to fermionic systems and may be applied to the study of light-matter interaction in wave-guiding structures [118].

To make things concrete, we start by giving the Hamiltonian of our test system. For the thermodynamic limit, it is equivalent to Eq. (2.15). Of course, for the numerical simulation, we have to restrict the overall system size to a finite number of lattice sites $M = M_{\mathrm{L}} + M_{\mathrm{R}} + 1$ again, corresponding to the nomenclature of Eqns. (5.1-5.4), where we now place the impurity in the center of the system. In the remainder of this section we concentrate on the resonant case at zero gate voltage $V_{\mathrm{g}} = 0$ and half filling. We then arrive at

$$\hat{H}_{\mathrm{C}} = \sum_{x=0,1} \Big[- J_{\mathrm{C}}(\hat{c}^{\dagger}_{M_{\mathrm{L}}-1+x}\hat{c}_{M_{\mathrm{L}}+x} + \hat{c}^{\dagger}_{M_{\mathrm{L}}+x}\hat{c}_{M_{\mathrm{L}}-1+x})$$
$$+ U_{\mathrm{C}}(\hat{n}_{M_{\mathrm{L}}-1+x} - \frac{1}{2})(\hat{n}_{M_{\mathrm{L}}+x} - \frac{1}{2}) \Big], \tag{5.32}$$

$$\hat{H}_{\mathrm{L}} = -J \sum_{x=0}^{M_{\mathrm{L}}-2} (\hat{c}^{\dagger}_{x}\hat{c}_{x+1} + \hat{c}^{\dagger}_{x+1}\hat{c}_{x}), \quad \hat{H}_{\mathrm{R}} = -J\sum_{x=M_{\mathrm{L}}+1}^{M-2}(\hat{c}^{\dagger}_{x}\hat{c}_{x+1} + \hat{c}^{\dagger}_{x+1}\hat{c}_{x}), \tag{5.33}$$

$$\hat{H} \equiv \hat{H}^{\mathrm{finite}}_{\mathrm{IRLM}} = \hat{H}_{\mathrm{L}} + \hat{H}_{\mathrm{C}} + \hat{H}_{\mathrm{R}}. \tag{5.34}$$

Shot noise is the contribution to current fluctuations at zero temperature – and hence a pure charge discretisation effect. To prepare the system in a state with finite

current through the structure, we therefore use the recipe described in section 5.1, adding a charge imbalance operator $\hat{H}_{SD} = V_{SD}[\hat{N}_L - \hat{N}_R]/2$ to the Hamiltonian and calculating the initial state as the ground state $|\Psi(t=0)\rangle = |\Psi_0\rangle$ of $\hat{H} + \hat{H}_{SD}$. Here, $\hat{N}_L$ ($\hat{N}_R$) counts the particle number in the left (right) lead. We then perform the time evolution using the time evolution operator $\hat{U}(t) = \exp(-i\hat{H}t/\hbar)$.

5.6.1 Numerical computation of current fluctuations

The following discussion is based on the numerical computation of time-dependent current fluctuations as defined in Eq. (5.10),

$$S(t, t') = \text{Re}\langle \Delta\hat{I}(t)\Delta\hat{I}(t')\rangle = \text{Re}\langle\Psi_0|\Delta\hat{I}(t)\Delta\hat{I}(t')|\Psi_0\rangle. \tag{5.35}$$

For strongly correlated systems, we use the time-dependent DMRG to perform the time evolution. Similar to the discussion in section 5.1.1, we have to obtain the time evolution of the initial non-equilibrium state $|\Psi_0\rangle$, for a set of time steps $t = n\Delta t$, $n \in \mathbb{N}$, and $t' = n'\Delta t$, $n' \in \mathbb{N}$, based on the Krylov subspace method; cf. section 3.3. The evaluation of expressions of the form $\langle \Delta\hat{I}(t)\Delta\hat{I}(t')\rangle = \langle\Psi_0|\Delta\hat{I}(t)\Delta\hat{I}(t')|\Psi_0\rangle$ then amounts to the computation of states

$$|\Psi(t')\rangle = U(t')|\Psi_0\rangle, \quad |\Psi(t)\rangle = U(t-t')|\Psi(t')\rangle, \tag{5.36}$$

$$|\Psi_I(t')\rangle = \Delta\hat{I}|\Psi(t')\rangle = \left[\hat{I} - \langle\Psi(t')|\,\hat{I}\,|\Psi(t')\rangle\right]|\Psi(t')\rangle, \quad \text{the same for } |\Psi_I(t)\rangle, \tag{5.37}$$

$$|\Phi_I(t' \to t)\rangle = U(t-t')|\Psi_I(t')\rangle, \tag{5.38}$$

$$\Rightarrow \quad \langle \Delta\hat{I}(t)\Delta\hat{I}(t')\rangle = \langle\Psi_I(t)|\Phi_I(t' \to t)\rangle. \tag{5.39}$$

For details of the DMRG time evolution protocol and the use of Krylov subspace methods for the time evolution operator see sections 3.2, 3.3 and Ref. [47].

Again, in the noninteracting case with $U_C \equiv 0$, we can apply the single-particle decomposition method as described in section 3.1; cf. also section 5.1.1. The Hamiltonian of the IRLM, Eqns. (5.32-5.34), can be expressed by a square form as in Eq. (3.2), which allows evaluation of the time-dependent current-current correlations (5.35) by means of Eq. (3.12).

5.6.2 Finite size effects study in the non-interacting case

Since we want to compare the numerical data with analytical results, we restrict ourselves to the non-interacting case with $U_C = 0$ for the moment. The expectation value of $\hat{I}(t)$, measured symmetrically on both contact links (cf. Eq. (5.8)), in the RLM for $J_C = 0.4J$ and for some values of V_{SD} is shown in the upper part of Fig. 5.23, while in the lower part, the current-current correlation function $S(t, t_{\min})$ can be found, for $t > t_{\min}$, and for a certain value of $t_{\min}$. Effects like the finite settling time t_S and the finite transit time t_R as well as the I-V_{SD}-characteristics have been already discussed in this chapter in great detail.
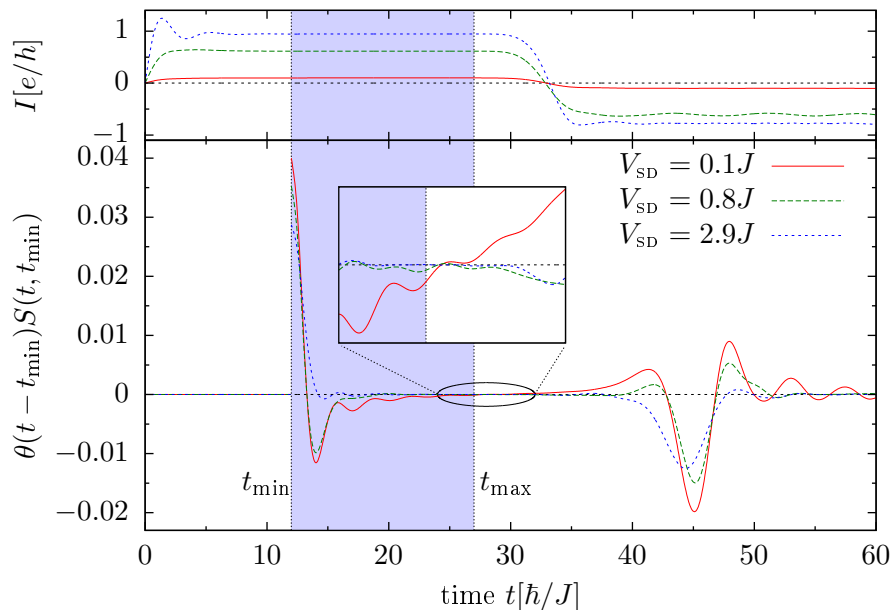
Figure 5.23 Time-dependent current $I(t)$, and current correlation function $S(t, t_{\min})$ with $t_{\min} = 12$, in the non-interacting resonant level model RLM, with tight-binding leads and a finite system size of $M = 60$ lattice sites, for different values of the bias voltage V_{SD}. The $I(t)$ curves show the three time regimes given by the settling time t_{S} and the transit time t_{R}. The highlighted time domain indicates the integration range $[t_{\min}, t_{\max}]$. The inset demonstrates an additional subtlety: the correlation function shows finite size reflection effects on the time scale $t - t_{\min} \gtrsim t_{\mathrm{R}}/2$, which imposes an additional restriction on $t_{\max}$.

At the beginning of this chapter we defined the noise power spectrum as the Fourier transform of the time-dependent current fluctuations, cf. Eqns. (5.9-5.15). We now want to see whether the noise can be reliably obtained in a real-time simulation based on these formulas. There are of course many obstacles. The first comes from the calculation of a non-equilibrium correlation function in the time domain from a real-time simulation. Because we are restricted to a finite system with M lattice sites and hard walls, a steady transport state is not well defined. Instead, we make the attempt to calculate the time evolution from the initial non-equilibrium state $|\Psi(t = 0)\rangle$ as described before and look for a quasi-stationary time regime. The "switching on" of a finite source-drain voltage V_{SD} at the initial time causes a ringing of the current [114], cf. also Fig. 5.23, which decays exponentially within a settling time t_{S}. The current finally enters a plateau regime, where the size of the plateau is given by the transit time t_{R} which is finite due to the finite size of the system [67], Fig. 5.23.

Having performed the time evolution of the system in order to bring it "close" to a steady state, we now have to evaluate the integral (5.15) in a limited time range

in order to obtain the low-frequency limit of the noise power spectrum

$$S_{\text{num}} = 4 \int\limits_{t_{\min}}^{t_{\max}} dt \ \text{Re}\langle \Psi_0 | \Delta \hat{I}(t) \Delta \hat{I}(t_{\min}) | \Psi_0 \rangle \tag{5.40}$$

where $t_{\min} > t_{\text{S}}$ and $t_{\max} < t_{\text{R}}$. Note, that $t_{\max}$ has to be chosen carefully, since finite size effects for the current-current correlations already occur on the time scale $t - t_{\min} \geq t_{\text{R}}/2$; cf. also the inset of Fig. 5.23. The symmetric definition of $S(t, t_{\min}) = S(t_{\min}, t)$, cf. Eq. (5.9), allows us to skip the integration over the time-range $t < t_{\min}$, which enables us to put $t_{\min}$ to the early period of constant current. In a hypothetical situation with a system of infinite size where $t_{\text{R}} \to \infty$ the contribution of

$$\int\limits_{t_{\max}}^{\infty} dt \ \text{Re}\langle \Psi_0 | \Delta \hat{I}(t) \Delta \hat{I}(t_{\min}) | \Psi_0 \rangle$$

can be neglected if $\text{Re}\langle \Delta \hat{I}(t) \Delta \hat{I}(t_{\min}) \rangle$ is small for $t > t_{\max}$ as compared to the mean value in the range $t_{\min} < t < t_{\max}$. One therefore has to choose the size of the system to be big enough to ensure the correlation function drops to zero within the transit time. This seems to be the case for the example given in Fig. 5.23, at least for values of the bias voltage $V_{\text{SD}} \gtrsim J$.

The finite transit time t_{R} introduces a finite cutoff frequency

$$\omega_{\text{cut}} = 2\pi/t_{\text{R}} \propto 1/M. \tag{5.41}$$

This is the main problem we encounter. In contrast to the situation of infinite leads, where zero frequency noise vanishes without applied voltage, we now find a contribution to the zero voltage shot noise of the order of $S(\omega_{\text{cut}})$. The low frequency domain is the most interesting for the kind of problems we wish to study: low frequency is low energy and thus strong coupling between impurity and leads.

The magnitude of the finite size effects for the type of systems that can be studied on the basis of the numerical computation resources available today is far from negligible. On Fig. 5.24 we give results for the shot noise S_{num} obtained for different system sizes of M lattice sites, as well as the expected result S in the thermodynamic limit obtained from the Landauer–Büttiker approach (this is discussed in more details in the appendix). While the results measured for finite size and the asymptotic results agree at large voltages, there is a marked difference at small voltages, with an offset at vanishing V_{SD}. In the figure, we also represent the finite size correction

$$\Delta S_{\text{num}} = S_{\text{num}} - S \tag{5.42}$$

rescaled by the system size M. For different values of M the rescaled finite size corrections $M \times \Delta S_{\text{num}}$ collapse very well on a single curve, indicating that the main finite size effects scale linearly with $1/M$ in the considered parameter regime. One
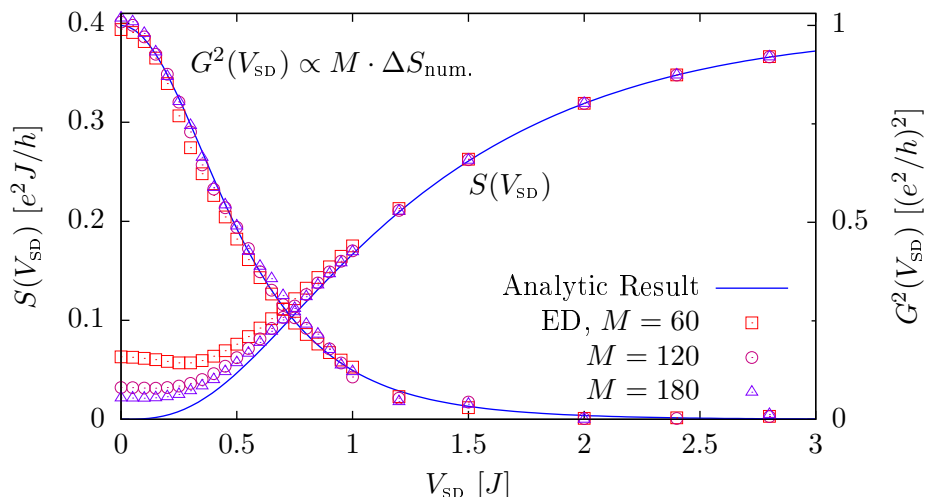
Figure 5.24 Noise S and squared differential conductance G^2 for $J_C = 0.4J$. The blue lines represent the analytic values obtained using the Landauer–Büttiker approach. The finite size of the system introduces an additional noise proportional to G^2/M.

may expect that the cut off given by the finite size of the leads corresponds to an effective finite temperature $\sim M^{-1}$ resulting in a low voltage offset $\sim G/M$. However, we find $\Delta S_{\mathrm{num}} \propto G^2$ with the differential conductance $G(V_{\mathrm{SD}}) = \partial I(V_{\mathrm{SD}})/\partial V_{\mathrm{SD}}$.

To understand the behaviour of ΔS_{num}, we consider the full frequency dependence of the shot noise. It can be obtained analytically in the wide band limit – see the appendix, Eq. (B.24). For values of $J_C/J \ll 1$, the numerical results obtained for the model with cosine dispersion relation should be consistent with the analytical result as long as the considered frequency is small compared to the band width. This is illustrated in Fig. 5.25. There, the frequency-dependent noise is obtained via

$$S_{\mathrm{num}}(\omega) = 4\mathrm{Re} \int_{t_{\mathrm{min}}}^{t_{\mathrm{max}}} \mathrm{d}t \ e^{i\omega(t-t_{\mathrm{min}})} S(t, t_{\mathrm{min}}) \tag{5.43}$$

for different values of the bias voltage V_{SD}. For big values of ω, the effects of the band curvature are quite marked – as can be seen by the departure of the various guide lines from the dotted lines representing the analytic wide band limit results.

To understand the voltage dependency of the finite size corrections, we consider the low frequency behaviour of the analytical results in the wide band limit

$$S(\omega > 0, V_{\mathrm{SD}}) = S(0, V_{\mathrm{SD}}) + \Delta S(\omega, V_{\mathrm{SD}}) + \mathcal{O}(\omega^2) \tag{5.44}$$

with the correction[2] in first order with respect to ω

$$\Delta S(\omega, V_{\mathrm{SD}}) \propto G^2(V_{\mathrm{SD}})\omega. \tag{5.45}$$

---

[2]The low-frequency approximation, including the first order in ω, has been provided by E. Boulat and H. Saleur; cf. also Ref. [84].
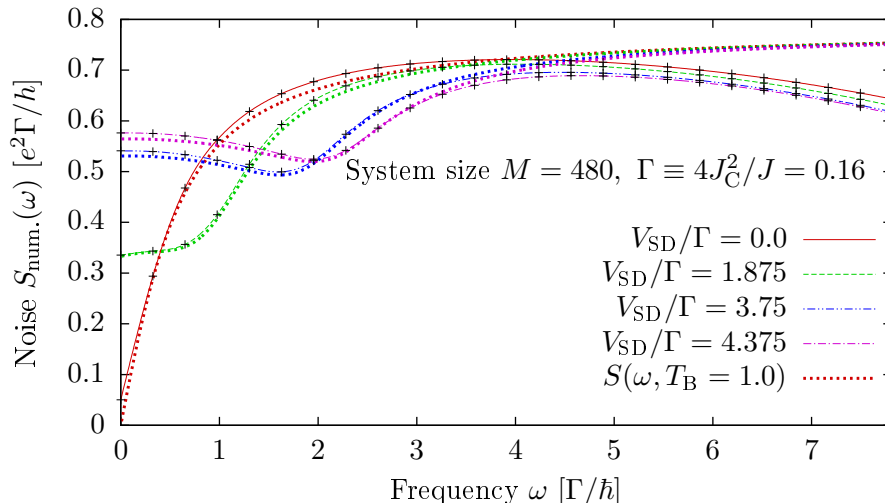
Figure 5.25 Noise $S(\omega)$ vs. frequency ω, both rescaled with respect to the width of the conductance peak $\Gamma = 4J_C^2/J$, for different values of the bias voltage. The lines going through the numerical values (represented by crosses) are just guides for the eye. The dotted lines correspond to the analytical result for the wide band limit.

For the system with finite band width, we have checked this expression by extracting the slope $\partial S(\omega, V_{SD})/\partial\omega$ in the limit $\omega \to 0^+$ from the numerical data. Again we find good agreement with G^2 in a voltage regime where finite size effects can be neglected, Fig. 5.26.

Inserting the cutoff frequency now leads to the expression

$$\Delta S(\omega_{cut}, V_{SD}) \propto \frac{1}{M} G^2(V_{SD}) \tag{5.46}$$

which is in good agreement with $\Delta S_{num}(V_{SD})$, cf. Fig. 5.24.

Using our knowledge of the finite size correction, we can now control the extrapolation of numerical data: in Fig. 5.28 we show the results obtained using linear extrapolation $1/M \to 0$ for $J_C = 0.3J$ and $J_C = 0.4J$. We find indeed very good agreement with the analytical result.

Damped boundary conditions The non-interacting case is of course very simple to calculate numerically (regardless of the possibility of the Landauer–Büttiker treatment). The numerical main effort consists in the exact diagonalisation of the $M \times M$ Hamiltonian matrices as well as the calculation of the time evolution which involves the multiplication of $M \times M$ matrices. Including interaction spoils this approach. Instead, one has to resort to approximative time evolution schemes using methods for correlated electrons – in the next section we will do so based on the time-dependent DMRG. While for the ED-based approach in the context of a non-interacting system it is no problem to obtain numerical results for $M \sim 1000$ lattice sites, the DMRG based approach is limited to the simulation of systems with
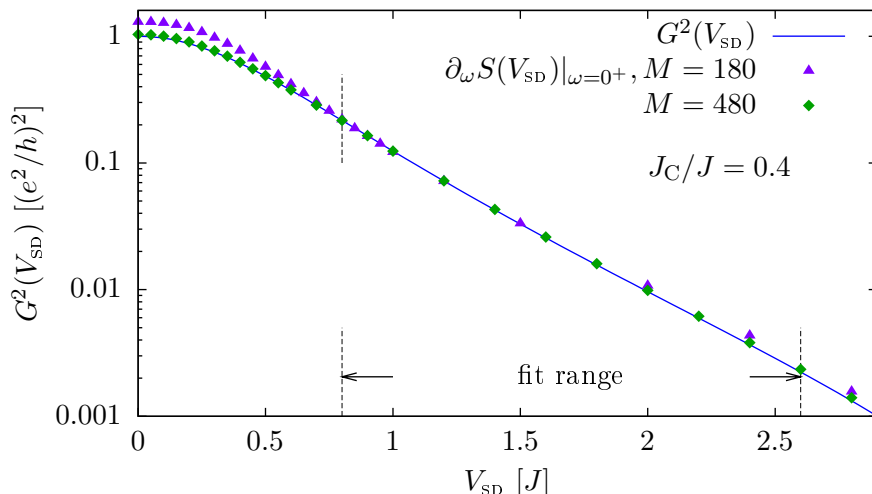
Figure 5.26 Slope of the frequency-dependent shot noise in the limit $\omega \to 0^+$, rescaled to fit with G^2, for different system sizes. In the low voltage regime we find finite size effects.

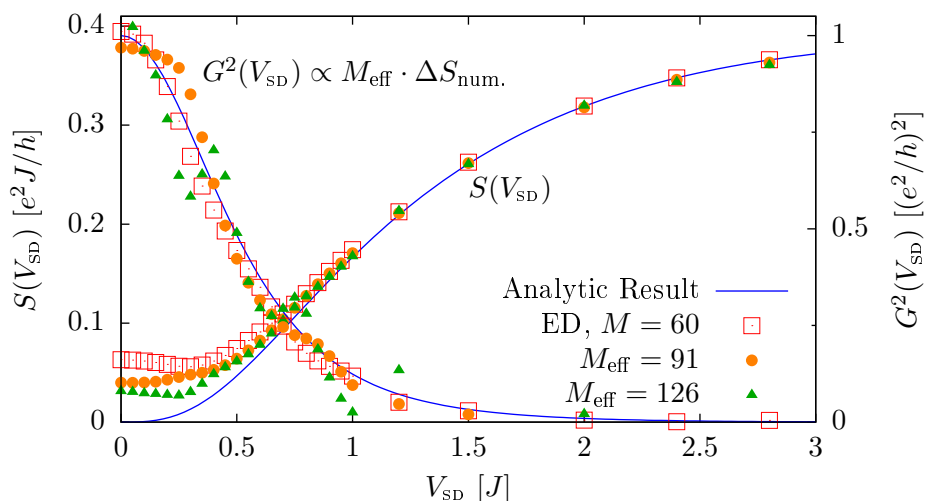*Figure 5.27* Noise S and squared differential conductance G^2 for $J_{\mathrm{C}} = 0.4J$. The blue lines represent the analytic values obtained using the Landauer–Büttiker approach. The system size is fixed to $M = 60$ lattice sites, while at the boundaries, the hopping matrix elements are exponentially damped with the damping constant $\Lambda^{-1/2}$ on M_Λ links. This results in an effectively enlarged system with M_{eff} lattice sites. The finite size correction ΔS_{num}, here rescaled by M_{eff}, again collapses on a single curve for different M_{eff}, and is still proportional to G^2.

$M \sim 50 \ldots 100$ lattice sites. Wilson leads, or damped boundary conditions (DBC), increase the energy resolution close to the Fermi surface and allow for a high resolution in linear transport calculations, see [30, 31]. In section 5.5 (cf. also Ref. [67])

we showed that using DBC with a weak damping constant allows us to effectively increase the system size to $M_{\text{eff}} > M$ lattice sites without changing M, where a rough estimate for M_{eff} has been given as a function of the damping constant Λ and the length of the damped leads M_Λ

$$M_{\text{eff}} \approx M - 2M_\Lambda + \frac{4}{\ln \Lambda} \big(\Lambda^{M_\Lambda/2} - 1 \big). \qquad (5.47)$$

We now use this estimate to perform the linear extrapolation to infinite system size, where we additionally adjust the estimate by fixing the extrapolated value to analytic results (cf. Ref. [119], for example, or section B.3 in the appendix)

$$S(V_{\text{SD}} = 0) = 0. \qquad (5.48)$$

To verify this approach we performed calculations for a non-interacting system with $M = 60$ lattice sites and DBC, for $J_{\text{C}} = 0.4J$. For the damped leads we used different combinations of Λ and M_Λ, where we used values for the damping constant in the range $\Lambda^{-1/2} \in [0.93, 1.0]$ for damped leads of $M_\Lambda = 0 \dots 26$ lattice sites (while keeping the total number of lattice sites M fixed!). The estimate for the effective system size, Eq. (5.47), is checked by looking at the scaling behaviour of the finite size correction ΔS_{num}, where we now find linear scaling $\propto 1/M_{\text{eff}}$, cf. Fig. 5.27.

The result is shown in Fig. 5.28. We find remarkably good agreement with the analytical result, while we have to point out that, for values of the bias voltage in the order of the band width, the approach fails, which has to be expected since the estimate of the system size only works in a limited voltage range, compare section 5.5. Additionally we find the numerical data to be very noisy depending on the respective configuration of the damping conditions.

The concept is not restricted to non-interacting fermions and can be implemented using numerical methods for interacting quantum systems. In this case as well, we expect the finite size corrections to go as $1/M$ because the cutoff frequency ω_{cut} has the same dependence. We note however that the prefactor might not be $G^2(V_{\text{SD}})$ exactly. [120, 121]

5.6.3 Finite interaction: the self-dual point of the IRLM

In the preceeding section we studied the influence of the finite size of the model system on the low-frequency shot noise of the current through the nanostructure. Since we made the assumption that electron-electron interaction can be suppressed on the structure, $U_{\text{C}} \equiv 0$, we have been able to apply a single-particle decomposition approach and to handle the numerical simulation by means of exact diagonalisation. We now want to apply the approach to the interacting resonant level model (IRLM), with finite interaction $U_{\text{C}} > 0$. The computation of the time-dependent current-current correlation therefore now is based on the time-dependent DMRG [47], as described in section 5.6.1.

Here, we set $U_{\mathrm{C}} = 2.0J$, and the coupling to $J_{\mathrm{C}} = 0.4J$, while we still operate in the resonant tunneling regime $V_{\mathrm{g}} = 0$. The IRLM bears a duality symmetry exchanging large and small interactions U_{C}. For an intermediate value of U_{C} the model is self-dual, which in our description exactly corresponds to the value $U_{\mathrm{C}} = 2.0J$ [56, 85]. Furthermore, there is an exact analytic solution to the problem for precisely the self-dual point, in the wide-band limit, which again allows us to check the numerical data; cf. also appendix B.2.

The total number of lattice sites in the numerical calculation varies from $M = 48$ to 72 lattice sites, with $M_{\mathrm{R}} = M_{\mathrm{L}} + 1$. Different other setups have been considered, including the effective enlargement of the system using damped boundary conditions as discussed before, which will not be presented here. For the numerical simulation within the DMRG projection scheme we set an upper bound to the dimension of the Hilbert space for each DMRG block to $N_{\mathrm{cut}} = 4000$ states.

As a first result we compare the numerical data for different system sizes to the analytical result in Fig. 5.29, where we show zero-frequency shot noise as well as the finite size error of the numerical data, rescaled by the system size. As discussed in the preceeding section, in the low frequency limit, strong finite size effects have to be expected, that get mostly pronounced for small values of the voltage. Since the rescaled finite size error happens to collapse on a single curve in the low voltage
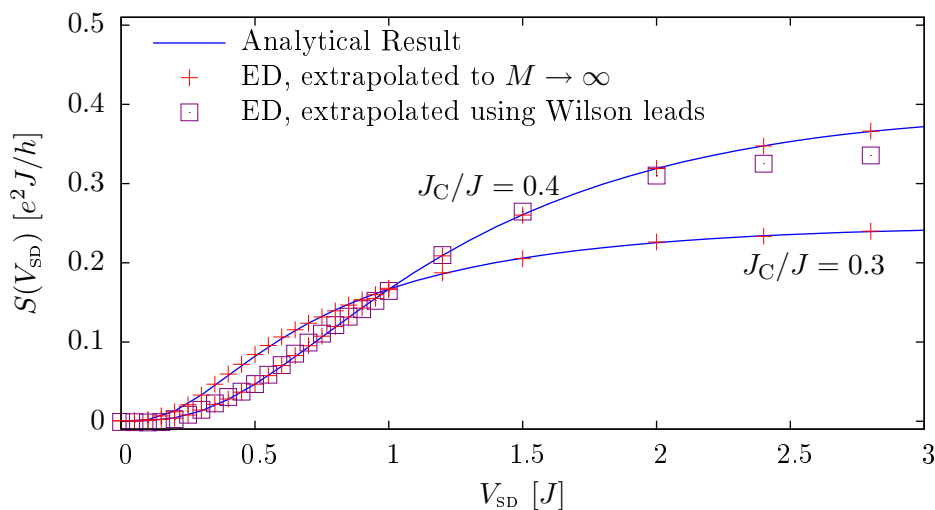
Figure 5.28   Shot Noise S as function of the bias voltage V_{SD} in the non-interacting resonant level model. The analytical result was obtained using the Landauer–Büttiker approach, Eq. (B.10) in the appendix, while the numerical result is computed for systems of different finite sizes of $M = 120...180$ lattice sites with a subsequent linear extrapolation of $1/M \to 0$. The two curves correspond to different couplings J_{C} of the impurity to the leads. Furthermore, we used DBC in order to effectively increase the system size. Here, the system size was fixed to $M = 60$ lattice sites. For weak damping and for not too big values of V_{SD}, we find very good agreement with the undamped case.

regime, the numerical data can be linearly extrapolated to infinite system size in order to obtain results for the thermodynamic limit. Also we verify the analytical estimate for the finite size error $S_{\text{num.}} - S_{\text{analyt.}} \propto G^2/M$ with G the differential conductance; cf. appendix B.2 for an analytic expression for G in the self-dual IRLM. The strong deviations in the high voltage regime from this relation may be traced back to different sources: the cutoff error introduced by the approximative time-dependent DMRG scheme gets especially pronounced for values of the voltage of the order of the bandwidth. Furthermore, to keep the numerical simulation feasible, one has to resort to small systems introducing finite size effects beyond the linear scaling.

Nevertheless, the numerical results shown in Fig. 5.30, where we obtained data for the low voltage regime using linear extrapolation, show very nice agreement with the analytical results given by Eq. (B.22) in the appendix.

The back-scattering Fano factor for the back-scattering current I_{BS},

$$F_{\text{BS}}(V_{\text{SD}}) = \frac{S(V_{\text{SD}})}{I_{\text{BS}}(V_{\text{SD}})}, \quad I_{\text{BS}}(V_{\text{SD}}) = gV_{\text{SD}}/e - I(V_{\text{SD}}), \tag{5.49}$$

with the *linear* conductance g ($g = e^2/h$ in the resonant tunneling situation), can also be obtained from the numerical data, Fig. 5.31, where we use the analytical
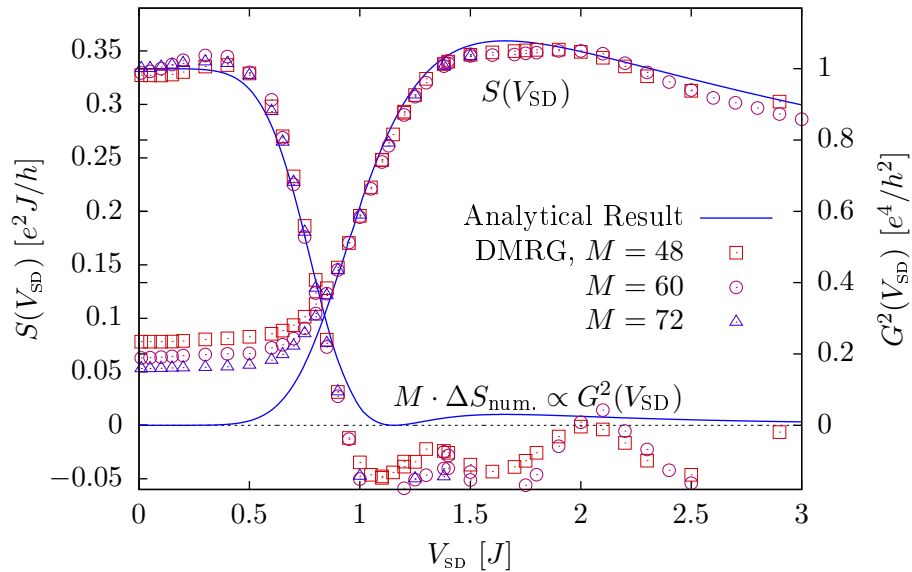
Figure 5.29 Finite size error of noise. The blue lines represent the analytical result, cf. appendix B.2. The numerical data have been obtained for systems with coupling $J_{\text{C}} = 0.4J$ and density-density interaction $U_{\text{C}} = 2.0J$ using td-DMRG. The system size varies from $M = 48$ to $M = 72$ lattice sites. The difference of numerical and analytical data in the low voltage regime is proportional to the squared differential conductance G^2 and scales linearly with the inverse system size $1/M$.
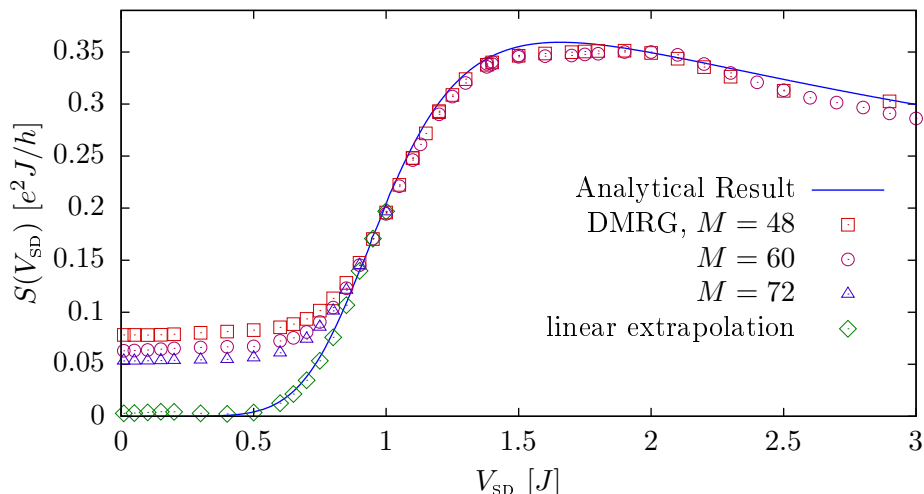
Figure 5.30 Linear extrapolation of the numerical shot noise data. The linear scaling of the low voltage finite size error is exploited to perform a linear extrapolation $1/M \to 0$. We find nice agreement of numerical and analytical results.
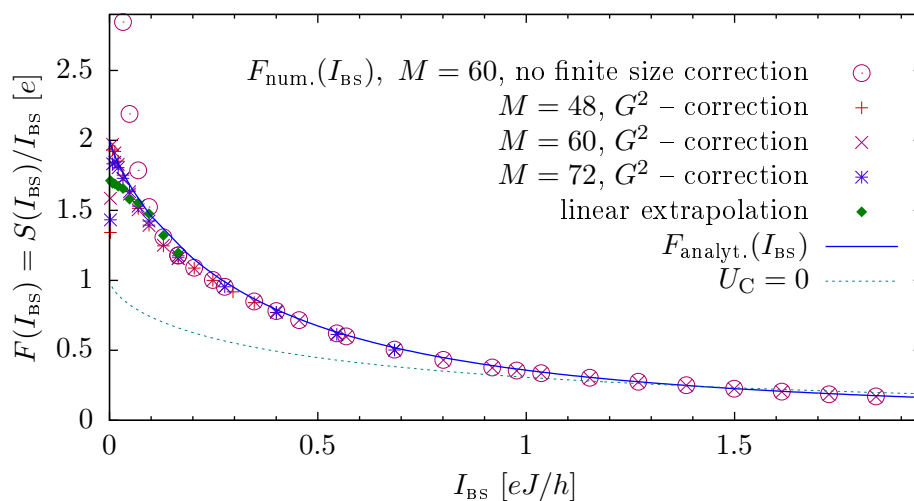

Figure 5.31 Back scattering Fano factor as a function of the back scattered current. The numerical data points have been obtained using the numerical shot noise data divided by the analytical back scattered current. The finite size error of the numerical results for shot noise leads to a diverging Fano factor. The situation improves for the linearly extrapolated data, while we find a nice agreement of the analytical result with the G^2-corrected data. For comparison we show the Fano factor in the non-interacting case.

result in order to obtain the back-scattering current I_{BS} [56]; cf. also appendix B.2. It fits nicely with the analytical result for F_{BS} as long as finite size effects can be neglected – which means in the limit of large values of I_{BS}, corresponding to values of

the bias voltage beyond the linear regime. However, the finite size offset at $I_{\mathrm{BS}} \to 0$ leads to a strongly diverging Fano factor, when no finite size corrections are applied. In contrast, F_{BS} remains finite even for very small values of I_{BS}, when obtained from the linearly extrapolated shot noise data. The deviations from the analytical result at small I_{BS} can be traced back to small absolute errors that get blown up in the limit $I_{\mathrm{BS}} \to 0$. The very nice agreement of analytical result and G^2-corrected data, even in the regime of very small I_{BS}, indicates that increasing the system size and adding more data points to the extrapolation procedure should improve the extrapolated result.

If we assume q to be the *elementary charge* in a system, where the particles tunnel *independent* of each other – and hence the probability for the tunneling of n particles in a certain time interval complies with *Poissonian* statistics – the Fano factor for the *particle* current f_{BS}

$$j_{\mathrm{BS}} = I_{\mathrm{BS}}/q \quad \Rightarrow \quad s = S/q^2, \quad \text{and hence} \quad f_{\mathrm{BS}} = j_{\mathrm{BS}}/s \quad \Rightarrow \quad F_{\mathrm{BS}} = q \cdot f_{\mathrm{BS}} \quad (5.50)$$

is equal to 1, since in this case, $s = j_{\mathrm{BS}}$. Presuming Poissonian statistics for the self-dual IRLM, we therefore can extract the elementary charge $q = 2e$ for the low-voltage limit from Fig. 5.31. If this assumption is justified is another question, which to decide would afford to compute the full counting statistics of the system.

5.6.4 Beyond the self-dual point

So far we have discussed results for shot noise in the IRLM for $U_{\mathrm{C}} = 0$ and $U_{\mathrm{C}} = 2J$, based on the numerical computation of the time evolution of a *finite* system, where we have been able to remove finite size effects by means of analytical reasoning and by a linear extrapolation to infinite system size. We could check the reliability of the approach, since for both cases, there are analytic solutions to the problem as well. We now turn to a situation with values of the interaction U_{C} different from before, where we are not aware of any exact analytical method that would provide results for the finite bias shot noise.

The question wether the current-current correlations $S(t, t')$ decay to zero within the time interval $[t_{\min}, t_{\max}]$ is crucial to the applicability of the approach, as discussed before. In Fig. 5.32 we show $S(t, t_{\min})$ for a system with $M = 88$ lattice sites, at bias voltage $V_{\mathrm{SD}} = 0.2J$, for two different values of $U_{\mathrm{C}} = 1.0J$, $3.0J$. As argued before, the maximum time that is available for the extraction of the noise power spectrum is given by $t_{\max} - t_{\min} = t_{\mathrm{R}}/2 = M/4[\hbar/J]$, which corresponds to the time window that is represented in the figure. A system of the given size clearly ranges at the top limit that can be handled on present days computers, based on the numerical method we use. The scaling procedure for the linear extrapolation to infinite system size therefore depends on the availability of reliable numerical data for systems *much smaller* than the given 88 lattice sites. As can be concluded from the left panel in Fig. 5.32, this restriction will not pose a big problem to the extraction of the zero-frequency noise in the case of $U_{\mathrm{C}} = 1J$. The correlations $S(t, t_{\min})$
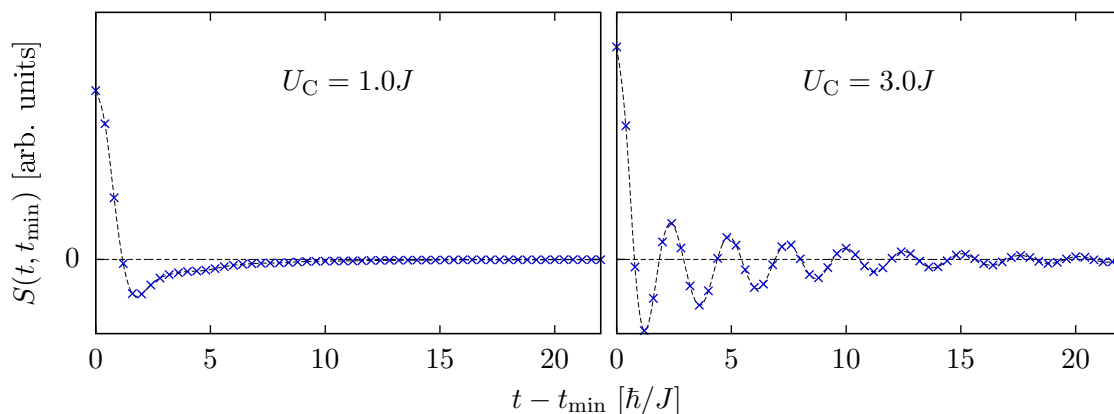
Figure 5.32 Time-dependent current-current correlations in the regime of steady current for a system with $M = 88$ lattice sites, and bias voltage $V_{SD} = 0.2J$, for two different values of the interaction U_C. The right panel visualizes the reason *why the method fails* for values of the interaction $U_C > 2J$: the correlations decay more and more slowly, for growing U_C, rendering the approximation for the low-frequency noise in Eq. (5.40) inaccurate – especially when including results for systems with only $M \sim 50$ lattice sites for the extrapolation procedure. — The black dashed lines interpolate S with cubic splines.

rapidly decay to zero, which still holds, if the system size is reduced to, say, $M = 48$ lattice sites, for example.

This statement is not true for the case $U_C = 3J$, see the right panel of the figure. Even at the upper limit of the time window, there are still finite wiggles to be found, which is of course much worse, if the system size is reduced to $M = 48$ lattice sites. For finite values of the bias voltage above a certain threshold this possibly does not matter, sice the finite cutoff error then adds to a finite noise value. The same holds for finite frequency noise for $\omega > \omega_{cut}$, as discussed before; cf. Eq. (5.41). In contrast, for $V_{SD} \to 0$ and $\omega \to 0$, where the shot noise is expected to vanish to 0, the cutoff error can not be neglected, but even worse, it does not scale linearly with $1/M$ for systems with a size in the accessible range. For increasing values of the interaction the correlations decay more and more slowly (not shown here), which is why we do not include results for shot noise for values of $U_C > 2J$ in this work.

Still, we do include results for $U_C = 1J$, where we focus on the low-voltage limit in order to extract the Fano factor. In Fig. 5.33 we show shot noise for small values of the bias voltage, where the finite size effects are very strong, in the thermodynamic limit, after liner extrapolation to $1/M \to 0$, extracted from numerical data for systems with $M = 48$, 64 and 88. On panel (a) we include the back-scattering current I_{BS}, while on panel (b), we represent S as function of I_{BS}. For the bias voltage $V_{SD} \to 0$, the shot noise vanishes, in compliance with relation (5.16).

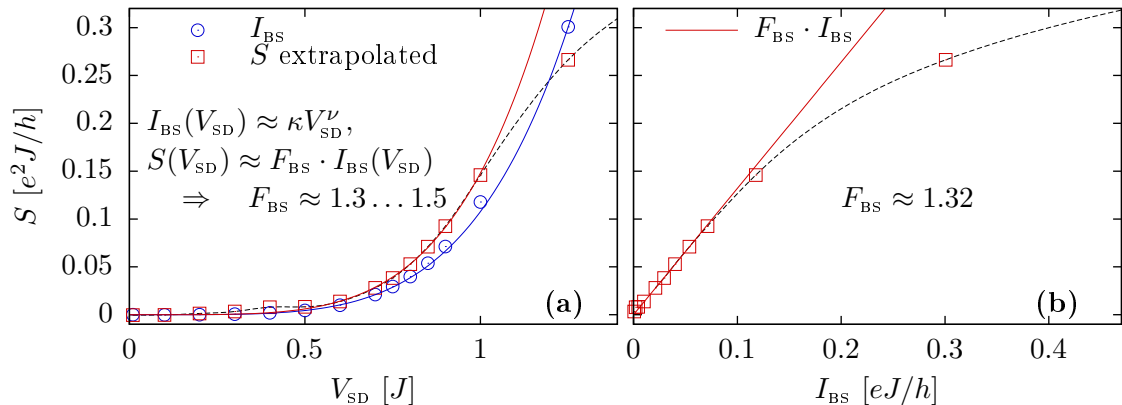Just dividing the numerical data for S and I_{BS} leads to very noisy results, since

Figure 5.33   (a) Back-scattering current I_{BS} and shot noise S as function of the bias voltage V_{SD}. The solid lines both are a fit to the given functions. For I_{BS}, we fit the parameters κ and ν, while for S we only fit the prefactor F_{BS}. The exponent strongly depends on the fit range, while F_{BS} varies on the order of magnitude of 10%. For the given figure, the fit range was chosen to be $V_{\mathrm{SD}} = 0 \ldots 0.7J$. (b) Plotting shot noise as function of the back-scattering current does not give access to the exponent; however, we now have to fit only one parameter (F_{BS}), increasing the precision for the Fano factor about one order of magnitude. — $U_{\mathrm{C}} = 1.0J$, $M = 48$, 64 and 88 lattice sites, $J_{\mathrm{C}} = 0.4J$. Shot noise S has been extrapolated to the continuum limit $1/M \to 0$. The black dashed line interpolates S with cubic splines.

this approach essentially means dividing zeros. Instead we extract the value for the Fano factor at zero voltage from a fit to a power law, where we assume for the shot noise as well as for the back-scattering current

$$I_{\mathrm{BS}}(V_{\mathrm{SD}}) \approx \kappa V_{\mathrm{SD}}^{\nu}, \quad \text{and} \quad S(V_{\mathrm{SD}}) \approx F_{\mathrm{BS}} \cdot I_{\mathrm{BS}}(V_{\mathrm{SD}}). \tag{5.51}$$

This ad-hoc assumption is motivated by the fact that in the non-interacting case as well as at the self-dual point, for the resonant tunneling situation, I_{BS} as well as S fulfill this precise relations for $V_{\mathrm{SD}} \to 0$, with the exponent $\nu = 3$ for $U_{\mathrm{C}} = 0$ and $\nu = 7$ for $U_{\mathrm{C}} = 2J$; cf. also appendix B. However, this approach still is very unstable. For a varying fit range $V_{\mathrm{SD}} = 0 \ldots V_{\max}$, $V_{\max} \in [0.5J, 0.9J]$, the fit value for F_{BS} varies on the order of $10 \ldots 15\%$, while the exponent even fluctuates by a factor of ~ 2. Alternatively, $F_{\mathrm{BS}} \approx 1.32e$ can be extracted from $S(I_{\mathrm{BS}})$, cf. Fig. 5.33 (b), with a much better precision of $\sim 10^{-2}$. Moreover, this representation reveals the range of values for I_{BS}, where $S(I_{\mathrm{BS}}) \propto I_{\mathrm{BS}}$, which in turn allows us to choose $V_{\max}$ in order to extract the exponent more reliably. We find $\nu \approx 4 \ldots 5$.

Summary and Outlook

In this chapter, we discussed numerical methods to compute quantities like finite bias current and shot noise. We therefore used the time-dependent density matrix renormalisation group (DMRG) method, which is capable of simulating the

time evolution of a quantum mechanical many-particle system in a non-equilibrium state. To check the reliability of the methods in use, we also applied exact diagonal-isation (ED) techniques in combination with a single-particle decomposition which is available for systems with suppressed electron-electron interaction only; on the other hand, ED is much cheaper than DMRG in terms of computation resources, which allows us to study much bigger systems.

A severe problem that is related to the numerical methods in use consists in the finite size of the simulated systems. Since we can not send the system size to infinity we have to deal with strong finite size effects which interfere with the "bare" result for the thermodynamic limit. Also, the finite size of the system renders a strictly steady state impossible; instead one has to seek for a quasi-steady state by looking for (more or less) time-independent expectation values of the observable of interest – which is, in our case, the current through the nanostructure – starting from an initial state that is generated by quenching the system out of equilibrium.

For these reasons, we discussed how to remove finite size effects in the first part of this chapter in great detail, where we also compared different ways of generating the initial non-equilibrium state. We showed how to extract finite bias conductance from a quasi-stationary, oscillating current. The amplitude of the oscillations could be traced back to the finite size energy gap of the model, while the frequency turned out to be equivalent to the bias voltage, allowing for an interpretation as Josephson current. The effects related to the leads being composed of an even or odd number of lattice sites (even-odd effect), which strongly affect the time-dependent current particularly at low bias voltage, appear to be connected to the structure of the single-particle energy levels in the leads. This knowledge could be used to remove the even-odd effect by adding a potential energy of the order of the finite size gap to the leads, shifting the levels of the two leads relative to each other. We furthermore showed how to remove effects due to the density shift in the leads which also results from the finite size of the system. Finally we discussed results for the differential and linear conductance of an interacting 7-site structure.

In the following section we investigated the applicability of damped boundary conditions in order to reduce finite size effects. While frequently used before in order to enhance the energy resolution at the Fermi level for the computation of low-energy properties, we analysed the technique for the computation of finite-bias current-voltage characteristics, where we interpreted the enhanced energy resolution as an effectively increased system size which allows for a correspondingly longer period of a steady current.

The most important topic of this chapter was the computation of shot noise at fi-nite bias. In the last section, we introduced a new way of extracting noise from time evolution calculations. We thereby could profit from the techniques that had been used before to extract the finite bias conductance. The presented method is inde-pendent of the underlying numerical simulation of the time evolution; while for the treatment of the non-interacting RLM we applied exact diagonalisation techniques, the results for the IRLM have been obtained using the time-dependent DMRG.

However, the results for the low-frequency noise again turned out to be plagued by strong finite size effects. The availability of analytical results for special situations – the RLM without interaction and the IRLM at its self-dual point – provided a great service in analysing the nature of the finite size effects. In the zero frequency regime, we could show that the finite size error scales G^2-dependent, with the differential conductance G. For sufficiently large systems we furthermore found the error to scale proportional to the inverse system size, which finally allowed to remove the finite size error by means of a linear extrapolation to infinite system size. Based on this finite size analysis we were able to obtain numerical results which corrrespond very nicely to the analytic results for the non-interacting case as well as for the IRLM in the self-dual point, where analytical solutions based on the thermodynamic Bethe ansatz have been presented in [85]. Moreover we have been providing results for the shot noise in a regime of the interaction where we are not aware of exact analytic methods to treat the problem. Most strikingly our results show an enhancement of the back scattered Fano factor due to interaction effects.

Finally we also explored the limitations of the method. Increasing the interaction beyond the self-dual point leads to a growth of time-dependent current-current correlations, which enforces us to increase the size of the simulated system. The presently available computing resources – in terms of computing time and in terms of memory – prevented us doing so. Therefore the application of this approach on situations with slowly decaying correlations is left for future research.

The results presented for the shot noise have been obtained by a time evolution simulation, with a subsequent Fourier transform to the frequency space. Alternatively, we can also imagine to apply a combined approach of time evolution simulation in order to obtain a steady current as an initial state, and then to obtain the noise power spectrum by means of a polynomial expansion for a resolvent expression as outlined in the summary of chapter 4 for non-equilibrium Green's funcions. This would provide access to a different method for the treatment of finite size errors, based on finite convergence generating factors, as discussed in chapter 4.

Despite its limitations, the method of real-time evolution based on the time-dependent DMRG has been successfully applied to a number of problems, including the extraction of finite-bias current-voltage characteristics for various models, and now shot noise in the interacting resonant level model. This evolution suggests as a next step to extend the method to higher order correlations, or even to the full counting statistics. First efforts in this direction are encouraging.

Conclusions

The aim of the present work was to investigate numerical methods suitable for the computation of transport properties for the electron transport in interacting nanostructures. A method which is capable of handling the full many-particle wave function, even for non-equilibrium situations, is the density matrix renormalisation group (DMRG) approach. It is based on a sophisticated projection scheme in combination with the iterative increase of the system size and therefore allows for the treatment of systems which are not accessible by exact diagonalisation. For our considerations, the DMRG therefore can be considered the "backbone" of the numerical simulations.

On top of this, we developed an expansion scheme based on Chebyshev polynomials, which allows to evaluate Green's functions. Here, we applied this scheme to obtain the single particle spectrum of the interacting resonant level model (IRLM). In contrast to the correction vector method, this expansion does not show any convergence problems and allows to extract the full frequency dependency of the Green's function from a single set of numerical data. Furthermore, the explicit inclusion of a broadening factor allows for a reliable extrapolation to the thermodynamic limit from data of finite systems. For the present problem, we could show that the method yields results in good agreement with analytic calculations for the free fermion case. Furthermore we obtained results for finite values of the interaction. This method is very general and can be applied to any model that is treatable by DMRG. The main restriction consists in the fact, that the expansion order grows linearly with the desired energy resolution, which makes the method inappropriate for resolving narrow structures in the spectrum.

For the computation of the current-voltage characteristics and finite-bias shot noise in the IRLM, we applied the time-dependent DMRG approach, which is capable of simulating the time evolution of a quantum mechanical many-particle system in a non-equilibrium state. We introduced a new way of extracting noise from time evolution calculations. Similar to the finite size effects for the time-dependent current, we found the shot noise to be strongly affected by finite size effects. The availability of analytical results for special situations – the RLM without interaction and the IRLM at its self-dual point – provided a great service in analysing the nature of the finite size effects. In the zero frequency regime, we could show that the finite size error scales G^2-dependent, with the differential conductance G. For sufficiently large systems we furthermore found the error to scale proportional to the inverse system size, with a voltage-independent scale factor, which finally allowed to remove the finite size error by means of a linear extrapolation to infinite system size. Based on this finite size analysis we were able to obtain numerical results

which correnspond very nicely to the analytic results for the non-interacting case as well as for the IRLM at the self-dual point, where analytical solutions based on the thermodynamic Bethe ansatz have been presented in [85]. Moreover we have been providing results for the shot noise in a regime of the interaction where we are not aware of exact analytic methods to treat the problem. Most strikingly our results show an enhancement of the back scattered Fano factor due to interaction effects. At the self-dual point of the model, the Fano factor approaches a value of 2 electron charges.

Appendix

Appendix A

Level Discretisation Effects

The single particle levels ε_k of an uncoupled, noninteracting tight-binding lead with M_α sites ($\alpha = \mathrm{L}, \mathrm{R}$)

$$\hat{H}_\alpha = -J \sum_{x=1}^{M_\alpha - 1} (\hat{c}_{\alpha,x}^\dagger \hat{c}_{\alpha,x+1} + \hat{c}_{\alpha,x+1}^\dagger \hat{c}_{\alpha,x}) \tag{A.1}$$

are given by

$$\varepsilon_j = -2J \cos[\pi j/(M_\alpha + 1)] = -2J \cos k_j, \tag{A.2}$$

$j = 1, \ldots, M_\alpha$, see Fig. A.1. The energy of a particle residing on a decoupled single dot structure ($J_\mathrm{C} = 0$)

$$\hat{H}_\mathrm{d} = V_g \, \hat{c}_\mathrm{d}^\dagger \hat{c}_\mathrm{d} \tag{A.3}$$

is simply given by the gate voltage $\epsilon_\mathrm{d} = V_\mathrm{g}$, which is at the Fermi edge for $V_\mathrm{g} = 0$.[1]
For an equal number of sites on both leads (as for example oM_So, Fig. A.2(a) or eM_Se, Fig. A.2(c)) there is a twofold degeneracy of the single particle lead levels which does not exist if $M_\mathrm{L} = M_\mathrm{R} \pm 1$, Fig. A.2(b). In the degenerate case, single particle eigenfunctions can be constructed with a fully delocalized particle density

---

[1]For a decoupled M_S-dot structure one gets $\epsilon_{\mathrm{d},j} = -2J_\mathrm{S} \cos[\pi j/(M_\mathrm{S} + 1)] + V_\mathrm{g}$, $j = 1, \ldots, M_\mathrm{S}$.
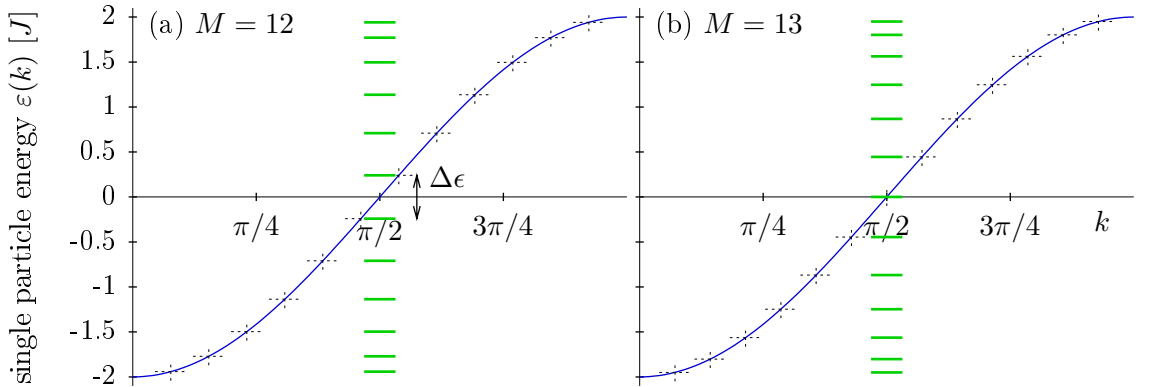
Figure A.1 Single particle energy levels of 1D tight binding chains. For an even number of lattice sites (a), there are two discrete levels at energies $\varepsilon = \pm\Delta\varepsilon/2$, but there is no level at $\varepsilon = 0$, in contrast to a situation with an odd number of lattice sites (b).
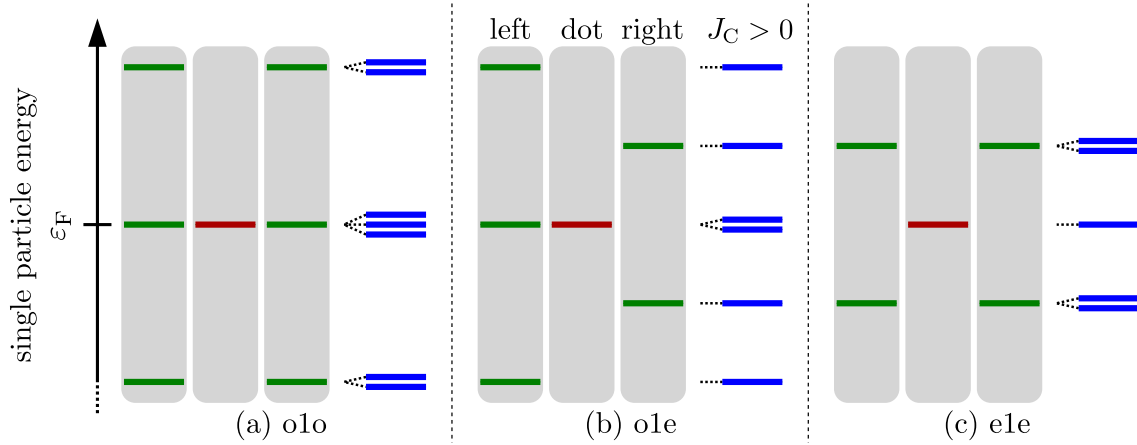
Figure A.2   Degeneracy of single particle energy levels of a single dot coupled to two leads with different configurations

while for $M_\mathrm{L} = M_\mathrm{R} \pm 1$, the density profile of the single particle wave functions shows an alternating confinement of the particle on either the left or the right lead. The same holds true for the energy levels of the structure: if degenerate with a lead level, the single particle wave function can be distributed over the whole lead while it is localized on the structure otherwise. Therefore, in the e1e case, the single-dot level is not degenerate with the lead levels when $\epsilon_\mathrm{d} = 0$. As a result, a single particle occupying the dot level generates a sharp peak in the density profile (as well as the spin profile). For the o1o case on the other hand, both leads have one energy level in the middle of the band, which together with the dot level generates a threefold degeneracy. For finite coupling $J_\mathrm{C} > 0$,

$$\hat{H} = \hat{H}_0 + \hat{H}_1, \qquad \hat{H}_0 = \hat{H}_\mathrm{L} + \hat{H}_\mathrm{R} + \hat{H}_\mathrm{d}, \tag{A.4}$$

$$\hat{H}_1 = -J_\mathrm{C}(\hat{c}_\mathrm{d}^\dagger \hat{c}_{\mathrm{L},1} + \hat{c}_\mathrm{d}^\dagger \hat{c}_{\mathrm{R},1} + \mathrm{H.c.}), \tag{A.5}$$

the degeneracy of the lead levels and of the levels of the structure with the lead levels gets lifted. The single particle wave functions must be divided equally on both leads, when $M_\mathrm{L} = M_\mathrm{R}$, while the alternating confinement is preserved for $M_\mathrm{L} = M_\mathrm{R} \pm 1$. Concerning the energy level of the dot, the threefold degeneracy in the uncoupled o1o case results in two levels with strong localization on the dot, one lifted above the Fermi edge and one pushed below, and a third level with vanishing particle density on the dot, remaining on the Fermi edge (Fig. A.2(a)).

Perturbation Theory for a Structure coupled to 1D Tight Binding Leads   This can be demonstrated by calculating the single particle energy levels at the Fermi edge as well as the corresponding wave functions for finite coupling J_C using first order perturbation theory. Starting from the unperturbed system with $J_\mathrm{C} = 0$, the

single particle wave functions read ($\alpha = \mathrm{L}, \mathrm{R}$; $M_\mathrm{L} = M_\mathrm{R}$ odd)

$$|\alpha, k\rangle = \frac{1}{\sqrt{\mathcal{N}_k}} \sum_{x=1}^{M_\alpha} \sin(kx) \hat{c}_{\alpha,x}^\dagger |\rangle, \quad |\mathrm{d}\rangle = \hat{c}_\mathrm{d}^\dagger |\rangle. \tag{A.6}$$

For $V_\mathrm{g} = 0$ and $k = \pi/2$, the perturbation $\hat{H}_1$ can be diagonalized using

$$|\nu, \frac{\pi}{2}\rangle = \frac{1}{\sqrt{2}} \left(\sin(\frac{\nu\pi}{4})|L, \frac{\pi}{2}\rangle + \sin(\frac{\nu\pi}{2})|\mathrm{d}\rangle + \sin(\frac{3\nu\pi}{4})|R, \frac{\pi}{2}\rangle \right), \quad \nu \in \{1, 2, 3\}, \tag{A.7}$$

and the first order correction of the energy levels reads

$$\Delta\epsilon_\nu = \langle\nu, \frac{\pi}{2}|\hat{H}_1|\nu, \frac{\pi}{2}\rangle = -\frac{J_\mathrm{C}}{\sqrt{\mathcal{N}_{\pi/2}}} \left(\sin(\frac{\nu\pi}{4}) + \sin(\frac{3\nu\pi}{4}) \right) \sin(\frac{\nu\pi}{2})$$

$$= -J_\mathrm{C} \frac{2\cos(\nu\pi/4)}{\sqrt{\mathcal{N}_{\pi/2}}} \tag{A.8}$$

with normalisation $\mathcal{N}_{\pi/2} = (M_\alpha + 1)/2$. We find $\Delta\epsilon_1 = -J_\mathrm{C}\sqrt{2/\mathcal{N}_{\pi/2}} = -\Delta\epsilon_3$, as well as $\Delta\epsilon_2 = 0$. In addition, Eq. (A.7) shows that the wave function $|\nu = 2, \pi/2\rangle$ is suppressed on the dot while it is strongly concentrated there for $\nu = 1$ or $\nu = 3$.

Appendix B

Analytic Results for Current and Shot Noise

B.1 Non-Interacting models

The Landauer–Büttiker method [19–21, 119] can be used to obtain the finite bias conductance and shot noise for the current through a mesoscopic region, if the interaction of the constituent particles can be neglected. From the knowledge of the transmission amplitude of an incoming particle, that is scattered from one lead through the mesoscopic region into the other lead (cf. Fig. B.1), the transmission *probability* can be computed, which then allows the computation of current and shot noise by means of integration over the occupied states. In chapter 5 we make use of this analytic approach to check the reliability of the numerical methods we use in the case of the resonant level model as well as in the case of a model with a two-dot structure, coupled to two 1D leads. We therefore provide the analytic expressions that have been used there.

The basic idea is to make an ansatz for a scattering state, which is assumed to be an eigen-state of the Hamiltonian of the system. This state has several unknown parameters, to be precise, the reflection amplitude r, the transmission amplitude t as well as several contributions of the degerees of freedom of the structure. The free parameters then have to be fixed by means of the eigen-state assumption.

The resulting transmission probability $T = |t|^2$ then has to be plugged into the
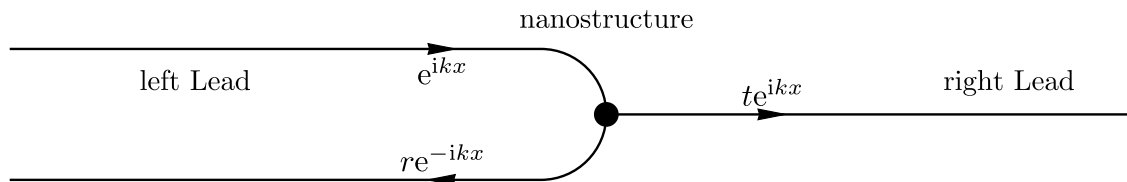
Figure B.1   Scattering states and Landauer–Büttiker formula. We assume that for the transport through a *non-interacting* mesoscopic structure coupled to two 1D leads, the transport properties of the system can be obtained using scattering states. Incoming particles are represented as plain waves, which are reflected back as a plain wave with amplitude r, and transmitted to the other lead with amplitude t.

Appendix B Analytic Results for Current and Shot Noise

Landauer–Büttiker formulas for single-channel current I and zero-frequency shot noise S. Since we always consider zero-temperature transport for a model with cosine dispersion $\varepsilon_k = -2J\cos k$, where we assume half filling $\Rightarrow k_{\mathrm{F}} = \pi/2$, $\varepsilon_{\mathrm{F}} = 0$, it is reasonable to introduce the source-drain voltage V_{SD} *symmetrically* around the structure. The expressions for current and shot noise then read

$$I(V_{\mathrm{SD}}) = \frac{e}{h} \int\limits_{-V_{\mathrm{SD}}/2}^{V_{\mathrm{SD}}/2} \mathrm{d}\varepsilon\, T(\varepsilon) \quad \text{and} \quad S(V_{\mathrm{SD}}) = \frac{2e^2}{h} \int\limits_{-V_{\mathrm{SD}}/2}^{V_{\mathrm{SD}}/2} \mathrm{d}\varepsilon\, [1 - T(\varepsilon)]T(\varepsilon). \quad \text{(B.1)}$$

For details on the derivation see, for example, Ref. [119]. The differential conductance G can be obtained from $I(V_{\mathrm{SD}})$ by

$$G(V_{\mathrm{SD}}) = e\frac{\partial I(V_{\mathrm{SD}})}{\partial V_{\mathrm{SD}}} = \frac{e^2}{2h}[T(V_{\mathrm{SD}}/2) + T(-V_{\mathrm{SD}}/2)]. \quad \text{(B.2)}$$

Resonant Level Model The ansatz scattering-state for the resonant level model with 1D leads looks as follows. Since there is only one level on the structure, we need only one parameter d to represent the dot level ($x = 0$). The reflection of the particle back to the "incoming" lead ($x = -\infty \ldots -1$) is represented by r, while the transmission to the "outgoing" lead ($x = 1 \ldots \infty$) is represented by t. Then

$$\hat{c}_k^\dagger = \sum_{x=-\infty}^{-1} (\mathrm{e}^{\mathrm{i}kx} + r\mathrm{e}^{-\mathrm{i}kx})\hat{c}_x^\dagger + d\hat{c}_0^\dagger + t\sum_{x=1}^{\infty} \mathrm{e}^{\mathrm{i}kx}\hat{c}_x^\dagger. \quad \text{(B.3)}$$

The Hamiltonian for the resonant level model *without* interaction is given by

$$\hat{H}_{\mathrm{RLM}} = -J\sum_{x=1}^{\infty}(\hat{c}_x^\dagger\hat{c}_{x+1} + \hat{c}_{x+1}^\dagger\hat{c}_x + \hat{c}_{-x}^\dagger\hat{c}_{-x-1} + \hat{c}_{-x-1}^\dagger\hat{c}_{-x}) + V_{\mathrm{g}}\hat{n}_0$$
$$- J_{\mathrm{C}}(\hat{c}_0^\dagger\hat{c}_1 + \hat{c}_1^\dagger\hat{c}_0 + \hat{c}_0^\dagger\hat{c}_{-1} + \hat{c}_{-1}^\dagger\hat{c}_0) \quad \text{(B.4)}$$

which can be obtained from (2.15) by setting $U_{\mathrm{C}} \equiv 0$. The energy of the system is increased by ε_k by adding a particle $\hat{c}_k^\dagger$, therefore

$$[\hat{H}_{\mathrm{RLM}}, \hat{c}_k^\dagger] = \varepsilon_k\hat{c}_k^\dagger. \quad \text{(B.5)}$$

This relation generates a set of equations for the unknown parameters ε_k, d, r and t, which can be used to obtain the dispersion relation

$$\varepsilon_k = -2J\cos k \quad \text{(B.6)}$$

and the transmission amplitude

$$t = \frac{2\mathrm{i}\sin k}{(\varepsilon_k - V_{\mathrm{g}})J/J_{\mathrm{C}}^2 + 2\mathrm{e}^{\mathrm{i}k}}. \quad \text{(B.7)}$$

as well as the transmission probability

$$T = |t|^2 = \frac{4J^2 - \varepsilon_k^2}{[\varepsilon_k((J/J_{\mathrm{C}})^2 - 1) - V_{\mathrm{g}}(J/J_{\mathrm{C}})^2]^2 + 4J^2 - \varepsilon_k^2}. \qquad (B.8)$$

The evaluation of Eq. (B.1), for the resonant case with the gate voltage set to zero $V_{\mathrm{g}} = 0$, finally leads to ($\eta_{\mathrm{C}} \equiv J_{\mathrm{C}}/J$, $v_{\mathrm{SD}} \equiv V_{\mathrm{SD}}/J$)

$$I(V_{\mathrm{SD}}) = \frac{\eta_{\mathrm{C}}^2}{\sqrt{1 - 2\eta_{\mathrm{C}}^2}^3} \left\{ 4(1 - \eta_{\mathrm{C}}^2)^2 \arctan\left(\frac{v_{\mathrm{SD}}\sqrt{1 - 2\eta_{\mathrm{C}}^2}}{4\eta_{\mathrm{C}}^2}\right) - \eta_{\mathrm{C}}^2 \sqrt{1 - 2\eta_{\mathrm{C}}^2} \cdot v_{\mathrm{SD}} \right\} \qquad (B.9)$$

and

$$S(V_{\mathrm{SD}}) = \frac{J}{2}\left(1 + \frac{\eta_{\mathrm{C}}^4}{1 - 2\eta_{\mathrm{C}}^2}\right) \left\{ \frac{4\eta_{\mathrm{C}}^2}{\sqrt{1 - 2\eta_{\mathrm{C}}^2}} \left[1 + 3\frac{\eta_{\mathrm{C}}^4}{1 - 2\eta_{\mathrm{C}}^2}\right] \times \right.$$
$$\left. \times \arctan\left(\frac{v_{\mathrm{SD}}\sqrt{1 - 2\eta_{\mathrm{C}}^2}}{4\eta_{\mathrm{C}}^2}\right) - v_{\mathrm{SD}}\frac{1 + 3\eta_{\mathrm{C}}^4/(1 - 2\eta_{\mathrm{C}}^2) + v_{\mathrm{SD}}^2/8}{1 + (v_{\mathrm{SD}}\sqrt{1 - \eta_{\mathrm{C}}^2}/4\eta_{\mathrm{C}}^2)^2} \right\}. \quad (B.10)$$

In the limit of small bias voltage, the expansion with respect to V_{SD} yields

$$S(V_{\mathrm{SD}}) \propto V_{\mathrm{SD}}^3. \qquad (B.11)$$

For finite values of V_{g} the corresponding expressions become quite complicated. On the other hand, Eq. (B.1) can be computed by numerical integration. We therefore contend ourselves by giving the above results for the on-resonance situation.

Remarks on the connection to the equilibrium single-particle spectral function of the dot   In chapter 4, we compute the single-particle spectral function of the dot numerically. Here, we provide an analytic expression for the spectral function of the noninteracting RLM for comparison.

For symmetric coupling J_{C} to the left and the right lead, the retarded Green's function $\mathcal{G}^{\mathrm{r}}$ can be related to the transmission *probability* [35] as

$$T(\varepsilon_k) = t^* t = -\mathrm{Im}[\Gamma(\varepsilon_k)\mathcal{G}^{\mathrm{r}}(\varepsilon_k)]. \qquad (B.12)$$

Here, $\Gamma(\varepsilon_k) = 2\pi\rho(\varepsilon_k)V_k V_k^*$, where ρ is the density of states in the tight-binding chain with cosine dispersion, $\rho(\varepsilon_k) = (J\sin k)^{-1}$, and V_k is the coupling of the dot level to the *momentum modes* in the semi-infinite chains, $V_k = -J_{\mathrm{C}}\sin k/\sqrt{\pi}$. Then

$$\mathcal{A}(\varepsilon_k) = -\frac{1}{\pi}\mathrm{Im}\mathcal{G}^{\mathrm{r}}(\varepsilon_k) = \frac{T(\varepsilon_k)}{\pi\Gamma(\varepsilon_k)} = \frac{T(\varepsilon_k)}{\pi\sin k}\frac{J}{2J_{\mathrm{C}}^2}. \qquad (B.13)$$

Structure with two lattice sites For the system with $M_S = 2$ lattice sites on the structure, we provide the transmission probability $T(\varepsilon)$. The Hamiltonian is given by

$$\hat{H}_{\mathrm{RLM}} = -J \sum_{x=1}^{\infty} (\hat{c}_x^\dagger \hat{c}_{x+1} + \hat{c}_{x+1}^\dagger \hat{c}_x + \hat{c}_{-x}^\dagger \hat{c}_{-x-1} + \hat{c}_{-x-1}^\dagger \hat{c}_{-x})$$
$$- J_{\mathrm{C}}(\hat{c}_{0\mathrm{R}}^\dagger \hat{c}_1 + \hat{c}_1^\dagger \hat{c}_{0\mathrm{R}} + \hat{c}_{0\mathrm{L}}^\dagger \hat{c}_{-1} + \hat{c}_{-1}^\dagger \hat{c}_{0\mathrm{L}}) - J_{\mathrm{S}}(\hat{c}_{0\mathrm{L}}^\dagger \hat{c}_{0\mathrm{R}} + \hat{c}_{0\mathrm{R}}^\dagger \hat{c}_{0\mathrm{L}}) \quad \text{(B.14)}$$

For simplicity we do not include a gate voltage. Here, we denote the coupling of the two lattice sites *on the structure* J_S, as well as the coupling of the structure to the leads J_C. The ansatz scattering states read

$$\hat{c}_k^\dagger = \sum_{x=-\infty}^{-1} (\mathrm{e}^{ikx} + r\mathrm{e}^{-ikx})\hat{c}_x^\dagger + d_\mathrm{L}\hat{c}_{0\mathrm{L}}^\dagger + d_\mathrm{R}\hat{c}_{0\mathrm{R}}^\dagger + t\sum_{x=1}^{\infty} \mathrm{e}^{ikx}\hat{c}_x^\dagger. \quad \text{(B.15)}$$

The procedure outlined before yields the dispersion relation $\varepsilon_k = -2J\cos k$ again, the transmission probability reads ($\eta_\mathrm{C} = J_\mathrm{C}/J$, $\eta_\mathrm{S} = J_\mathrm{S}/J$)

$$T = \frac{\eta_\mathrm{S}^2 \eta_\mathrm{C}^4 (4 - \varepsilon_k^2/J^2)}{\mathcal{F}_- \cdot \mathcal{F}_+}, \qquad \mathcal{F}_\pm = \Big[\frac{\varepsilon_k}{J}\Big(1 - \frac{\eta_\mathrm{C}^2}{2}\Big) \pm \eta_\mathrm{S}\Big]^2 + \frac{\eta_\mathrm{C}^4}{4}\Big(4 - \frac{\varepsilon_k^2}{J^2}\Big). \quad \text{(B.16)}$$

B.2 Wide-band limit and the self-dual point of the IRLM

In [56, 85], E. Boulat and H. Saleur provided analytic results for current and shot noise for the self-dual IRLM in the wide-band limit, based on a continuum field-theoretic description of the model,

$$\hat{H} = \hat{H}_0 + \hat{H}_\mathrm{B}, \quad \hat{H}_0 = -\mathrm{i}\sum_{\alpha=\mathrm{L,R}} \int_{-\infty}^{\infty} \mathrm{d}x \ \hat{\psi}_\alpha^\dagger(x)\partial_x\hat{\psi}_\alpha(x), \quad \text{(B.17)}$$

$$\hat{H}_\mathrm{B} = \gamma\Big\{ \big[\hat{\psi}_\mathrm{L}^\dagger(0) + \hat{\psi}_\mathrm{R}^\dagger(0)\big]\hat{d} + \hat{d}^\dagger\big[\hat{\psi}_\mathrm{L}(0) + \hat{\psi}_\mathrm{R}(0)\big] \Big\}$$
$$+ U\big[: \hat{\psi}_\mathrm{L}^\dagger(0)\hat{\psi}_\mathrm{L}(0) : + : \hat{\psi}_\mathrm{R}^\dagger(0)\hat{\psi}_\mathrm{R}(0) : \big](\hat{d}^\dagger\hat{d} - 1/2), \quad \text{(B.18)}$$

with symmetric coupling γ and the dot level $\hat{d}$ on resonance (the contribution $V_g\hat{d}^\dagger\hat{d}$ vanishes). In this continuum description, the self-dual point corresponds to a value of $U = \pi$. At temperature $T = 0$, the current-voltage characteristics then is given as [56]

$$I_0(V_{\mathrm{SD}}) = V_{\mathrm{SD}} \sum_{n=0}^{\infty} \frac{(-1)^n}{4\sqrt{\pi}} \frac{(4n)!}{n!\Gamma[3(n+1/2)]} \bar{V}_{\mathrm{SD}}^{6n} \qquad \text{for } \bar{V}_{\mathrm{SD}} < \mathrm{e}^\Delta, \quad \text{(B.19)}$$

$$I_0(V_{\mathrm{SD}}) = V_{\mathrm{SD}} \sum_{n=1}^{\infty} \frac{(-1)^{n+1}}{4\sqrt{\pi}} \frac{\Gamma(1+n/4)}{n!\Gamma[3/2 - 3n/4]} \bar{V}_{\mathrm{SD}}^{-3n/2} \qquad \text{for } \bar{V}_{\mathrm{SD}} > \mathrm{e}^\Delta, \quad \text{(B.20)}$$

with $e^\Delta = \sqrt{3}/4^{2/3}$ and the natural expansion variable

$$\bar{V}_{\text{SD}} = \frac{\Gamma(1/6)}{4\sqrt{\pi}\Gamma(2/3)} \frac{V_{\text{SD}}}{T_{\text{B}}}. \tag{B.21}$$

Furthermore, the shot noise is related to the current as [85]

$$S(V_{\text{SD}}) = \frac{1}{3}\left[I_0(V_{\text{SD}}) - V_{\text{SD}} \cdot \frac{\partial I_0(V_{\text{SD}})}{\partial V_{\text{SD}}} \right]. \tag{B.22}$$

T_{B} is a scale. Note, that I_0/T_{B}, as well as S/T_{B}, depends on $\bar{V}_{\text{SD}}$ *only*. Matching the numerical results presented in section 5.6.1 on the analytic results therefore requires a *single* rescaling of I_0 and V_{SD}. The low-voltage expansion of the shot-noise can be deduced from Eqns. (B.19) and (B.22) and fulfills

$$S(V_{\text{SD}}) \propto V_{\text{SD}}^7. \tag{B.23}$$

Frequency-dependent noise for $U_{\text{C}} = 0$ Furthermore, the frequency-dependent shot noise for the *non-interacting* RLM has been provided by E. Boulat and H. Saleur in the wide-band limit in [84]. It reads

$$S(\omega, V_{\text{SD}}, T_{\text{B}}) = \frac{T_{\text{B}}}{4}\Theta(V_{\text{SD}} - |\omega|)\left\{\left[\arctan\left(\frac{V_{\text{SD}}}{T_{\text{B}}}\right) + \arctan\left(\frac{V_{\text{SD}} - 2|\omega|}{T_{\text{B}}}\right) \right]\right.$$
$$+ \frac{T_{\text{B}}}{4}\left\{ \arctan\left(\frac{V_{\text{SD}} + 2|\omega|}{T_{\text{B}}}\right) - \arctan\left(\frac{V_{\text{SD}} - 2|\omega|}{T_{\text{B}}}\right) \right\}$$
$$\left. + \frac{T_{\text{B}}}{2\omega} \ln\left(\frac{T_{\text{B}}^2 + (V_{\text{SD}} - 2|\omega|)^2}{T_{\text{B}}^2 + V_{\text{SD}}^2}\right) \right\}, \tag{B.24}$$

where the scale is now given by $T_{\text{B}} = 4J_{\text{C}}^2/J$, for $J_{\text{C}} \ll J$.

B.3 Low-frequency shot noise in the ground state

The noise power spectrum $S(\omega)$ is defined by the Fourier transform of the current-current correlations, cf. Eq. (5.13). We now assume that the expectation value $\langle \cdot \rangle$ is obtained for the ground state $|\Psi_0\rangle$ of the system.[1] Based on general arguments we now show that in this case,

$$S(\omega = 0) = 0. \tag{B.25}$$

In order to prove this relation, we first of all want to note that in the ground state, there is no current flow $\langle\Psi_0|\hat{I}|\Psi_0\rangle = 0$, which implies $\Delta\hat{I} = \hat{I}$. Starting from

---

[1]For the ground state energy E_0 being degenerate, we randomly choose a state that holds $\hat{H}|\Psi_0\rangle = E_0|\Psi_0\rangle$.

Eq. (5.13), we then find

$$
S(\omega^+) = 2\mathrm{Re} \int\limits_0^\infty \mathrm{d}t \ e^{i\omega^+ t} \, \langle\Psi_0| \Big[\hat{I}(t)\hat{I}(0) + \hat{I}(0)\hat{I}(t) \Big] |\Psi_0\rangle
$$

$$
= 2\mathrm{Re} \int\limits_0^\infty \mathrm{d}t \ e^{i\omega^+ t} \, \langle\Psi_0|\hat{I} \Big[e^{i(E_0-\hat{H})t/\hbar} + e^{-i(E_0-\hat{H})t/\hbar} \Big] \hat{I}|\Psi_0\rangle
$$

$$
= -2\mathrm{Im}\langle\Psi_0|\hat{I} \Big[\frac{1}{(E_0-\hat{H})/\hbar + \omega^+} + \frac{1}{-(E_0-\hat{H})/\hbar + \omega^+} \Big] \hat{I}|\Psi_0\rangle, \quad \text{(B.26)}
$$

where ω^+ contains a convergence generating factor, $\mathrm{Im}\,\omega^+ = \eta \to 0^+$. To proceed, we insert a complete basis of eigenstates $\{|\Psi_n\rangle\}$ of the Hamiltonian of the system, with energy $E_n|\Psi_n\rangle = \hat{H}|\Psi_n\rangle$. The above expression then translates to

$$
-2\mathrm{Im}\sideset{}{'}\sum_n \langle\Psi_0|\hat{I}|\Psi_n\rangle\langle\Psi_n| \Big[\frac{1}{(E_0-E_n)/\hbar + \omega^+} - \frac{1}{(E_0-E_n)/\hbar - \omega^+} \Big] \hat{I}|\Psi_0\rangle, \quad \text{(B.27)}
$$

where the dashed symbol for the sum $\sum'$ indicates, that we *exclude* the (degenerate) ground state from the sum. This is allowed for the following reason: we are free to choose the basis $\{|\Psi_n\rangle\}$ in such a way that the current operator $\hat{I}$ is diagonal in the *subspace* of the degenerate ground state. For $E_n = E_0$ then $\langle\Psi_0|\hat{I}|\Psi_n\rangle = 0$. The remaining contributions then fulfill $\Delta_n \equiv (E_0 - E_n)/\hbar \neq 0$, leading to

$$
\frac{1}{\Delta_n + \omega^+} - \frac{1}{\Delta_n - \omega^+} = \frac{\Delta_n + \omega - i\eta}{(\Delta_n + \omega)^2 + \eta^2} - \frac{\Delta_n - \omega + i\eta}{(\Delta_n - \omega)^2 + \eta^2}
$$

$$
\xrightarrow{\omega\to 0} \frac{-2i\eta}{\Delta_n^2 + \eta^2} \xrightarrow{\eta\to 0^+} -2\pi i\delta(\Delta_n). \quad \text{(B.28)}
$$

Since we excluded the (degenerate) ground state, the sum vanishes identically, proving the relation (B.25).

Bibliography

[1] M. A. Reed, J. Chen, A. M. Rawlett, D. W. Price, and J. M. Tour, Molecular random access memory cell, Applied Physics Letters **78**(23), 3735–3737 (2001).

[2] E. Lörtscher, J. Ciszek, J. Tour, and H. Riel, Reversible and Controllable Switching of a Single-Molecule Junction, Small **2**, 973–977 (2006).

[3] V. Meded, A. Bagrets, A. Arnold, and F. Evers, Molecular Switch Controlled by Pulsed Bias Voltages, Small **5**, 2218–2223 (2009).

[4] D. Goldhaber-Gordon, H. Shtrikman, D. Mahalu, D. Abusch-Magder, U. Meirav, and M. A. Kastner, Kondo effect in a single-electron transistor, Nature **391**, 156–159 (1998).

[5] D. Goldhaber-Gordon, J. Göres, M. A. Kastner, H. Shtrikman, D. Mahalu, and U. Meirav, From the kondo regime to the mixed-valence regime in a single-electron transistor, Phys. Rev. Lett. **81**(23), 5225–5228 (1998).

[6] S. M. Cronenwett, T. H. Oosterkamp, and L. P. Kouwenhoven, A Tunable Kondo Effect in Quantum Dots, Science **281**(5376), 540–544 (1998), http://www.sciencemag.org/content/281/5376/540.full.pdf.

[7] J. Schmid, J. Weis, K. Eberl, and K. v. Klitzing, A quantum dot in the limit of strong coupling to reservoirs, Physica B: Condensed Matter **256-258**, 182–185 (1998).

[8] S. Gustavsson, R. Leturcq, B. Simovič, R. Schleser, T. Ihn, P. Studerus, K. Ensslin, D. C. Driscoll, and A. C. Gossard, Counting Statistics of Single Electron Transport in a Quantum Dot, Phys. Rev. Lett. **96**(7), 076605 (2006).

[9] C. Fricke, F. Hohls, N. Sethubalasubramanian, L. Fricke, and R. J. Haug, High-order cumulants in the counting statistics of asymmetric quantum dots, Applied Physics Letters **96**(20), 202103 (2010).

[10] S. Iijima, Helical microtubules of graphitic carbon, Nature **354**, 56–58 (1991).

[11] S. J. Tans, M. H. Devoret, H. Dai, A. Thess, R. E. Smalley, L. J. Geerligs, and C. Dekker, Individual single-wall carbon nanotubes as quantum wires, Nature **386**, 474–477 (1997).

[12] C. Kergueris, J. P. Bourgoin, S. Palacin, D. Esteve, C. Urbina, M. Magoga, and C. Joachim, Electron transport through a metal-molecule-metal junction, Phys. Rev. B **59**(19), 12505–12513 (1999).

[13] R. H. M. Smit, Y. Noat, C. Untiedt, N. D. Lang, M. C. van Hemert, and J. M. van Ruitenbeek, Measurement of the conductance of a hydrogen molecule, Nature **419**, 906–909 (2002).

[14] D. Djukic and J. M. van Ruitenbeek, Shot noise measurements on a single molecule, Nano Letters **6**(4), 789 (2006).

[15] J. Reichert, R. Ochs, D. Beckmann, H. B. Weber, M. Mayor, and H. v. Löhneysen, Driving Current through Single Organic Molecules, Phys. Rev. Lett. **88**(17), 176804 (2002).

[16] B. J. van Wees, H. van Houten, C. W. J. Beenakker, J. G. Williamson, L. P. Kouwenhoven, D. van der Marel, and C. T. Foxon, Quantized conductance of point contacts in a two-dimensional electron gas, Phys. Rev. Lett. **60**(9), 848–850 (1988).

[17] U. Meirav, M. A. Kastner, and S. J. Wind, Single-electron charging and periodic conductance resonances in gaas nanostructures, Phys. Rev. Lett. **65**(6), 771–774 (1990).

[18] J. M. van Ruitenbeek, A. Alvarez, I. P. neyro, C. Grahmann, P. Joyez, M. H. Devoret, D. Esteve, and C. Urbina, Adjustable nanofabricated atomic size contacts, Review of Scientific Instruments **67**(1), 108–111 (1996).

[19] R. Landauer, Spatial Variation of Currents and Fields Due to Localized Scatterers in Metallic Conduction, IBM J. Res. Dev. **1**, 223 (1957).

[20] R. Landauer, Electrical resistance of disordered one-dimensional lattices, Phil. Mag. **57**, 863 (1970).

[21] M. Büttiker, Four-Terminal Phase-Coherent Conductance, Phys. Rev. Lett. **57**(14), 1761–1764 (1986).

[22] O. P. Sushkov, Conductance anomalies in a one-dimensional quantum contact, Phys. Rev. B **64**(15), 155319 (2001).

[23] R. A. Molina, D. Weinmann, R. A. Jalabert, G. L. Ingold, and J. L. Pichard, Conductance through a one-dimensional correlated system: Relation to persistent currents and the role of the contacts, Phys. Rev. B **67**(23), 235306 (2003).

[24] V. Meden and U. Schollwöck, Conductance of interacting nanowires, Phys. Rev. B **67**(19), 193303 (2003).

[25] R. A. Molina, P. Schmitteckert, D. Weinmann, R. A. Jalabert, G. L. Ingold, and J. L. Pichard, Residual conductance of correlated one-dimensional nanosystems: A numerical approach, Eur. Phys. Jour. B **39**, 107 (2004).

[26] A. Freyn, G. Vasseur, P. Schmitteckert, D. Weinmann, G. L. Ingold, R. A. Jalabert, and J. L. Pichard, The embedding method beyond the single-channel case: Two-mode and hubbard chains, Eur. Phys. J. B **75**, 253 (2010), arXiv:0909.5048.

[27] A. Oguri, Y. Nisikawa, and A. C. Hewson, Determination of the Phase Shifts for Interacting Electrons Connected to Reservoirs, J. Phys. Soc. Jpn. **74**, 2554 (2005).

[28] Y. Meir, N. S. Wingreen, and P. A. Lee, Transport through a Strongly Interacting Electron System: Theory of Periodic Conductance Oscillations, Phys. Rev. Lett **66**, 3048 (1991).

[29] K. Louis and C. Gros, Quantum Monte Carlo simulation for the conductance of one-dimensional quantum spin systems, Phys. Rev. B **68**, 184424 (2003).

[30] D. Bohr, P. Schmitteckert, and P. Wölfle, DMRG evaluation of the Kubo formula, Europhys. Lett. **73**, 246 (2006).

[31] D. Bohr and P. Schmitteckert, Strong enhancement of transport by interaction on contact links, Phys. Rev. B **75**(24), 241103(R) (2007).

[32] P. Schmitteckert and F. Evers, Exact Ground State Density-Functional Theory for Impurity Models Coupled to External Reservoirs and Transport Calculations, Phys. Rev. Lett. **100**(8), 086401 (2008).

[33] C. Karrasch, T. Enss, and V. Meden, Functional renormalization group approach to transport through correlated quantum dots, Phys. Rev. B **73**(23), 235337 (2006).

[34] C. A. Büsser, E. V. Anda, A. L. Lima, M. A. Davidovich, and G. Chiappe, Transport in coupled quantum dots: Kondo effect versus antiferromagnetic correlation, Phys. Rev. B **62**(15), 9907–9910 (2000).

[35] Y. Meir and N. S. Wingreen, Landauer Formula for the Current through an Interacting Electron Region, Phys. Rev. Lett **68**, 2512 (1992).

[36] H. Schoeller and J. König, Real-Time Renormalization Group and Charge Fluctuations in Quantum Dots, Phys. Rev. Lett. **84**(16), 3686–3689 (2000).

[37] G. Stefanucci and C. O. Almbladh, Time-dependent partition-free approach in resonant tunneling systems, Phys. Rev. B **69**(19), 195318 (2004).

[38] G. Stefanucci and C. O. Almbladh, Time-dependent quantum transport: An exact formulation based on TDDFT, Europhys. Lett. **67**(1), 14 (2004).

[39] M. Di Ventra and T. N. Todorov, Transport in nanoscale systems: the microcanonical versus grand-canonical picture, J. Phys.: Condens. Matter **16**, 8025 (2004).

[40] N. Bushong, N. Sai, and M. Di Ventra, Approach to Steady-State Transport in Nanoscale Conductors, Nano Letters **5**, 2569 (2005).

[41] S. Weiss, J. Eckel, M. Thorwart, and R. Egger, Iterative real-time path integral approach to nonequilibrium quantum transport, Phys. Rev. B **77**(19), 195316 (2008).

[42] J. E. Han and R. J. Heary, Imaginary-Time Formulation of Steady-State Nonequilibrium: Application to Strongly Correlated Transport, Phys. Rev. Lett. **99**(23), 236808 (2007).

[43] M. A. Cazalilla and J. B. Marston, Time-Dependent Density-Matrix Renormalization Group: A Systematic Method for the Study of Quantum Many-Body Out-of-Equilibrium Systems, Phys. Rev. Lett. **88**(25), 256403 (2002).

[44] H. G. Luo, T. Xiang, and X. Q. Wang, Comment on "Time-Dependent Density-Matrix Renormalization Group: A Systematic Method for the Study of Quantum Many-Body Out-of-Equilibrium Systems", Phys. Rev. Lett. **91**(4), 049701 (2003).

[45] A. J. Daley, C. Kollath, U. Schollwöck, and G. Vidal, Time-dependent density-matrix renormalization-group using adaptive effective Hilbert spaces, Journal of Statistical Mechanics: Theory and Experiment **2004**(04), P04005 (2004).

[46] S. R. White and A. E. Feiguin, Real-Time Evolution using the Density Matrix Renormalization Group, Phys. Rev. Lett. **93**, 076401 (2004).

[47] P. Schmitteckert, Nonequilibrium electron transport using the density matrix renormalization group method, Phys. Rev. B **70**(12), 121302 (2004).

[48] A. E. Feiguin and S. R. White, Time-step targetting methods for real-time dynamics using DMRG, Phys. Rev. B **72**, 020404(R) (2005).

[49] G. Schneider and P. Schmitteckert, Conductance in strongly correlated 1d systems: Real-time dynamics in dmrg (unpublished), cond-mat/0601389.

[50] P. Schmitteckert and G. Schneider, Signal transport and finite bias conductance in and through correlated nanostructures, in: High Performance Computing in Science and Engineering '06, edited by W. E. Nagel, W. Jäger, and M. Resch, (Springer, Berlin, 2006), pp. 113–126.

[51] P. Schmitteckert, Signal transport in and conductance of correlated nanostructures, in: High Performance Computing in Science and Engineering '07, edited by W. E. Nagel, D. B. Kröner, and M. Resch, (Springer, Berlin, 2007), p. 99.

[52] T. Ulbricht and P. Schmitteckert, Signal transport in and conductance of correlated nanostructures, in: High Performance Computing in Science and Engineering '08, edited by W. E. Nagel, D. B. Kröner, and M. Resch, (Springer, Berlin, 2008), pp. 71–82.

[53] A. Branschädel, T. Ulbricht, and P. Schmitteckert, Conductance of Correlated Nanostructures, in: High Performance Computing in Science and Engineering '09, edited by W. E. Nagel, D. Kröner, and M. M. Resch, (Springer, Berlin, 2009), pp. 123–135.

[54] A. Branschädel and P. Schmitteckert, Conductance and Noise Correlations of Correlated Nanostructures, in: High Performance Computing in Science and Engineering '10, edited by W. E. Nagel, D. Kröner, and M. M. Resch, (Springer, Berlin, 2010), pp. 169–179.

[55] K. A. Al-Hassanieh, A. E. Feiguin, J. A. Riera, C. A. Büsser, and E. Dagotto, Adaptive time-dependent density-matrix renormalization-group technique for calculating the conductance of strongly correlated nanostructures, Physical Review B (Condensed Matter and Materials Physics) **73**(19), 195304 (2006).

[56] E. Boulat, H. Saleur, and P. Schmitteckert, Twofold Advance in the Theoretical Understanding of Far-From-Equilibrium Properties of Interacting Nanostructures, Physical Review Letters **101**(14), 140601 (2008).

[57] F. Heidrich-Meisner, A. E. Feiguin, and E. Dagotto, Real-time simulations of nonequilibrium transport in the single-impurity anderson model, Phys. Rev. B **79**(23), 235336 (2009).

[58] F. Heidrich-Meisner, G. B. Martins, C. A. Büsser, K. A. Al-Hassanieh, A. E. Feiguin, G. Chiappe, E. V. Anda, and E. Dagotto, Transport through quantum dots: a combined dmrg and embedded-cluster approximation study, Eur. Phys. J. B **67**(4), 527–542 (2009).

[59] S. Kirino, T. Fujii, J. Zhao, and K. Ueda, Time-Dependent DMRG Study on Quantum Dot under a Finite Bias Voltage, Journal of the Physical Society of Japan **77**(8), 084704 (2008).

[60] L. G. G. V. Dias da Silva, F. Heidrich-Meisner, A. E. Feiguin, C. A. Büsser, G. B. Martins, E. V. Anda, and E. Dagotto, Transport properties and Kondo correlations in nanostructures: Time-dependent DMRG method applied to

quantum dots coupled to Wilson chains, Physical Review B (Condensed Matter and Materials Physics) **78**(19), 195317 (2008).

[61] S. R. White, Density matrix formulation for quantum renormalization groups, Phys. Rev. Lett. **69**(19), 2863–2866 (1992).

[62] S. R. White, Density-matrix algorithms for quantum renormalization groups, Phys. Rev. B **48**(14), 10345–10356 (1993).

[63] S. R. White, Spin Gaps in a Frustrated Heisenberg Model for CaV_4O_9, Phys. Rev. Lett. **77**(17), 3633–3636 (1996).

[64] R. M. Noack and S. R. Manmana, Diagonalization- and numerical renormalization-group-based methods for interacting quantum systems, AIP Conference Proceedings **789**(1), 93–163 (2005).

[65] K. A. Hallberg, New trends in density matrix renormalization, Advances in Physics **55**(5), 477–526 (2006).

[66] U. Schollwöck, The density-matrix renormalization group, Rev. Mod. Phys. **77**(1), 259–315 (2005).

[67] A. Branschädel, G. Schneider, and P. Schmitteckert, Conductance of inhomogenous systems: Real-time dynamics, Ann. Phys. (Berlin) **522**, 657 (2010).

[68] M. Reznikov, M. Heiblum, H. Shtrikman, and D. Mahalu, Temporal Correlation of Electrons: Suppression of Shot Noise in a Ballistic Quantum Point Contact, Phys. Rev. Lett. **75**(18), 3340–3343 (1995).

[69] A. Kumar, L. Saminadayar, D. C. Glattli, Y. Jin, and B. Etienne, Experimental Test of the Quantum Shot Noise Reduction Theory, Phys. Rev. Lett. **76**(15), 2778–2781 (1996).

[70] R. de Picciotto, M. Reznikov, M. Heiblum, V. Umansky, G. Bunin, and D. Mahalu, Direct observation of a fractional charge, Nature **389**, 162–164 (1997).

[71] M. Reznikov, R. de Picciotto, T. G. Griffiths, M. Heiblum, and V. Umansky, Observation of quasiparticles with one-fifth of an electron's charge, Nature **399**, 238–241 (1999).

[72] M. Esposito, U. Harbola, and S. Mukamel, Nonequilibrium fluctuations, fluctuation theorems, and counting statistics in quantum systems, Rev. Mod. Phys. **81**(4), 1665–1702 (2009).

[73] I. Klich and L. Levitov, Quantum Noise as an Entanglement Meter, Phys. Rev. Lett. **102**(10), 100502 (2009).

[74] I. Klich and L. Levitov, Many-Body Entanglement: a New Application of the Full Counting Statistics, AIP CONFERENCE PROCEEDINGS **1134**, 36 (2009).

[75] B. Reulet, J. Senzier, and D. E. Prober, Environmental Effects in the Third Moment of Voltage Fluctuations in a Tunnel Junction, Phys. Rev. Lett. **91**(19), 196601 (2003).

[76] Y. Bomze, G. Gershon, D. Shovkun, L. S. Levitov, and M. Reznikov, Measurement of Counting Statistics of Electron Transport in a Tunnel Junction, Phys. Rev. Lett. **95**(17), 176601 (2005).

[77] L. Levitov and G. Lesovik, Charge distribution in quantum shot noise, JETP Lett **58**, 230 (1993).

[78] L. Levitov, H. Lee, and G. B. Lesovik, Electron counting statistics and coherent states of electrical current, J. Math. Phys. **37**, 4845 (1996).

[79] A. Gogolin, R. Konik, A. W. W. Ludwig, and H. Saleur, Counting statistics for the Anderson impurity model: Bethe ansatz and Fermi liquid study, Ann. der Physik **16**, 678 (2007).

[80] P. Fendley and H. Saleur, Nonequilibrium dc noise in a luttinger liquid with an impurity, Phys. Rev. B **54**(15), 10845–10854 (1996).

[81] R. M. Konik, H. Saleur, and A. W. W. Ludwig, Transport through Quantum Dots: Analytic Results from Integrability, Phys. Rev. Lett. **87**(23), 236801 (2001).

[82] P. Mehta and N. Andrei, Nonequilibrium quantum impurities: From entropy production to information theory, Phys. Rev. Lett. **100**(8), 086804 (2008).

[83] S. P. Chao and G. Palacios, Non-equilibrium Transport in the Anderson model of a biased Quantum Dot: Scattering Bethe Ansatz Phenomenology.

[84] A. Branschädel, E. Boulat, H. Saleur, and P. Schmitteckert, Numerical evaluation of shot noise using real-time simulations, Phys. Rev. B **82**(20), 205414 (2010).

[85] A. Branschädel, E. Boulat, H. Saleur, and P. Schmitteckert, Shot Noise in the Self-Dual Interacting Resonant Level Model, Phys. Rev. Lett. **105**(14), 146805 (2010).

[86] P. W. Anderson, Localized Magnetic States in Metals, Phys. Rev. **124**(1), 41–53 (1961).

[87] P. Schmitteckert, Calculating green functions from finite systems, J. Phys.: Conf. Ser. **220**, 012022 (2010).

[88] M. Vekić and S. R. White, Smooth boundary conditions for quantum lattice systems, Phys. Rev. Lett. **71**(26), 4283–4286 (1993).

[89] M. Abramowitz and I. Stegun, Handbook of Mathematical Functions with Formulas, Graphs and Mathematical Tables (Dover Publications, 1964).

[90] W. H. Press, S. A. Teukolsky, W. T. Vetterling, and B. P. Flannery, Numerical Recipes 3rd Edition: The Art of Scientific Computing, 3 edition (Cambridge University Press, September 2007).

[91] G. H. Golub and C. F. van Loan, Matrix Computations (Johns Hopkins Studies in Mathematical Sciences), 3rd edition (The Johns Hopkins University Press, October 1996).

[92] Y. Saad, Analysis of some krylov subspace approximations to the matrix exponential operator, SIAM Journal on Numerical Analysis **29**(1), pp. 209–228 (1992).

[93] R. B. Sidje, Expokit: a software package for computing matrix exponentials, ACM Trans. Math. Softw. **24**(1), 130–156 (1998).

[94] C. Moler and C. F. van Loan, Nineteen dubious ways to compute the exponential of a matrix, twenty-five years later, SIAM Review **45**(1), 3–49 (2003).

[95] N. J. Higham, The scaling and squaring method for the matrix exponential revisited, SIAM J. Matrix Anal. Appl. **26**(4), 1179–1193 (2005).

[96] A. Weiße, G. Wellein, A. Alvermann, and H. Fehske, The Kernel Polynomial Method, Rev. Mod. Phys. **78**(1), 275–306 (2006).

[97] K. G. Wilson, The renormalization group: Critical phenomena and the Kondo problem, Rev. Mod. Phys. **47**(4), 773–840 (1975).

[98] A. C. Hewson, The Kondo Problem to Heavy Fermions (Cambridge University Press, 1993).

[99] A. Krylov, On the numerical solution of the equation by which in technical questions frequencies of small oscillations of material systems are determined, Izvestija AN SSSR (News of Academy of Sciences of the USSR) **VII**(4), 491 (1931).

[100] K. Schönhammer, Full counting statistics for noninteracting fermions: Exact results and the Levitov-Lesovik formula, Phys. Rev. B **75**(20), 205329 (2007).

[101] S. R. White and R. M. Noack, Real-space quantum renormalization groups, Phys. Rev. Lett. **68**(24), 3487–3490 (1992).

[102] F. Verstraete, J. J. García-Ripoll, and J. I. Cirac, Matrix Product Density Operators: Simulation of Finite-Temperature and Dissipative Systems, Phys. Rev. Lett. **93**(20), 207204 (2004).

[103] T. Barthel, U. Schollwöck, and S. R. White, Spectral functions in one-dimensional quantum systems at finite temperature using the density matrix renormalization group, Phys. Rev. B **79**(24), 245101 (2009).

[104] S. Liang and H. Pang, Approximate diagonalization using the density matrix renormalization-group method: A two-dimensional-systems perspective, Phys. Rev. B **49**(13), 9214–9217 (1994).

[105] P. Calabrese and J. Cardy, Entanglement entropy and quantum field theory, Journal of Statistical Mechanics: Theory and Experiment **2004**(06), P06002 (2004).

[106] C. Beenakker, Electron-hole entanglement in the Fermi sea, Proc. Int. School Phys. E. Fermi, Vol. 162, (IOS Press, Amsterdam, 2006), cond-mat/0508488.

[107] E. Schrödinger, Quantisierung als Eigenwertproblem, Annalen der Physik **386**(18), 109–139 (1926).

[108] A. Alvermann and H. Fehske, Chebyshev approach to quantum systems coupled to a bath, Phys. Rev. B **77**(4), 045125 (2008).

[109] P. Mehta and N. Andrei, Nonequilibrium Transport in Quantum Impurity Models: The Bethe Ansatz for Open Systems, Phys. Rev. Lett. **96**(21), 216802 (2006).

[110] G. D. Mahan, Many-Particle Physics, 3rd edition (Kluwer Academics / Plenum Publishers, New York, N.Y., 2000).

[111] S. Ramasesha, A new algorithm for solving large inhomogeneous linear system of algebraic equations, Journal of Computational Chemistry **11**(5), 545–547 (1990).

[112] L. D. Landau and E. M. Lifshitz, Statistical Physics (Pergamon, Oxford, 1959).

[113] Y. Imry, Introduction to Mesoscopic Physics (Oxford University Press, 1997).

[114] N. S. Wingreen, A. P. Jauho, and Y. Meir, Time-dependent transport through a mesoscopic structure, Phys. Rev. B **48**(11), 8487–8490 (1993).

[115] M. Cini, Time-dependent approach to electron transport through junctions: General theory and simple applications, Phys. Rev. B **22**(12), 5887–5899 (1980).

Bibliography

[116] I. Bâldea and H. Köppel, Sources of negative differential resistance in electric nanotransport, Phys. Rev. B **81**(19), 193401 (2010).

[117] H. Saleur and U. Weiss, Point-contact tunneling in the fractional quantum Hall effect: An exact determination of the statistical fluctuations, Phys. Rev. B **63**(20), 201302 (2001).

[118] P. Longo, P. Schmitteckert, and K. Busch, Few-photon transport in low-dimensional systems: Interaction-induced radiation trapping, Phys. Rev. Lett. **104**(Jan), 023602 (2010).

[119] Y. M. Blanter and M. Büttiker, Shot noise in mesoscopic conductors, Physics Reports **336**, 1 (2000).

[120] F. Lesage and H. Saleur, Correlations in one-dimensional quantum impurity problems with an external field, Nuclear Physics B **490**(3), 543 – 575 (1997).

[121] C. d. C. Chamon, D. E. Freed, and X. G. Wen, Tunneling and quantum noise in one-dimensional Luttinger liquids, Phys. Rev. B **51**(4), 2363–2379 (1995).

Index

Index

noise power spectrum, 52
    numerical evaluation of, 82

Poisson statistics, 90
polynomial
    expansion, 27
        applications of, 32
        Green's function, 36
        resolvent expressions, 36
        time evolution, 32
    expansion coefficient, 28
    moment, 28
polynomials
    Chebyshev, 29, 30
    Laguerre, 29, 31
    orthogonal, 27

quasi-stationary state, 56

resolvent, 28
resolvent expressions, 36
resonant tunneling, 8

scattering state, 101
self-energy, 39
settling time, 54
short time behaviour, 56
shot noise, 50, 52
    IRLM, 86
    resonant level model, 79
single particle decomposition, 15
spectral function
    IRLM, 39
    noninteracting RLM, 103
    single-particle, 42
spinless fermions, 7
sweep, 24

temperature evolution, 34
    Chebyshev expansion, 35
    Laguerre expansion, 35
tight-binding chain, 7
time evolution, 25, 32
    Chebyshev expansion, 32
        truncation of, 33

imaginary, 34
    Chebyshev expansion, 35
    Laguerre expansion, 35
    Krylov subspace method, 25
transit time, 54
    damped boundary conditions, 73
truncation error, 20, 22
truncation scheme, 18

wave function
    truncated, 18
weight function, 28

Acknowledgements